DESIGN AND DEVELOPMENT OF NOVEL RADIO FREQUENCY IDENTIFICATION (RFID) TAG STRUCTURES

A Dissertation
Presented to
The Academic Faculty

by

Li Yang

In Partial Fulfillment
of the Requirements for the Degree
Doctor of Philosophy in the
School of Electrical and Computer Engineering

Georgia Institute of Technology
December 2009

DESIGN AND DEVELOPMENT OF NOVEL RADIO FREQUENCY IDENTIFICATION (RFID) TAG STRUCTURES

Approved by:

Dr. Manos Tentzeris, Advisor
School of Electrical and Computer Engineering
Georgia Institute of Technology

Dr. Mary Ann Ingram
School of Electrical and Computer Engineering
Georgia Institute of Technology

Dr. Joy Laskar
School of Electrical and Computer Engineering
Georgia Institute of Technology

Dr. Stylianos Kavadias
College of Management
Georgia Institute of Technology

Dr. Gerald DeJean
School of Electrical and Computer Engineering
Georgia Institute of Technology

Date Approved: November 2, 2009

To my beloved family

ACKNOWLEDGEMENTS

It has been a long journey of education and discovery toward the PhD in Georgia Tech. However, it becomes worthy when I have received a lot of help, encouragement, and love from people listed below.

First, I would like to acknowledge the enthusiastic supervision from my research advisor, Professor Manos M. Tentzeris. He has motivated me to provide the excellence and the novelty in the research and guided me to reach the outstanding outcomes in the most right way. For that, I am eternally grateful to him.

I want to thank my proposal and defense committee members for their time and suggestions. I would like to thank all my colleagues from the ATHENA research group, as well as all of my friends. Giulia, my dissertation would not have been completed without her help and passion. I have leant a lot from her in research and personality. Bo, Amin, Terence, Jong-Hoon, Trang, Rushi, Jonathan, Napol, Toni, Serkan, Rongwei, Yuan, and Xin, thank all of them for their generous help in research and companionship in these years. I would like to thank Dr. Ronglin Li and Dr. Daniela Staiculescu for their help in my research. I also want to thank GEDC crews including Ms. Joi Adams, Ms. Angelika Braig, Ms. DeeDee Bennett, and Mr. Christopher Evans.

I owe too much to my parents, Guofeng Yang and Shuhua Ni, for their endless love and unlimited support to help me walk out of a small town to see the outer world.

I reserve this final paragraph for my great and beloved wife Jiexin Li. I can not find any single word to express my deepest gratitude for your love, faith, patience and support.

TABLE OF CONTENTS

LIST OF TABLES

LIST OF FIGURES

LIST OF SYMBOLS AND ABBREVIATIONS

ASK	Amplitude Shift Keying
BCB	Benzocyclobutene
BW	Bandwidth
CI	Confidence Intervals
CNT	Carbon Nanotube
dB	Decibel
DMF	Dimethylformamide
DOE	Design of Experiments
EAS	Electronic Article Surveillance
EIRP	Effective Isotropic Radiated Power
EM	Electromagnetic
EPC	Electronic Product Code
ε_r	Relative Permittivity
GHz	Gigahertz
IFF	Identify-friend-or-foe
LCP	Liquid Crystal Polymer
MEMS	Micro Electromechanical Systems
mm	Millimeter
MWNT	Multi-Walled Carbon Nanotube
PET	Polyethylene Terephthalate
RF	Radio Frequency
RFID	Radio Frequency Identification
RSM	Response Surface Methodology

RTSA	Real-time Spectrum Analyzer
SWNT	Single-Walled Carbon Nanotube
tanδ	Loss Tangent
TL	Transmission Line
μm	Micron
VNA	Vector Network Analyzer
WBAN	Wireless Body-area Network

SUMMARY

The objective of the proposed research is to design and develop a series of radio frequency identification (RFID) tag structures that exhibit good performance characteristics with cost optimization and can be realized on flexible substrates such as liquid crystal polymer (LCP), paper-based substrate and magnetic composite material for conformal applications.

The demand for flexible RFID tags has recently increased tremendously due to the requirements of automatic identification in various areas. Several major challenges existing in today's RFID technologies need to be addressed before RFID can eventually march into everyone's daily life, such as how to design high performance tag antennas with effective impedance matching for passive RFID IC chips to optimize the power performance, how to fabricate ultra-low-cost RFID tags in order to facilitate mass production, how to integrate sensors with passive RFID tags for pervasive sensing applications, and how to realize battery-free active RFID tags in which changing battery is not longer needed. In this research, different RFID tag designs are realized on flexible substrates. The design techniques presented set the framework for answering these technical challenges for which, the focus will be on RFID tag structure design, characterization and optimization from the perspectives of both costs involved and technical constraints.

CHAPTER 1

INTRODUCTION

Radio frequency identification (RFID) tags have become quite widespread in many services in the industry such as access control, parcel and document tracking, distribution logistics and automotive systems. In these applications, a wireless communication link is provided between a remote transponder and an interrogator. A suitable tag must have low cost, low profile, and good performance in the targeting application environment. In this chapter, the history and issues in RFID tag design are presented, along with a critical discussion of emerging trends.

RFID is a rapidly developing automatic wireless data-collection technology with a long history [1]. The first multi-bit functional passive RFID systems, with a range of several meters, appeared in the early 1970s [2] and continued to evolve through the 1980s [3]. Recently, RFID has experienced a tremendous growth, due to developments in integrated circuits, radios and increased interest from the retail industry and government [4]. Thus, the first decade of the 21st century sees the world moving toward the technology's widespread and large-scale adoption. A major landmark was the announcement by Wal-Mart Inc. to mandate RFID for its suppliers in "the near future," at the Retail Systems Conference in June 2003 in Chicago. This was followed by the release of the first electronic product code (EPC) global standard in January 2005. It has been predicted that worldwide revenue for RFID will eclipse $1.2 billion in 2008, an almost 31% increase over the previous year [5]. Key volume applications for RFID technology have been in markets such as access control, sensors and metering applications, payment systems, communication and transportation, parcel and document tracking, distribution logistics, automotive systems, livestock/pet tracking, and hospitals/pharmaceutical applications [6].

An RFID system consists of readers and tags. A typical system has a few readers, either stationary or mobile, and many tags that are attached to objects, as illustrated in Figure 1.1. A reader communicates with the tags in its wireless range and collects information about the objects to which tags are attached. RFID technology has many advantages over the existing barcode technology. RFID tags can be embedded in an item rather than the physical exposure requirement of barcodes and can be detected using a radio frequency (RF) signal. Communication based on RF signals also enhances the read range for RFID tags. In addition, barcodes only contain information about the manufacturer of an item and basic information about the object itself; however, RFID is particularly useful for applications in which the item must be identified uniquely. RFID also can hold additional functionality, which means more bits of information.

Figure 1.1: Conceptual diagram of an RFID system.

The roots of RFID technology can be traced back to World War II. Both sides in the war were using radar to warn of approaching planes while they were still miles away; however, it was impossible to distinguish enemy planes from Allied ones. The Germans

discovered that by just rolling planes when returning to base changes the radio signal reflected back, which would alert the radar crew on the ground. This crude method made it possible for the Germans to identify their planes. The British developed the first active identify-friend-or-foe (IFF) system. By just putting a transmitter on each British plane, it received signals from the aircraft and identified it as a friend [7].

An early exploration of the RFID technology came in October 1948 by Harry Stockman [8]. He stated back then that "considerable research and development work has to be done before the remaining basic problems in reflected-power communication are solved, and before the field of useful applications is explored." His vision flourished until other developments in the transistor, the integrated circuit, the microprocessor, and the communication networks took place. RFID had to wait for a while to be realized [9].

The advances in radar and RF communications systems continued after World War II through the 1950s and 1960s, as described in Table 1.1. In the 1960s, application field trials were initiated, followed by first commercial product. Companies were investigating solutions for anti-theft, which revolutionized the whole RFID industry. They investigated anti-theft systems that utilized RF waves to monitor if an item was paid or not. This was the start of the 1-bit electronic article surveillance (EAS) tags by Sensormatic, Checkpoint, and Knogo. This is by far the most commonly used RFID application.

The electronic identification of items caught the interest of large companies as well. In 1970s large corporations like Raytheon (RayTag 1973), RCA, and Fairchild (Electronic Identification system 1975, electronic license plate for motor vehicles 1977) built their own RFID modules. Thomas Meyers and Ashley Leigh of Fairchild also developed a passive encoding microwave transponder in 1978 [9].

By the 1980s there were mainstream applications all around the world. The RFID was like a wildfire spreading without any boundaries. In the United States, RFID technology found its place in transportation (highway tolls) and personnel access (smart

ID cards). In Europe, industrial and business systems RFID applications, such as short-range animal tracking, attracted industry. Using RFID technology, the world's first commercial application for collecting tolls in Norway (1987) and after in the United States by the Dallas North Turnpike (1989) was established.

Table 1.1: The decades of RFID

Decade	Event
1940-1950	Radar refined and used, major World War II development effort. RFID invented in 1948.
1950-1960	Early explorations of RFID technology, laboratory experiments.
1960-1970	Development of the theory of RFID. Start of applications field trials.
1970-1980	Explosion of RFID development. Tests of RFID accelerate. Very early adopter implementations of RFID.
1980-1990	Commercial applications of RFID enter mainstream.
1990-2000	Emergence of standards. RFID widely deployed. RFID becomes a part of everyday life.

In the 1990s, IBM engineers developed and patented a UHF RFID system. IBM conducted early research with Wal-Mart, but this technology was never commercialized. UHF offered a longer read range and faster data transfer compared to the 125 kHz and 13.56 MHz applications. These accomplishments led the way to the world's first open highway electronic tolling system in Oklahoma in 1991. This was followed by the world's first combined toll collection and traffic management system in Houston by the Harris County Toll Road Authority (1992). In addition to this, GA 400 and Kansas

Turnpike Highways were the first to implement multi-protocol tags, which allowed two different standards to be read [7][9].

After IBM's early pilot studies in the 1990s with Wal-Mart, UHF RFID got a boost in 1999 when the Uniform Code Council, European Article Number International, Procter & Gamble, and Gillette teamed up to establish the Auto-ID Center at the Massachusetts Institute of Technology. This research focused on putting a serial number on the tag to keep the price down using a microchip and an antenna. By storing this information in a database, tag tracking was finally realized in this grand networking technology. This was a crucial point in terms of business because now a stronger communication link between the manufacturers and the business partners was established. A business partner would now know when a shipment was leaving the dock at a manufacturing facility or warehouse, and a retailer could automatically let the manufacturer know when the goods arrived [7].

The Auto-ID Center also initiated the two air interface protocols (Class 1 and Class 0), the EPC numbering scheme, and the network architecture used to seek for the RFID tag data between 1999 and 2003. The Uniform Code Council licensed this technology in 2003 and EPCglobal was born as a joint venture with European Article Number International to commercialize EPC technology.

Today some of the biggest retailers in the world such as Albertsons, Metro, Target, Tesco, Wal-Mart, and the U.S. Department of Defense stated that they plan to use EPC technology to track their goods. The healthcare/pharmaceutical, automotive, and other industries are also pushing toward adaptation of this new technology. EPCglobal adopted a second-generation (Gen-2 ISO18000-6-C) standard in January 2005. This standard is widely used in the RFID world today [7].

For a successful RFID implementation one has to possess a keen knowledge of its standards, its technology, and how it meets the different needs for various applications. FedEx CIO Rob Carter quoted Bill Gates' definition of a "2-10 technology" in an

interview when he was asked about RFID. “2-10 technology” means that for the first two years, hype reigns, followed by disappointment, until the day 10 years later when people realize the technology has flourished and become part of daily life. Carter accepts after noticing some challenges and problems FedEx is experiencing with tags, that “RFID might be a 3-15 technology.” [10] This citing comes from a man who is in charge of the whole activity of tracking parcels it does not even own for up to 48 hours anywhere in the world – an activity that cries out for RFID.

Apart from higher-level problems in RFID applications, tag design imposes different lower level challenges. These challenges include current high cost of tags, impedance matching, and tag performance issues. From a system point of view problems at the lower level must be resolved before moving up on the RFID system hierarchy for an optimized overall performance.

To sell RFID tags just like any other product, the tags have to be cheap. RFID is intended to produce an electronic replacement for the ubiquitous UPC barcode. By implementing the barcode in electronic form, it is expected that item-level RFID will enable automated inventory control in supermarkets and department stores, will facilitate rapid checkout, and will also allow more efficient product flow from the manufacturer to the consumer with reduced overall wastage and idle inventory. Individually tagged items typically have a price floor in the range of a few cents to a few tens of cents. Given typical price margins, it will therefore be necessary to deliver a tag with a total price perturbation of perhaps less than 1 cent to allow widespread deployment [11]. In contrast, pallet-level tracking solutions that are currently being deployed have price-points larger than 10 cents. Mark Roberti’s report [12] based on Auto-ID Center’s predictions on IC manufacturing cost reduction [13] indicates that in the near future the cost of a passive tag can reach as low as 5 cents from 30-35 cents [14] as it is now. The prediction relies on the fact that these tags will be sold in high volume, about 30 billion a year, which would in turn reduce the cost of ICs to almost 1 cent. The rest of the cost will be

distributed in the cost of the substrate and the assembly process. Paper-based substrates are a promising candidate for the low-cost substrate material. The high demand and the mass production of paper make it widely available and the lowest cost material ever made [15]. Using paper as the substrate for RFID tags can dramatically reduce the material cost. However, there are hundreds of different paper materials available in the commercial market, varying in density, coating, thickness, texture, etc. Each has its own RF characteristics. Therefore, the RF characterization of paper substrates becomes a must for optimal designs utilizing this low-cost substrate. Some characterization work has been done in frequencies beneath UHF band [16][17][18], but none – to the author's knowledge – in or above UHF band.

Tag performance in an RFID system is mostly evaluated by how the tag read range is in different environments. This depends mainly on the tag IC and antenna properties as well as the propagation environment. The tag characteristics can be summed up in IC sensitivity, antenna gain, antenna polarization, and impedance match. The propagation environment limitations are the path loss and tag detuning [19].

Unlike most of the other RF front ends in which antennas have been designed primarily to match either 50Ω or 75Ω loads for years, an RFID tag antenna has to be directly matched to the IC chip, which primarily exhibits complex input impedance. This is because to maximize the performance of the transponder, maximum power must be delivered from the antenna to the IC. Therefore, the impedance-matching technique plays an important role in a successful RFID tag design.

The equivalent circuit of the antenna load is shown in Figure 1.2. *Vs* is the voltage across the antenna, which is induced from the receiving signal. The antenna displays complex input impedance Z_{ANT} at its terminals. The chip also displays complex impedance Z_{LOAD}, when looking into the opposite direction of the antenna. The load's impedance is dependent on the IC and can be measured. To ensure maximum power transfer from the antenna to the load, the input impedance of the antenna must be

conjugately matched to the IC's impedance in the operating frequency of the tag [20], as depicted in Equation 1.1. In other words, the real part of the antenna input impedance must be equal to the real part of the load's impedance and the imaginary part of the antenna input impedance must be equal to the opposite of the imaginary part of the load's impedance [21].

$$Z_{ANT} = Z_{LOAD}^{*} \tag{1.1}$$

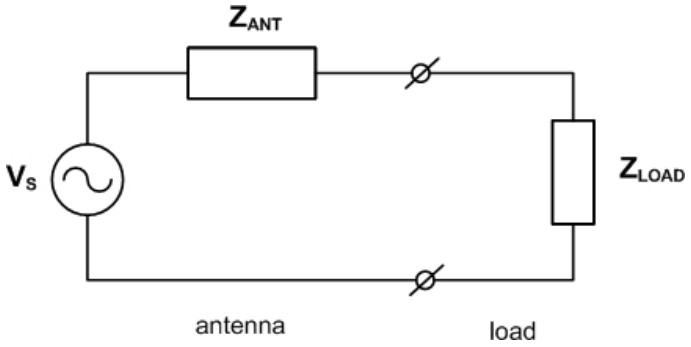

Figure 1.2: The equivalent circuit of an RFID tag.

Kurokawa [22] described a concept of power waves traveling between the generator and load, and introduced the following definitions for the power reflection coefficient $|s|^2$, as shown in Equation 1.2.

$$|s|^2 = \left| \frac{Z_{LOAD} - Z_{ANT}^{*}}{Z_{LOAD} + Z_{ANT}} \right|^2, \quad 0 \le |s|^2 \le 1 \tag{1.2}$$

The power reflection coefficient $|s|^2$ shows what fraction of the maximum power available from the antenna is not delivered to the load [23].

In free-space propagation environment, the power arrived at an RFID antenna can be calculated using Friss free-space equation as:

$$P_a = P_t G_t G_r (\frac{\lambda}{4\pi d})^2 \tag{1.3}$$

where P_t is the power transmitted by the reader, G_t is the gain of the reader antenna, G_r is the gain of the receiving tag antenna, λ is the wavelength, and d is the distance between the reader and the tag. $P_t G_t$ is the equivalent isotropic radiated power, denoted as EIRP.

If the minimum threshold power necessary to power up the chip is P_{th}, then read range r can be calculated as

$$r = \frac{\lambda}{4\pi}\sqrt{\frac{EIRP \cdot G_r \cdot \tau}{P_{th}}} \tag{1.4}$$

where $\tau = 1-|s|^2$, named power transmission coefficient. As a result, achieving maximum power transfer from the antenna to the load is translated into minimizing the power reflection coefficient $|s|^2$. It has to be noted that both the impedance of the antenna and the load vary with frequency. For this reason $|s|^2$ can be minimized in a single frequency. Consequently this is chosen to be the operation frequency of the RFID tag. To be noticed, in Equation 1.4, polarization match between the reader and tag antennas is assumed. In the majority of applications the tag antenna polarization is usually linear because of pre-required small size of the tag, and the reader antenna polarization is circular to allow the tag to appear in almost arbitrary position in the field of the reader antenna. Thus a sacrifice of -3 dB power loss due to polarization mismatch between circularly polarized reader antenna and linearly polarized tag antenna overcomes the problem of tag orientation. The read range r would be $1/\sqrt{2}$ times shorter due to the polarization mismatch.

Adding an external matching network with lumped elements is usually prohibited due to cost, fabrication, and size issues. Instead, a serial stub feed structure has been

proved an effective method for the impedance match [24]. The resistive shorting stub and the double inductive stub make up the overall matching network to match to the chip input impedance. However, in the serial stub feed structure, the dimensions of the resistive shorting stub and the double inductive stub are comparable with the antenna main radiating body. These stubs limit the miniaturization of the antenna size. Good impedance matching antennas with small form factor are highly desired in practical usage. Therefore, for a compact RFID antenna design, other matching techniques without any stubs need to be explored.

Active tags, which are a subclass of RFID tag, use batteries to power their communication circuitry and benefit from relatively long wireless range. Unlike the passive ones, active RFID systems can be used as sensor nodes and they can monitor and store environment data, such as acceleration or temperature. However, the need for an external battery limits their applications to where battery replacements are possible and affordable. Battery technology is mature, extensively commercialized, and completely self-contained. However, given current energy density and shelf-life trends, even for relatively large batteries and conservative communication schedules, the mean time to replacement is only a year or two [25]. For some applications, such as harsh environment monitoring, in which battery changing is not easy, the problem is aggravated significantly. Concerns over relatively short battery life have restricted wireless device applications. Therefore, researchers have been looking for alternative power sources. A possible and promising solution is based on the idea of harvesting or scavenging ambient energy from the environment and converting it to electricity, thus eliminating the need for batteries and extending the device lifetime deployment duration dramatically or even indefinitely.

Over the past few years there has been an increasing focus on developing power scavenging techniques for wearable electronics, since the human body is an under-estimated energy source that is continuously generating steady thermoelectric, blood pressure and motion energy outputs. For example, it has been shown that the heat flow

generated by the human body creates a power density of about 20mW/cm^2 on average. Ramsay and Clark [26] found that output power generated from an average person's blood pressure at 100 mmHg is about 0.93W. Thad Starner's investigation [27] analyzed various human activities and found that the heel strike during walking is a plentiful and readily tapped source of wasted energy. Starner estimated that an average 67 watts of power are available in the heel movement of a 68 kg person walking at a brisk pace. Admittedly, scavenging most of that energy unobtrusively would be impossible. But even a small percentage of it would provide enough power to operate many of the body-worn systems on the market today. Vladimir Leonov [28] demonstrated a wrist-watch type of thermoelectric generator providing a useful power of 0.2-0.3mW for usual daily-life activity, and 0.1mW on immobilized subjects with low metabolic rate to power a wireless sensor node. Paul Mitcheson [29] has proposed several forms of vibration-driven MEMS microgenerator using the motion of the human body to produce power at the scale of tens of microwatts. In the ETA Autoquartz, a proof mass winds a spring that pulses a microgenerator at its optimal rate of 15,000 rotations per minute for 50 ms, yielding 6 mA bursts at greater than 16 V that are integrated on a storage capacitor [30]. However, until today few reports have been seen in the RFID area about the development of battery-free active tags using the human body as a renewal energy source for wearable electronics applications.

In this dissertation, different RFID tag structures have been designed on flexible substrates. In Chapter 2, RFID tag antenna impedance matching techniques are investigated. In Chapter 3, the characterization of paper-based material has revealed that paper substrate is one of the best organic-substrate candidates for low-cost RFID tag applications. The high demand and the mass production of paper make it widely available and at the same time the lowest cost material ever made. From a manufacturing point of view paper can undergo large reel-to-reel processing, thus mass fabricating RFID inlays on paper becomes more feasible. Paper also has low surface profile and is suitable for

direct write methodologies, such as conductive inkjet printing instead of the traditional metal etching techniques. Such a fast process can be used efficiently to print electronics on the surface of paper substrate or even embedded in a multilayer fashion. Inkjet-printed paper-based RFID tags have been researched as a solution for ultra-low-cost RFID tag design. In Chapter 4, in addition to the paper-based substrate, magnetic composite material will be examined as an alternative solution for flexible RFID tags. Substrate impacts on RFID tag antenna performance have been studied. Chapter 5 focuses on the realization of RFID-enabled sensor module. A prototype of chipless passive RFID integrated with inkjet-printed carbon nanotubes is demonstrated for low-cost sensing applications. In Chapter 6, battery-free active RFID tag has also been researched which will serve as a promising solution for wearable identification/tracking system. Energy scavenging technique has been applied to extract the electrical energy from renewal energy resources such as human body movement to power up the active RFID tag. The costly replacing of batteries can therefore be avoided. Chapter 7 concludes this dissertation, summarizing its contributions.

CHAPTER 2

ANTENNA ARCHITECTURES FOR PASSIVE RFID TAGS

RFID has become a pervasive technology [31] in everyday life. The electromagnetic research mainly concerns the design of tag antennas having high efficiency and small size, and suited to complex impedance matching to the embedded electronics [32]. In this chapter, the RFID antenna impedance-matching techniques will be investigated. For each design solution, the role of the main geometrical parameters over the complex impedance tuning is examined. Three passive UHF RFID tag modules, targeting at meeting three different application requirements – size reduction, high directivity, and tagging metallic objects – are then developed with satisfied performance.

2.1 RFID Antenna Impedance-matching Techniques

Because of the integrated on-chip energy-storage device, most of the available passive RFID IC chips exhibit an input reactance roughly ranging from -100 Ω to -400 Ω [32], while the real part is about an order-of-magnitude smaller. The tag antenna impedance should be inductive in order to achieve conjugate matching. To obtain low-cost devices, it is not feasible to use external matching networks involving lumped components. Therefore, the matching mechanisms have to be embedded within the tag's antenna layout.

2.1.1 T-match Structure

To introduce tunable parameters to a dipole of length *l*, a centered short-circuit stub and a second dipole of length *a* are added, forming the T-match structure. The IC chip is connected to the second dipole with a distance *b* from the larger dipole. T match acts as an impedance transformer, as shown in Figure 2.1.

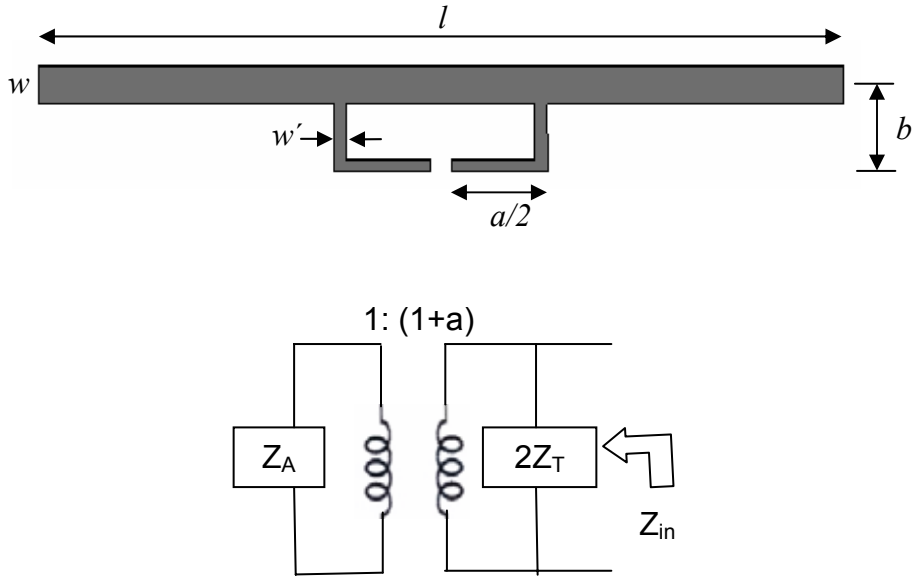

Figure 2.1: The T-match structure and the equivalent circuit.

The impedance at the source point is given by [33]

$$Z_{in} = \frac{2Z_t(1+a)^2 Z_A}{2Z_t + (1+a)^2 Z_A} \tag{2.1}$$

where $Z_t = jZ_0 \tan ka/2$ is the input impedance of the short-circuit stub formed by the T-match conductors and part of the dipole; $Z_0 = 276\log(b/\sqrt{r_e r_e'})$ is the characteristic impedance of the two-conductor transmission line with spacing b; Z_A is the dipole impedance taken at its center in the absence of the T-match connection; r_e=0.25w and r_e'=8.25w' are the equivalent radii of the dipole and of the matching stub; and $\alpha=\ln(b/r_e')/\ln(b/r_e)$ is the current division factor between the two conductors. The geometrical parameters, a, b and w' can be adjusted to match the antenna impedance to the complex chip impedance Z_{chip}.

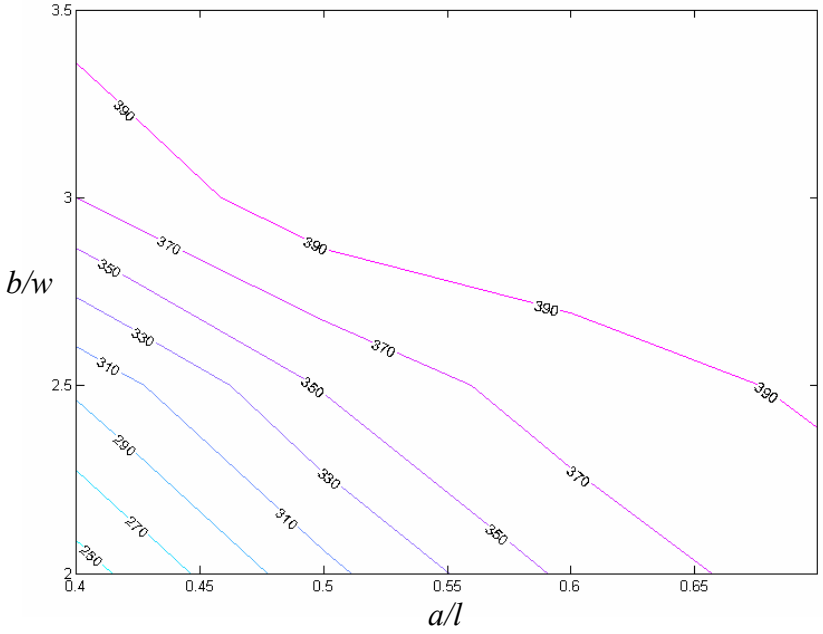

(a)

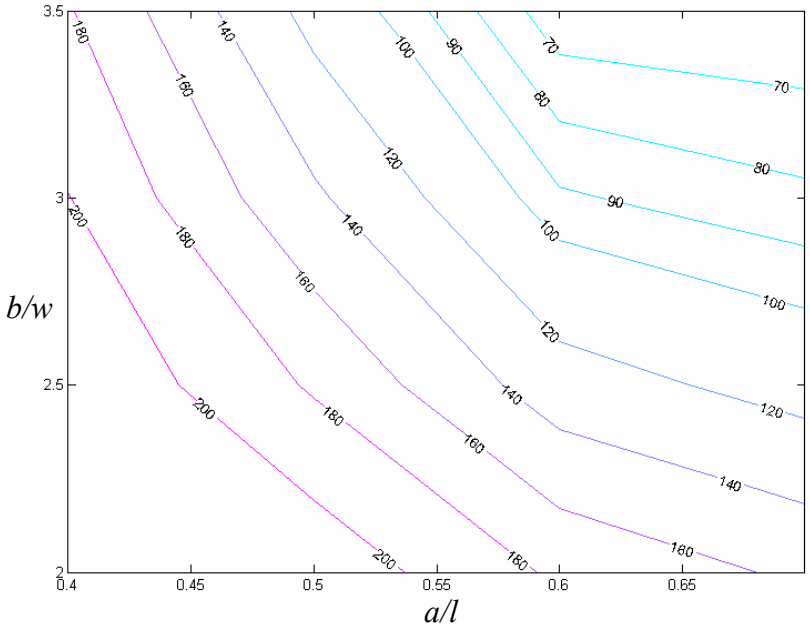

(b)

Figure 2.2: The T-match structure matching chart for the case of l=λ/2, w=λ/100, w'=w/2: (a) resistance (b) reactance.

Figure 2.2 shows the matching chart for the T-match structure. The ratio between the dipoles' cross sections have been fixed to $w/w'=2$. In particular, it can be easily verified from Equation 2.1 that the increase of the w/w' ratio will raise the impedance values. To be noticed the contour lines in the resistance and reactance plots become mutually parallel, resulting in a reduced matching agility. Further more, even with small values of *a* and *b*, high values of input resistance are observed. This makes it difficult to match the impedance to IC chips. Therefore, a single T-match structure could not be completely adequately for matching, unless some shape modification of the main radiator is considered.

2.1.2 Inductively-coupled Structure

The inductively-coupled structure consists of a feed loop with two terminals and a radiating body. The two terminals of the loop are connected to the IC, and the feed "communicates" with the antenna body through mutual coupling.

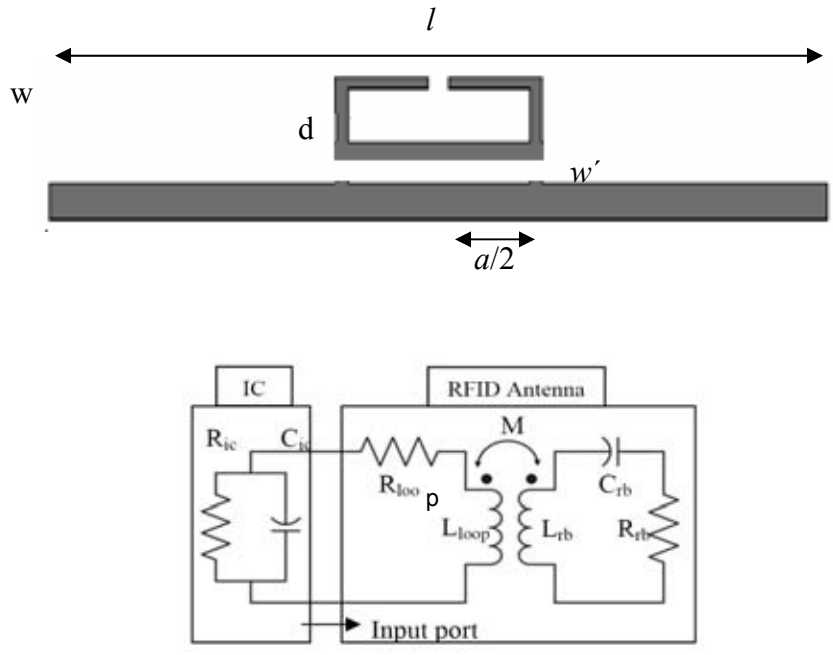

Figure 2.3: The inductively-coupled structure and the equivalent circuit.

The inductively-coupled structure can be modeled as a transformer. Figure 2.3 depicts the equivalent lumped element model, where R_{rb} and R_{loop} are the individual resistances of the radiating body and the feed loop. M is the mutual inductance and L_{loop} is the self-inductance of the feed loop. R_p and C_p are representing the substrate effects.

Compared with the serial stub feed structure in which off-resonance operation is preferred for better resistance/reactance stability, the inductively-coupled structure is designed at the resonant frequency. This is because at the resonant frequency f_0, assuming that the substrate effect is minimal, the components of antenna input resistance R_{zin} and reactance X_{zin} can be predicted as

$$R_{zin} = \frac{(2\pi f_0 M)^2}{R_{rb}} + R_{loop} \tag{2.2}$$

$$X_{zin} = 2\pi f_0 L_{loop} \tag{2.3}$$

Thus, at the resonant frequency, the resistance is mainly controlled by M and R_{rb}, and the reactance is dependent only upon L_{loop}. In this way, the antenna input resistance and input reactance can be adjusted independently. Figure 2.4 shows an example of the matching chart. The input reactance is nearly unaffected by the loop-dipole distance d. For a fixed loop size, the resistance reduces when the loop-dipole distance increases. Therefore, inductively coupled feeding structures present one of the theoretical optimum solutions to effectively match an antenna to arbitrary chip impedances. A design procedure could initially select the loop size with the purpose of canceling the IC chip's capacitive reactance. Further on, a proper loop-dipole distance, d, could be chosen to match the chip's resistance. To be noticed, the resistance of the inductively-coupled structure can hardly achieve high values. Shape modification of the main radiator is needed to match to some types of IC chips that possess high resistance.

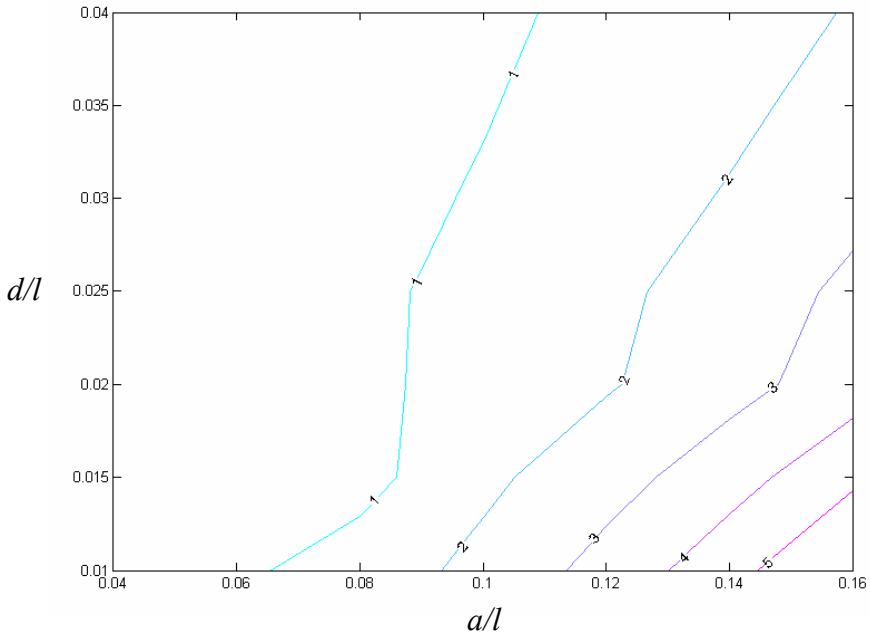

(a)

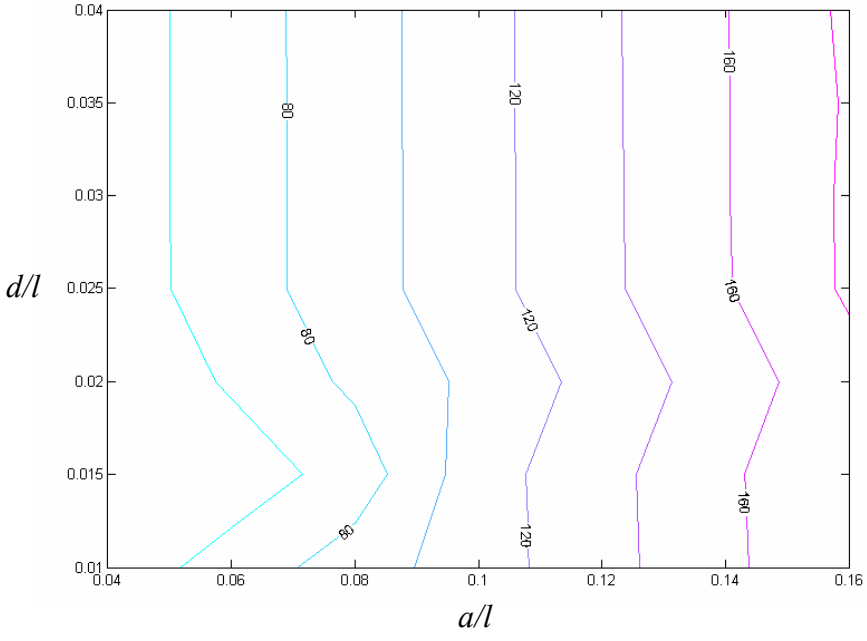

(b)

Figure 2.4: The inductive-coupled structure matching chart for the case of a=b, l=λ/2, w=λ/100, w'=w/2: (a) resistance (b) reactance.

2.1.3 Nested-slot Structure

A useful matching technique for tags fabricated with large planar dipoles or suspended patches [34] is to employ a nested-slot structure, as shown in Figure 2.5. The slot profile can be seen as a slot-line impedance transformer. Depending on the shape and on the size of the internal slot, the antenna acts mainly either as an H slot, a broadband dipole, or as a double folded dipole. In particular, the maximum antenna gain is fixed mainly by the patch length *l*, while the impedance tuning can be changed by the slot dimensions *a* and *b*.

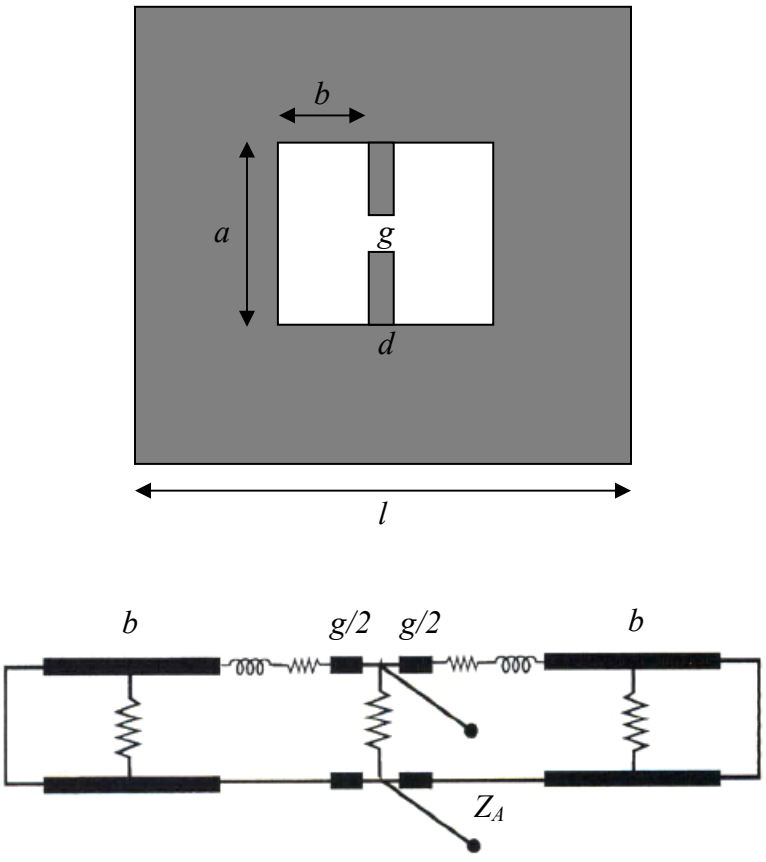

Figure 2.5: The nested-slot structure and the equivalent circuit.

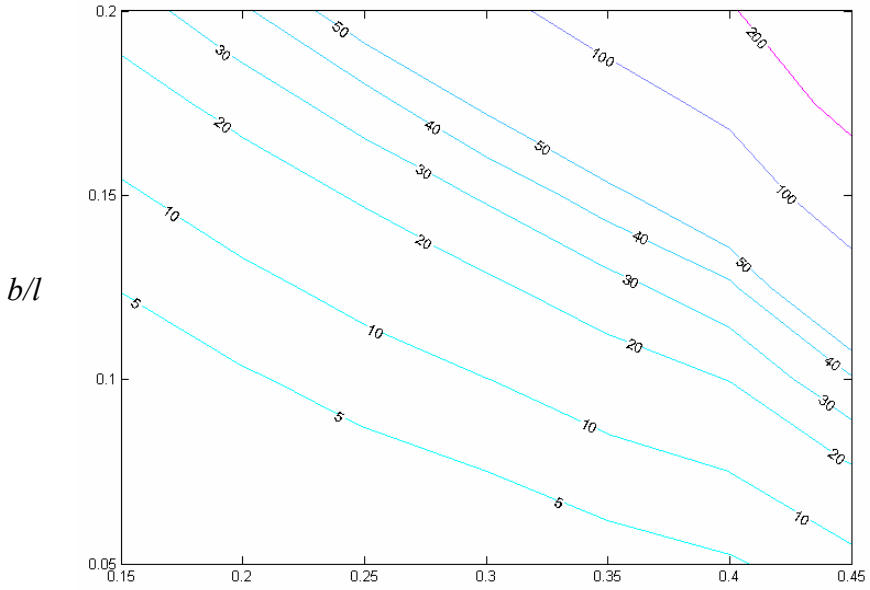

(a)

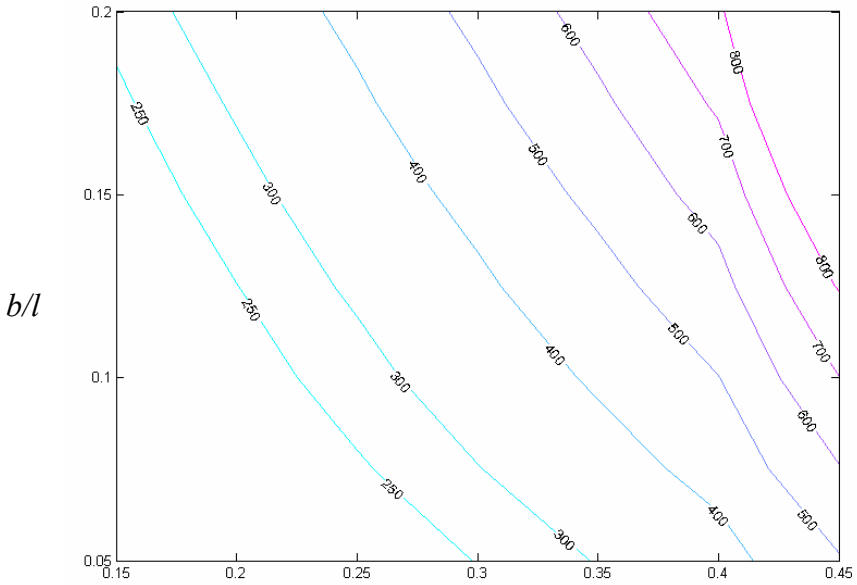

(b)

Figure 2.6: The Nested-slot structure matching chart for the case of l=λ/2, d=g=w=λ/120: (a) resistance (b) reactance.

Figure 2.6 shows the matching chart of the nest-slot structure. It can be observed that the resistance is sensitive mainly to the slot's width *b*, while the reactance presents fast and nearly linear variations along with the sizes of both *a* and *b*. The contour lines in resistance and reactance plots, respectively, are nearly orthogonal. Therefore, broad resistance dynamics can be obtained with a high degree of matching capability.

2.2 Compact RFID Tag using Arc-shape Arms

One of the main challenges in designing a passive RFID is the impedance matching between the terminals of the tag antenna and those of the IC which exhibits complex input impedance. The matching network of the tag has to guarantee the maximum power delivered to the IC which is used to store the data transmitted to and received from the RFID reader. This requires a conjugate matching technique, such as a serial stub feed structure [24].

In the serial stub feed structure, the dimensions of the resistive and inductive stubs are comparable with the main radiating body. These stubs limit the miniaturization of the antenna size. For an ultra-compact RFID antenna design, a matching technique without any stubs is highly preferred. An inductively-coupled feed structure, as illustrated in Figure 2.7, is such an effective way for impedance matching.

Several inductively coupled RFID antenna prototypes with meander line arms have been proposed in the past [35][36]. However, the typical resistance of such antennas can hardly achieve high values in practice, limiting their use to a limit number of tag chips. Up to now, no inductively coupled antenna input resistance higher than 50Ω has been reported based on meander line arms configurations. Without loss of generality, in this design the overall matching network is designed to conjugately match an RFID chip with a high capacitive impedance of Z_{IC}=73-j113 Ω. An ultra-compact inductively-coupled feed antenna was designed in an area less than 1.7 in x 1.4 in, as illustrated in Figure 2.7.

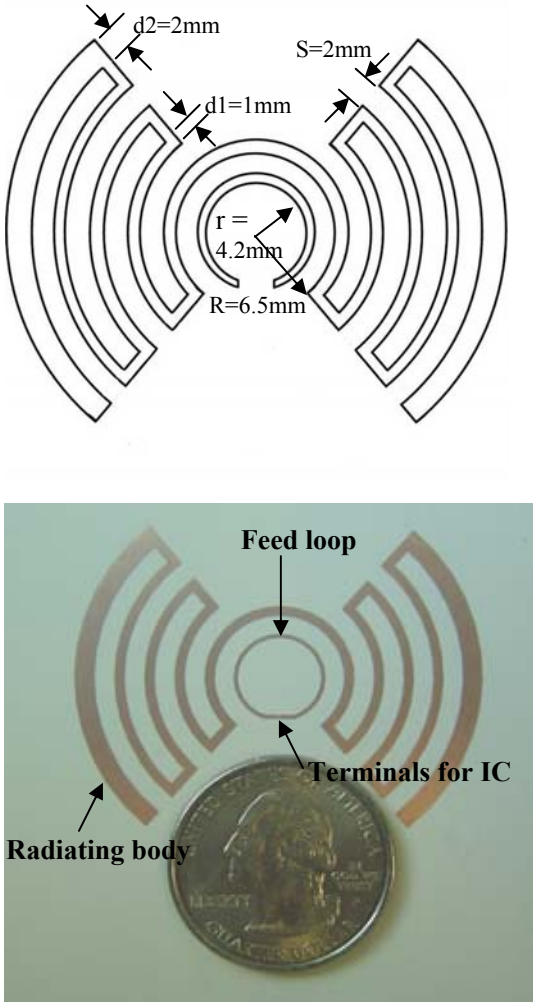

Figure 2.7: Schematic layout and photograph of the inductively-coupled feed antenna fabricated on LCP substrate.

Its arc-shape arms will effectively reduce the intrinsic resistance of the radiating body, resulting in the increase of antenna input resistance in inverse proportion. The substrate was a flexible 4mil LCP that has a dielectric constant ε_r of 3.10 and a loss tangent $tan\delta$ of 0.0019. Since the inductively-coupled feed structure is designed at the resonant frequency, the impedance response is sharper than the one in a serial stub structure, resulting in a narrower bandwidth. Therefore, the inductively-coupled antenna is more applicable to operate at specific bands. In this case, the antenna was designed to cover the European

RFID band, ranging from 865 MHz to 868 MHz. It has to be noted that the performance of this design is quite insensitive to fabrication tolerances and variations.

In Equation 2.2, R_{loop} is typically small, therefore, resistance is mainly controlled by M and R_{rb}. The arc-shape configuration significantly reduced the value of R_{rb}, resulting in higher R_a. To verify this effect, meander line arms with the same line width and spacing were also modeled. The equivalent circuit was optimized with the ADS simulation software, so that the model data and the impedance data calculated by Method of Moment (IE3D Package) align precisely. The lumped element values are shown in Table 2.1. It can be seen that only the radiating body resistance R_{rb} is significantly influenced by introducing the arc-shape structure. R_{rb} is decreased from 21.4 Ω to 3.67 Ω and the antenna input resistance R_a is increased from 20.5 Ω to 76.4 Ω, reaching the range of desired value.

Table 2.1: Lumped element values for different inductively coupled feeding antennas

Sample	Rrb (Ohm)	Crb (pF)	Lrb (nH)	Lloop (nH)	M (nH)	Rloop (Ohm)	Impedance (Ohm)
Arc-shape	3.67	0.72	42.0	21.4	3.0	0.35	76.4+j102.8
Meander line	21.4	0.57	54.3	20.3	3.3	0.1	20.5+j113

The lumped element values of the equivalent circuit optimized by ADS simulation software include the substrate effects. It can be seen that the model data and the full wave simulated impedance data demonstrate very good agreement, as shown in Figure 2.8.

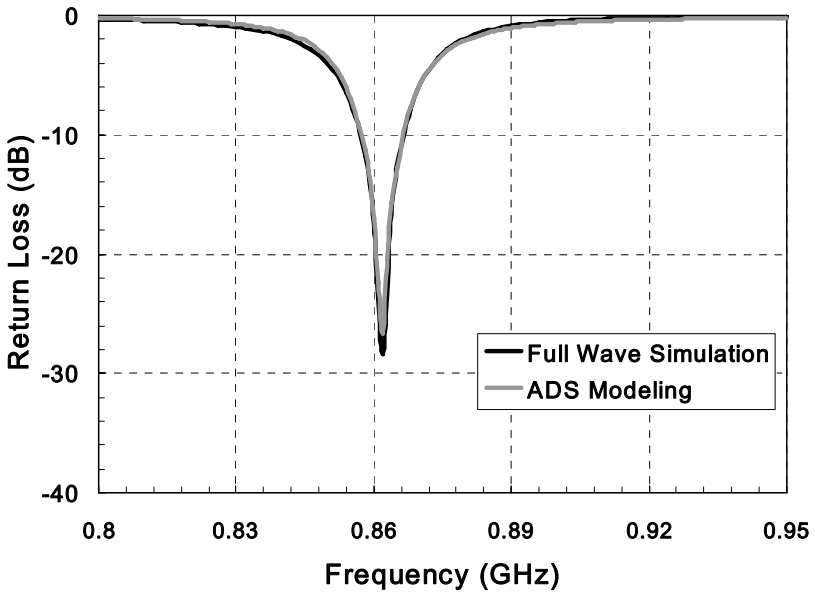

Figure 2.8: Comparison of return loss full wave simulation results with ADS modeling.

The measured and simulated input impedances of the antenna in the interested band are illustrated in Figure 2.9. At 866 MHz, a measured input impedance of 60.8+j102.5 Ω is achieved, resulting in a -30 dB return loss at that frequency. The return loss below -10 dB extends from 858 MHz to 869 MHz, covering the whole European UHF band which extends from 865 MHz to 868 MHz and accounting for most fabrication variations, as shown in Figure 2.10.

Since the radiating body is basically a λ/2 dipole, the radiation pattern looks similar to the one of a dipole, as shown in Figure 2.11. A directivity of 2.09 dBi is achieved with 90.4% radiation efficiency.

An important performance criterion for RFID tag is its read range – the maximum distance at which tag can be detected. In free-space propagation environment, the read range of a tag can be derived from Friis free-space equation [20], as

$$r = \frac{\lambda}{4\pi}\sqrt{\frac{EIRP \cdot G \cdot \tau}{P_{th}}} \tag{2.4}$$

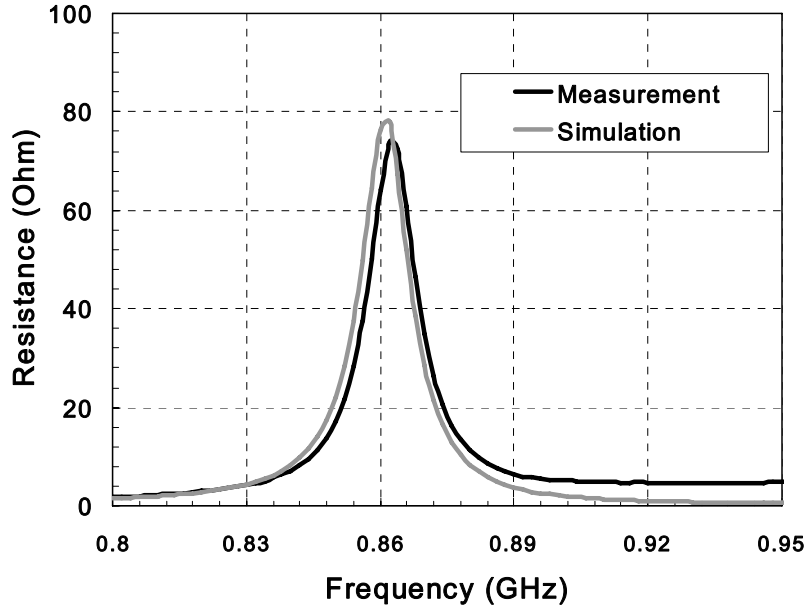

(a)

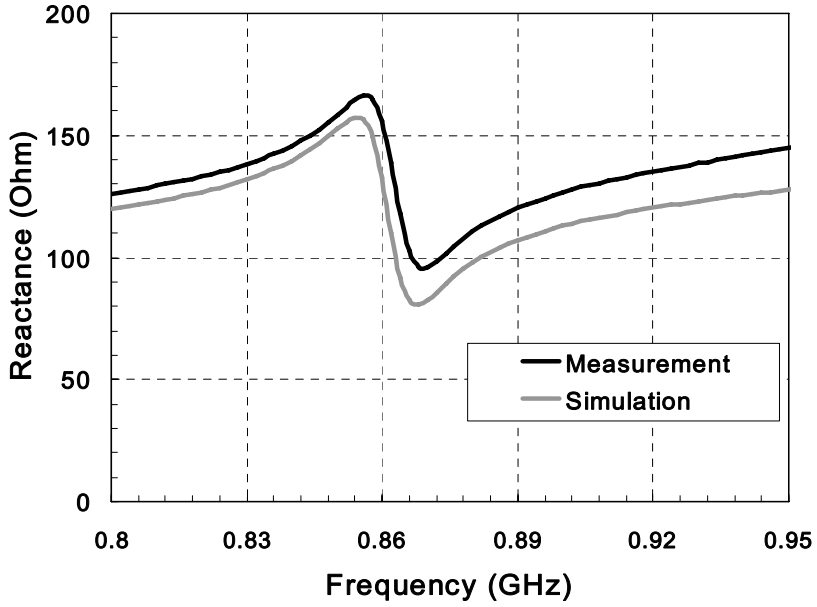

(b)

Figure 2.9: Measured and simulated data of input impedance: (a) Resistance (b) Reactance.

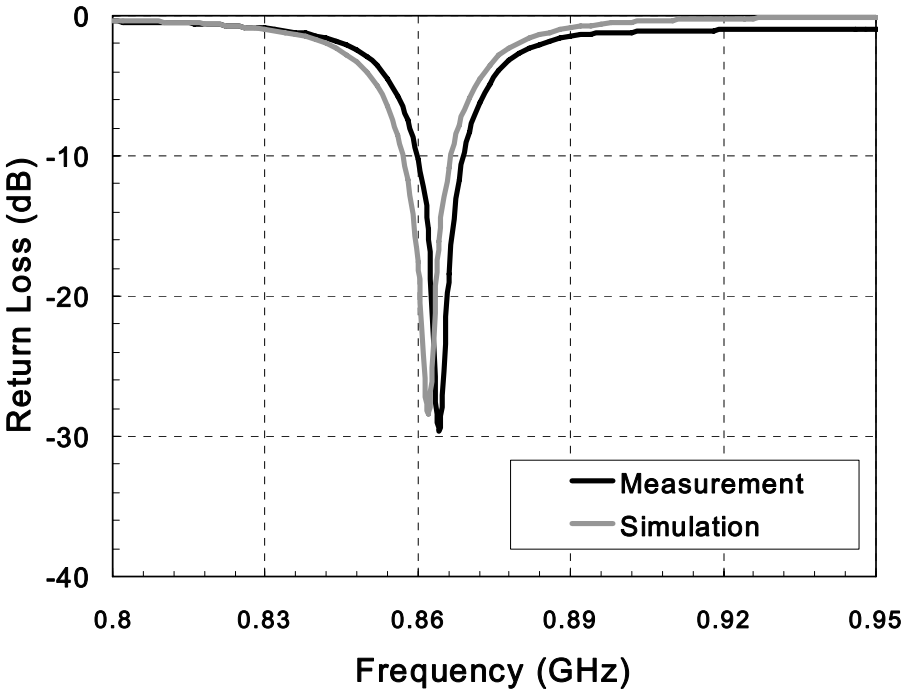

Figure 2.10: Measured and simulated data of return loss.

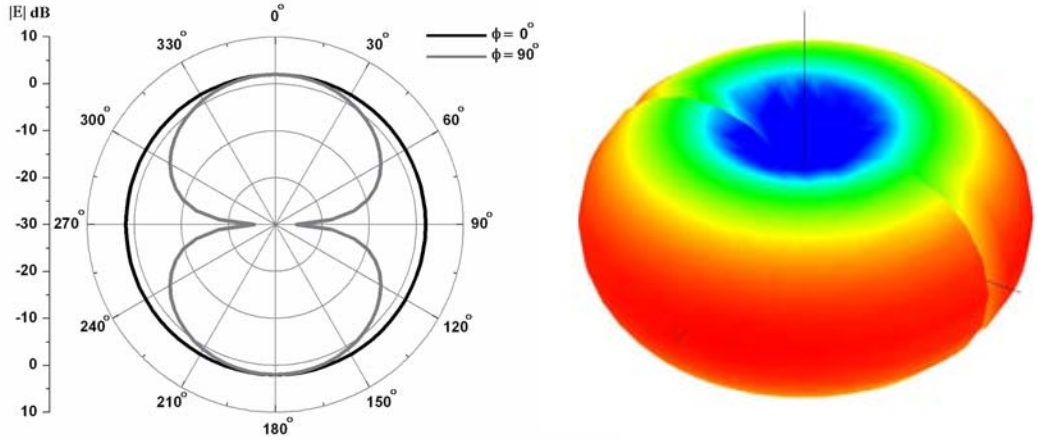

Figure 2.11: 2D and 3D far-field radiation plot.

where the equivalent isotropic radiated power is denoted as EIRP, G is the antenna gain, which equals the antenna directivity D multiplied the radiation efficiency η, τ is the power transmission coefficient between the tag antenna and the RFID IC chip, and P_{th} is the threshold or minimum power needed to activate the RFID IC chip. The values are summarized in Table 2.2.

Table 2.2: Arc-shape RFID tag key parameters

EIRP	Gain (G)	Antenna (Z_{ant})	Chip (Z_{IC})	τ	P_{th}
4 W	1.65 dBi	74+j117 Ω	73-j113 Ω	0.99	-13 dBm

The calculated read range is 8.9 m. This is the case for linearly polarized reader antenna. For circularly polarized reader antenna, the circular-to-linear polarization mismatch would sacrifice -3 dB power loss. In this case the read range would be $1/\sqrt{2}$ times shorter, as 6.3 m.

As illustrated in the arc-shape RFID tag, the inductively coupled matching method leads to ultra-miniaturized sizes, making it suitable for tagging small items. In addition, the approach for antenna arms folding provides optimum current flow and high radiation efficiencies. The presented antenna structures can supply higher resistance to realize conjugate match with some types of tag chips. Inductively coupled RFID antennas with up to 70 Ω input resistance have been first time reported.

2.3 Dual-radiating-body RFID Tag with High Directivity

In majority of applications the tag is allowed to appear in almost arbitrary position in the field of the reader antenna. An omnidirectional radiation pattern, which is usually generated by a dipole-shape antenna, is widely adopted in RFID tag designs. As a trade off to the omnidirectional performance, such antenna does not have a high directivity and can hardly exhibit long-range performance. In some specific applications, such as in the

conveyor belt or loading dock situations as shown in Figure 2.12, the tags and reader antenna placement are fixed, high directivity antenna performance is therefore more preferred to the omnidirectional reading ability, in order to boost the reading range or equivalently minimize the reader power consumption on the same reading distance. Some research has been reported by adding loading bars to the dipole structure to distort the radiation pattern towards a directional shape [37], but the directivity enhancement achieved is limited, usually less than 2.0 dBi, due to the weak coupling.

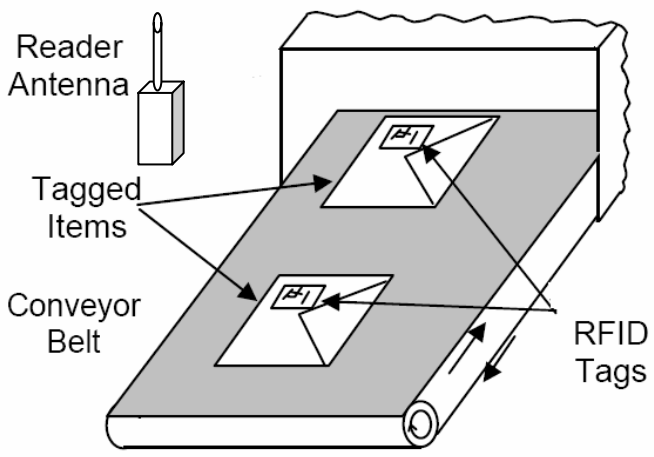

Figure 2.12: RFID conveyor belt application.

Inductively-coupled structure provides the opportunity to feed more than one radiating element at the same time. Each radiating element will directly couple with the feeding loop and have a strong coupling. Figure 2.13 shows the configuration of the dual-radiating-body antenna. Two meander line arms are placed on each side of the feeding loop. Each radiating body functions as a dipole. Especially, the current directions excited on the arms are opposite along them. Therefore, on the direction of z-axis, the radiation patterns cancel out each other and the added field appears to be zero. The radiation pattern is shown in Figure 2.14. The radiating energy is focused directionally in a dumbbell shape and a high gain of 5.03 dBi is observed. The target chip impedance is Z_{IC}=30-j172 Ω.

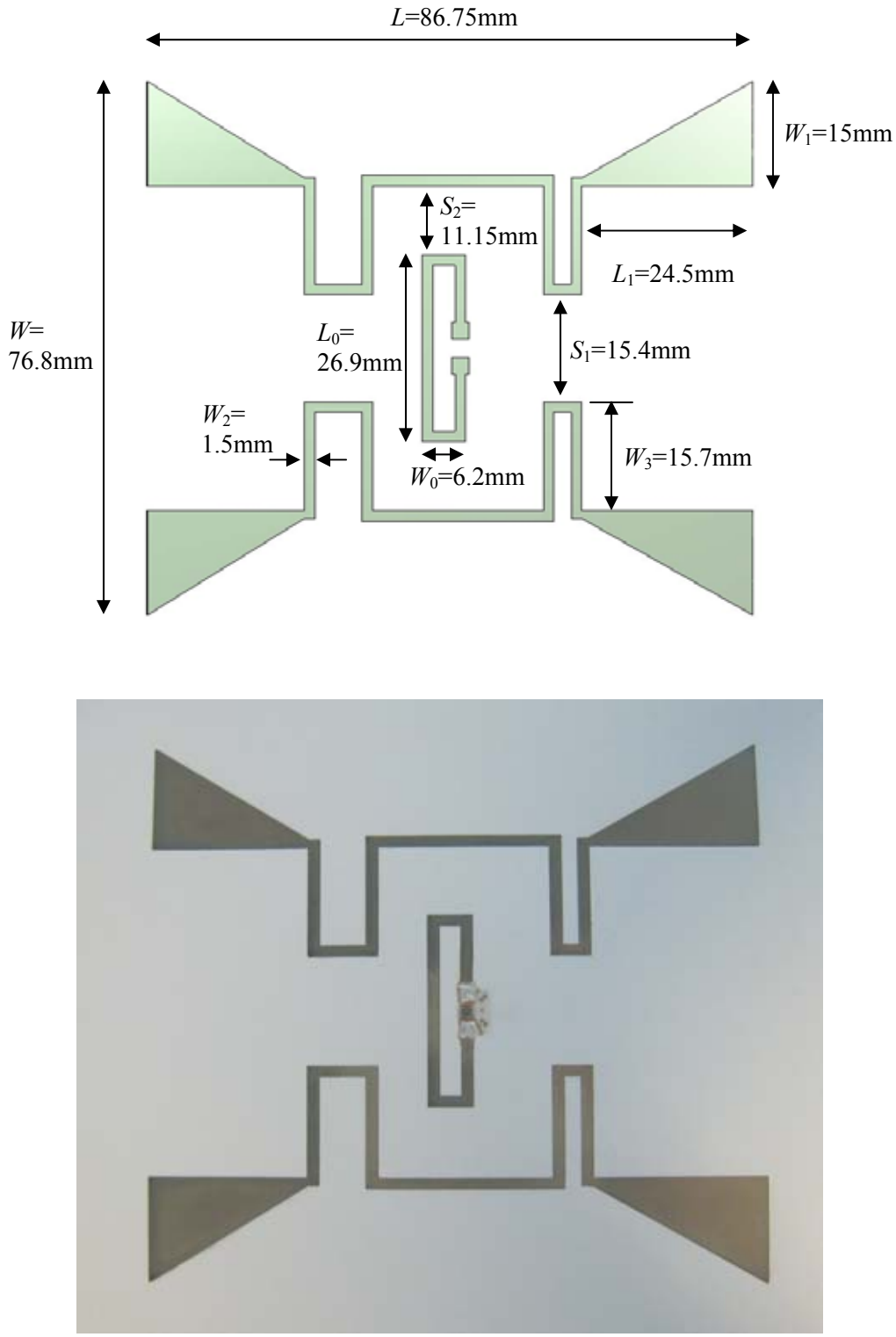

Figure 2.13: Schematic layout and photograph of the dual-radiating-body RFID antenna.

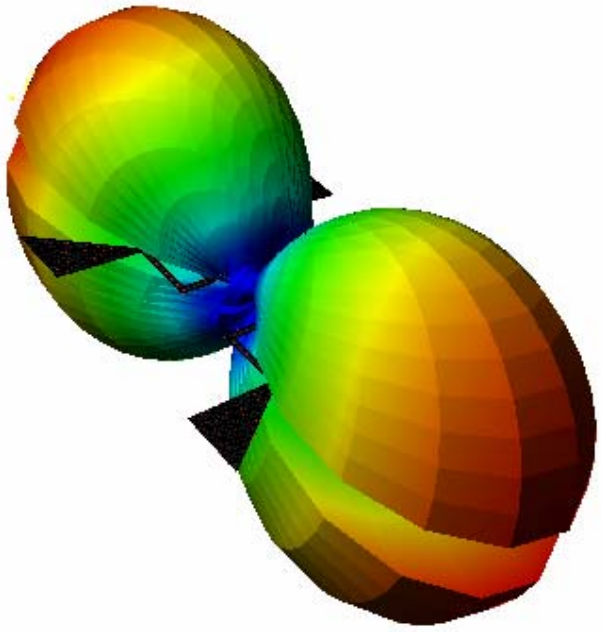

Figure 2.14: Far-field radiation pattern of the dual-radiating-body antenna.

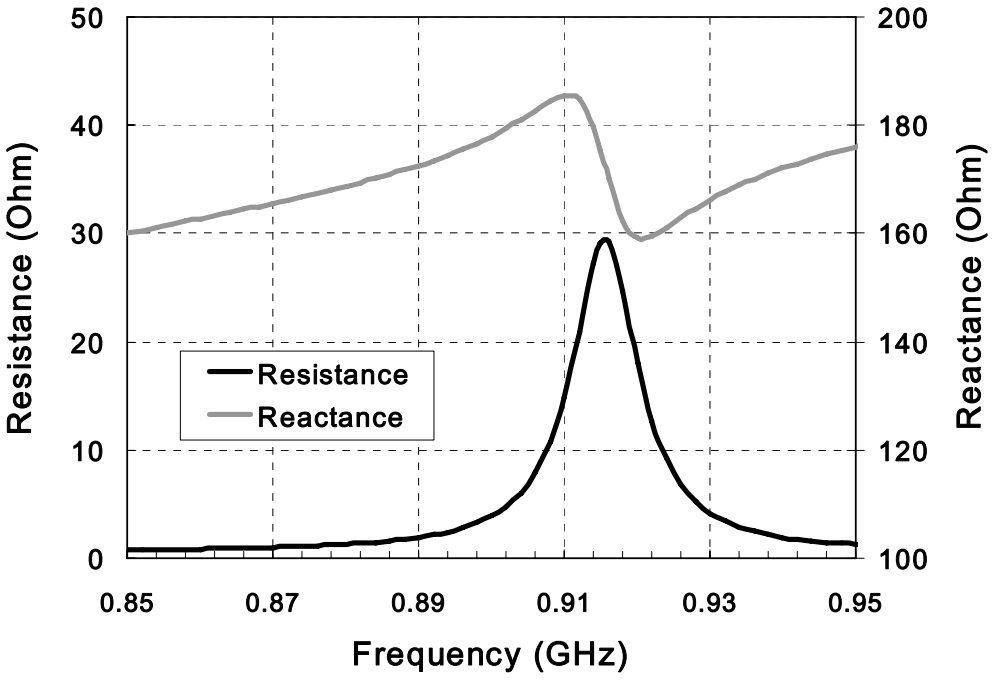

Figure 2.15: Resistance and reactance plot of the dual-radiating-body antenna.

The antenna input impedance plot is depicted in Figure 2.15. The impedance of the proposed antenna is 29.1+j175.2 Ω at 915 MHz. A -29.8 dB return loss, or power transmission coefficient of 0.99, is achieved at 915MHz, as shown in Figure 2.16.

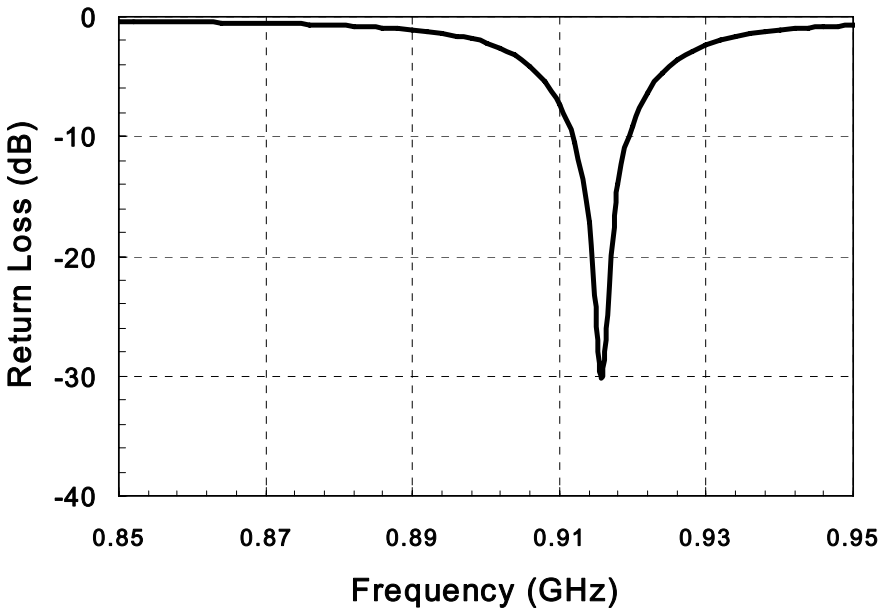

Figure 2.16: Return loss plot of the dual-radiating-body antenna.

Table 2.3: Dual-radiating-body RFID tag key parameters

EIRP	Gain (G)	Antenna (Z_{ant})	Chip (Z_{IC})	τ	P_{th}
4 W	5.03 dBi	29.1+j175.2 Ω	30-j172 Ω	0.99	-15 dBm

The key values of the dual-radiating-body RFID tag antenna are summarized in Table 2.3. Owing to the high directivity, the reading distance of the proposed tag is strongly enhanced. The calculated read range is 16.5 m with a linearly polarized reader antenna, or 11.7 m with a circularly polarized reader antenna considering the -3 dB circular-to-linear polarization mismatch. Measurements have been carried out in an outdoor environment using a commercial circularly polarized reader antenna. The reference power P_{ref} transmitted by the reader antenna is at 20% of the maximum allowed

power $P_{\max}$ (an EIRP of 4 W). This set up helps minimizing the ground interference [38]. The maximum read range can be calculated from

$$r_{\max} = r_{ref} \sqrt{\frac{P_{\max}}{P_{ref}}} \tag{2.5}$$

where $r_{\max}$ is the maximum read range, r_{ref} is the actual distance between the reader and tag antenna. The measured maximum read range is 10.4 m with the circularly polarized antenna, which is close to the theoretical range.

2.4 Microstrip RFID Tag for On-Metal Operation

Most commercial UHF RFID tags are based on the dipole antenna, and it is well known that tag performance degrades significantly when the tag is placed near a conducting surface [39]. This is an unfortunate situation, since industry continues to seek a low-cost way to tag metal assets, like cargo containers. Often, industry simply provides a 3-6 mm thick low-dielectric material such as a foam substrate in order to provide enough separation from the metal surface to provide adequate, though severely degraded, performance. A foam separation of 3.2 mm above metal surface can yield a performance degradation of 16 dB or more over free-space performance of a dipole-based RFID tag, resulting in a reduction in read range of about 85% [40].

Microstrip patch antennas are a well-known class of antennas that exhibit good performance for on-metal operation. A microstrip antenna consists of a primary radiating element, a dielectric substrate, a ground plane, and a feeding element. The feeding structure is based on some sort of unbalanced transmission line, either a coaxial cable with a probe feed, or a microstrip transmission line with an edge feed. The need to establish an electrical reference complicates the structure, usually requiring a via to the ground plane [41]. The via significantly complicates the manufacturing process and increase the cost of the RFID tag which has been the bottle neck of a pervasive RFID application.

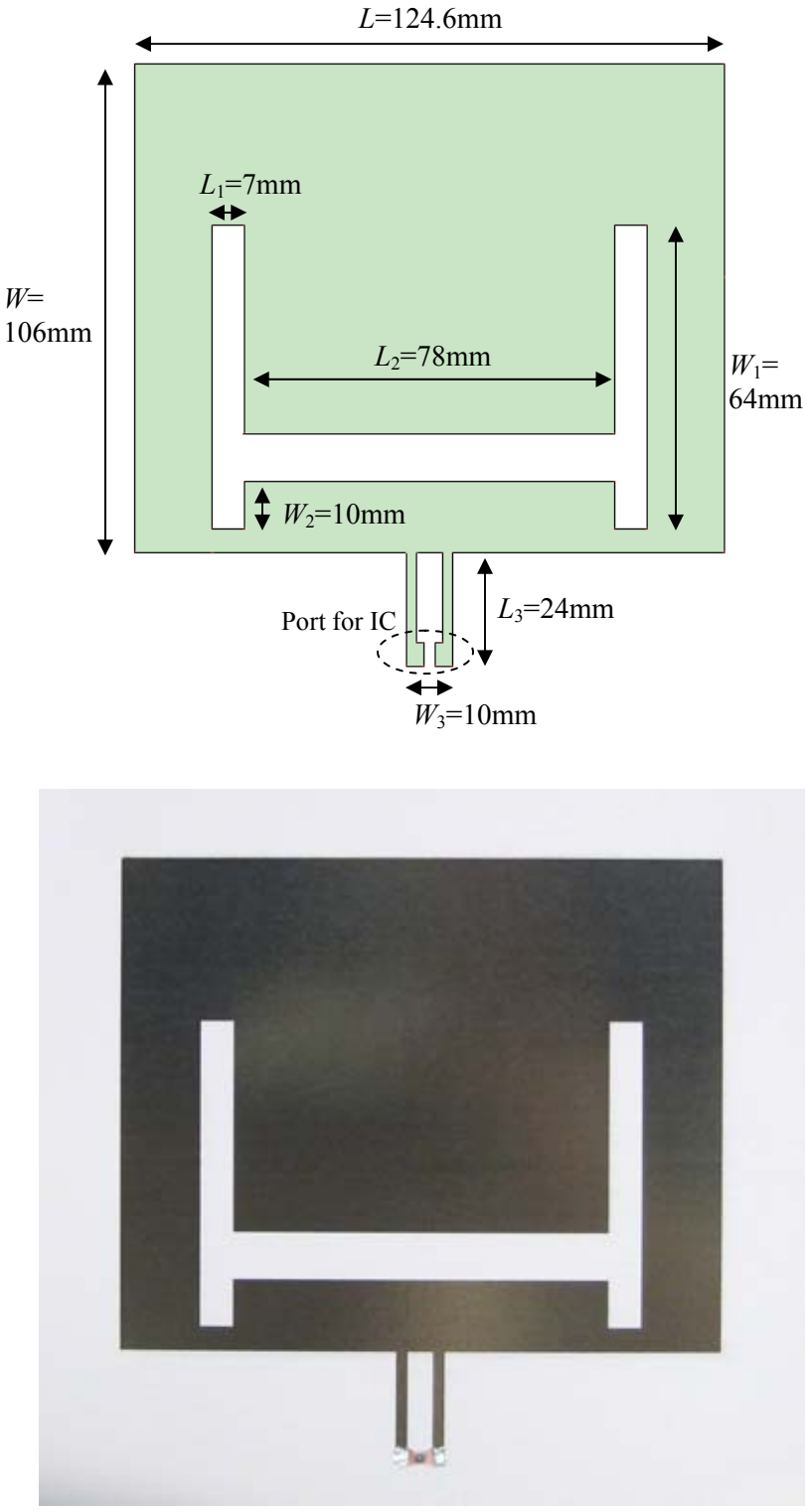

Figure 2.17: Schematic layout and photograph of the microstrip RFID antenna.

The T-match structure is widely used in dipole-shaped antennas as an impedance tuning method to provide a conjugate match to the IC chip impedance. A microstrip antenna with T-match feed on the edge was proposed in this section for the RFID on-metal operation. Figure 2.17 shows the antenna geometry, where the IC chip is connected in the center of the T-match lines on the coplanar surface of the microstrip antenna. The antenna was inkjet-printed on a 170 μm paper substrate, and then stacked on a 5.3 mm thickness foam with dielectric constant 1.04. The H-shape slot lengthened the current path on the patch surface and shifted down the frequency. Therefore, the patch size was reduced significantly. As a comparison, an uncut patch resonating at the same frequency has the dimensions of 147.4 mm x 135 mm, an area 50.7% larger than the H-shaped slot antenna's.

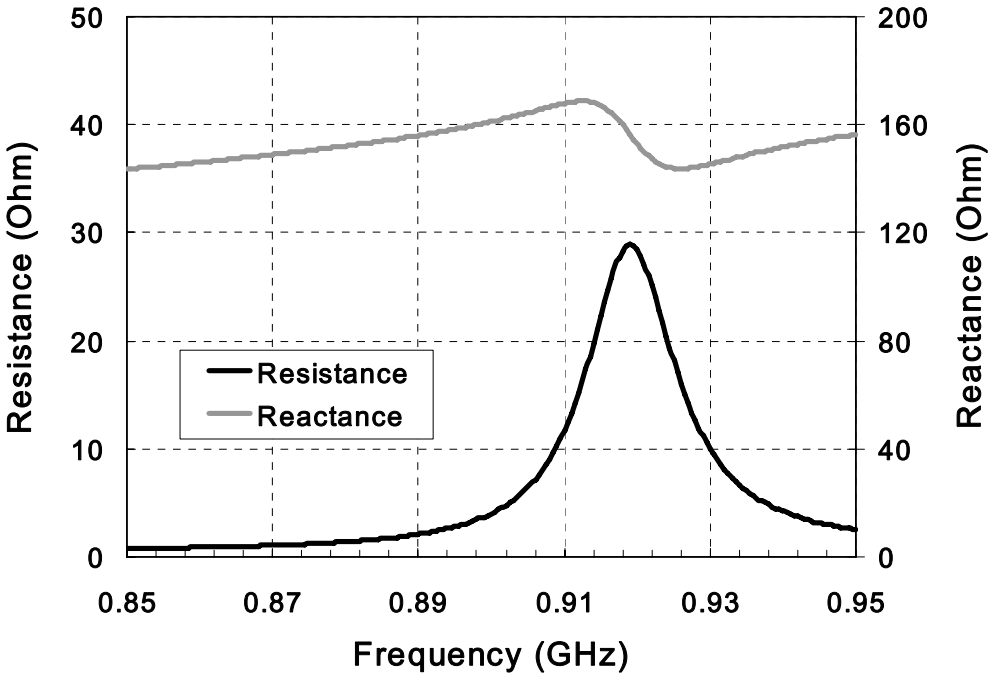

Figure 2.18: Resistance and reactance plot of the microstrip RFID antenna.

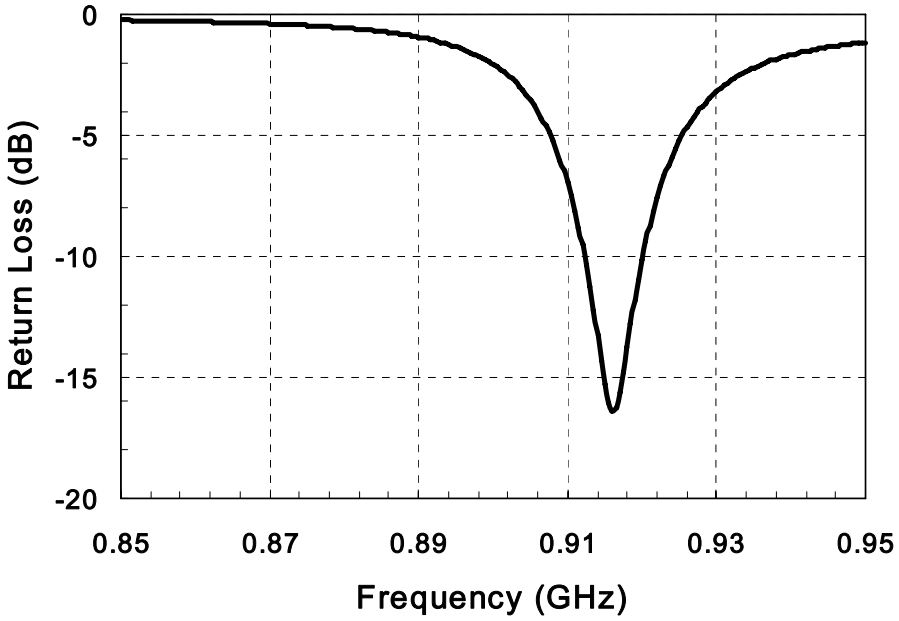

Figure 2.19: Return loss plot of the microstrip RFID antenna.

The substrate and ground dimensions are 18 cm x 18 cm. The antenna input impedance plot is depicted in Figure 2.18. The impedance of the proposed antenna is 22.3+j167.2 Ω at 915 MHz. A -16.25 dB return loss, normalized from the Z_{IC}=30-j172 Ω IC chip impedance, or equivalently power transmission coefficient of 0.97, is achieved at 915 MHz, as shown in Figure 2.19. The radiation pattern is shown in Figure 2.20. As a typical microstrip antenna, the radiating pattern is focused along the z-axis and a high gain of 7.40 dBi is observed.

The key values of the microstrip RFID tag antenna are summarized in Table 2.4. The calculated read range is 21.4 m with a linearly polarized reader antenna, or 15.16 m with a circularly polarized reader antenna considering the -3 dB circular-to-linear polarization mismatch. The fabricated antenna was placed on a 1.5 m x 1 m ground plane. The same set up as in the dual-radiating-body antenna read range measurement was applied. The measured maximum read range is 14.5 m with the circularly polarized antenna. The slight range decrease may be due to the non-uniformity of the foam

substrate thickness that will affect the input impedance of the antenna. Overall, good agreement between the measurement and the theoretical results is observed. To be noticed, the microstrip RFID antenna also exhibits robust performance when tagged on different material surfaces owing to the shielding from the ground plane. The same tag was placed outside of a water container, and 14.2 m read range with the circularly polarized antenna was measured. The performance of this prototype has been compared to other commercial RFID tag for metallic applications. The read range performances were summarized in Table 2.5.

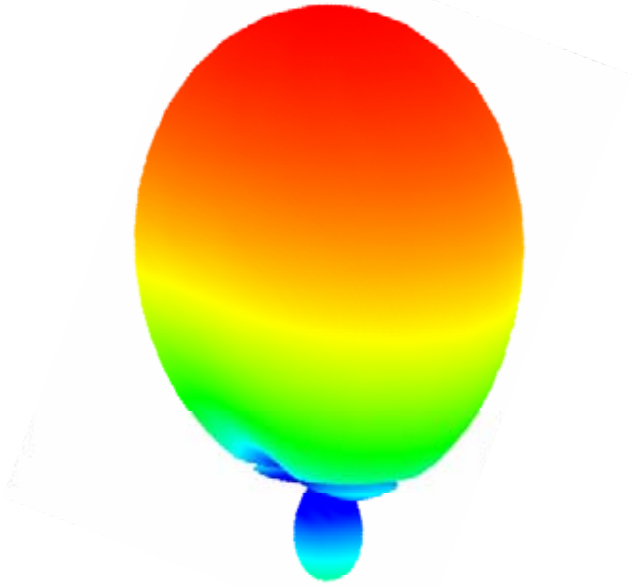

Figure 2.20: Far-field radiation pattern of the microstrip RFID antenna.

Table 2.4: Microstrip RFID tag key parameters

EIRP	Gain (G)	Antenna (Z_{ant})	Chip (Z_{IC})	τ	P_{th}
4 W	7.40 dBi	22.3+j167.2 Ω	30-j172 Ω	0.97	-15 dBm

Table 2.5: Comparison of the read range of different commercial tags

	Microstrip Tag	Intermec IT65L	Intermec IT65S	Alien ALN-9540
Metal Surface	14.5 m	12.2 m	6.3 m	< 1 m
Water Container	14.2 m	10.1 m	4.7 m	< 1 m

* 4W EIRP, circularly polarized reader antenna

2.5 Chapter Summary

The RFID antenna impedance-matching techniques were investigated in this chapter. Three passive UHF RFID tag modules, namely arc-shape inductively-coupled RFID tag, dual-radiating-body RFID tag, and microstrip RFID tag, are then developed, targeting at different performances – compact size, high directivity, and ability to tag metallic objects. The proposed RFID tag configurations can find attractive applications in many services in the industry.

CHAPTER 3

INKJET-PRINTED RFID TAG ON PAPER SUBSTRATE

In this chapter, inkjet-printed RFID tags fabricated on paper substrates are investigated as an approach that aims for a system-level solution for fast and ultra-low-cost mass production. First, the RF characteristics of the paper substrate are studied by using the microstrip ring resonator and the cavity resonator methods in order to characterize the relative permittivity (ε_r) and loss tangent ($tan\delta$) of the substrate at UHF band. A UHF RFID tag module is then developed with the inkjet-printing technology, proving this approach could function as an enabling technology for much simpler and faster fabrication on paper. Simulation and well-agreed measurement results, which show very good agreement, verify a good performance of the tag module. In addition, the investigation of minimizing the conductive ink usage by reducing solid printed surfaces with alternative designs, while maintaining the tag antenna performance is achieved.

3.1 Motivation

With the growth of demand for low-cost, flexible and power-efficient broadband wireless electronics, the materials and integration techniques become more and more critical and face more challenges, especially with the ever increasing interest for "cognitive intelligence" and wireless applications, such as 3G/4G communication systems and WiMax. This demand is further enhanced by the need for inexpensive, reliable, and durable wireless RFID-enabled sensor nodes that is driven by several applications [42], such as logistics, Aero-ID, anti-counterfeiting, supply-chain monitoring, space, healthcare, pharmaceutical, and is regarded as one of the most important methods for realizing ubiquitous ad-hoc networks.

Paper-based electronics has drawn increasing attention in the fields where cost is the major consideration in applications, such as RFID area [43]. Paper is considered one of the best organic-substrate candidates for UHF and microwave applications, while it features the industrial ability to be processed in a reel-to-reel fashion [44]. Needless to mention that paper is also environmentally friendly and one of the lowest cost materials used in the industry in terms of mass production. Paper can easily obtain a low surface profile with the application of appropriate coatings, which can enable the utilization of direct write methodologies such as inkjet-printing, to be used in replacement of relatively expensive wet-etching techniques. Such a fast process can be used to print electronics on the surface of paper substrate or even embedded in a multilayer fashion. In addition, paper can be made hydrophobic and/or fire-retardant by adding certain textiles.

However, there are hundreds of different paper materials available in the commercial market, varying in density, coating, thickness, texture, etc. Each has its own RF characteristics. Some characterization work has been reported in frequencies below the UHF band [16][17][18], but none in or above UHF band. Therefore, the RF characterization of paper substrate becomes a must for optimal designs utilizing this low-cost substrate, as well as the demonstration of the use of inkjet-printing process in the development of paper-based RFID tags.

3.2 Inkjet-printing Technology

There is a strong need in industry for rapid prototyping and "just in time methods", materials, and tools to direct write passive circuit elements on various substrates, especially in the mesoscopic regime, which is electronic devices that straddle the size range between conventional microelectronics (sub-micron range) and traditional surface-mount components (10-mm range) [45]. The need is based on the desire to: (1) rapidly fabricate prototype circuits without iterations in photolithographic mask design; (2) reduce the size of PCBs and other structures by conformally incorporating passive circuit

elements into the structure; (3) fabricate parts of electronic circuits by methods that occupy a smaller production scale footprint, which are Computer-aided Design (CAD) compatible, and that can be totally controlled from the designers' computer to the working prototype. The savings in time is especially critical to the quick-changing electronics market of today.

Inkjet printing is a direct-write technology by which the design pattern is transferred directly to the substrate, and there is not requirement of masks compared with the traditional etching technique which has been widely used in industry. Being data driven directly from CAD information and stored digitally, it is thus flexible. Piezoelectric dispensing technology used in the inkjet printing is adaptable to a wide range of material dispensing applications, such as biomedical reagents, liquid metals, and optical polymers. Besides, unlike etching that is a subtractive method of removing unwanted metal from the substrate surface, inkjet-printing jets a single ink droplet from the nozzle to the desired position; therefore, no waste is created, resulting in an economical fabrication solution. As an additive process with no chemical waste, it is environmentally friendly.

Inkjet printing technology has been developed over the past fifty years for low-cost and high-quality office printers, for industrial marking applications and for specialty applications. Electronics manufacturing and solid free-form-fabrication applications drove initial developments of inkjet printing technology for novel applications during the 1980s. Most recently, photonics, micro-electromechanical systems (MEMS), wireless communication, and portable electronics are driving forces in the adaptation of inkjet printing technology. Large format inkjet printers, the fastest growing segment in the inkjet printer industry, have enabled low-cost, rapid response signage.

There are two types of inkjet printing, one is the continuous mode inkjet technology, and another is the demand mode inkjet technology.

Figure 3.1 shows a schematic of the continuous mode inkjet-printing system. The

drop breaks off from the jet in the presence of an electrostatic field, referred to the charging field, and thus acquires an electrostatic charge. The charged drops are directed to the either the catcher or the desired location on the substrate by another electrostatic field, the deflection field. This type of system is given the name of "continuous" because drops are continuously produced and their trajectories are varied by the amount of charge applied.

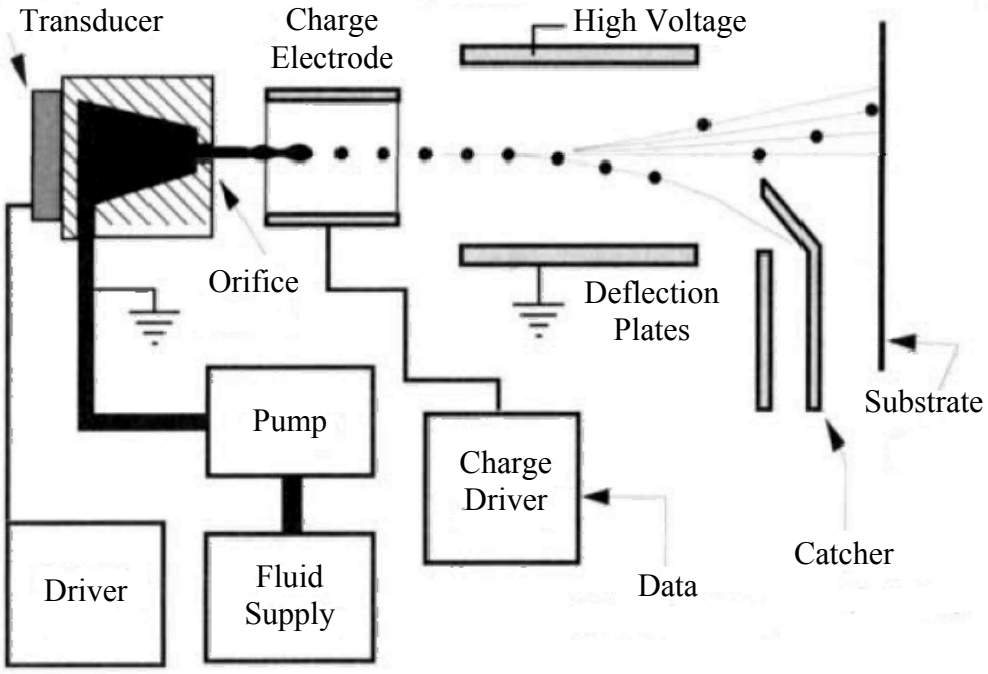

Figure 3.1: Schematic of a continuous mode inkjet-printing system.

Figure 3.2 shows a schematic of a demand mode inkjet-printing system. In this system, a volumetric change in the fluid is induced by the application of a voltage pulse to a piezoelectric material that is coupled, directly or indirectly, to the fluid. This volumetric change causes pressure transients to occur in the fluid and these are directed so as to produce a drop that issues from an orifice. Because the voltage is applied only when a drop is desired, it is referred to as "drop-on-demand."

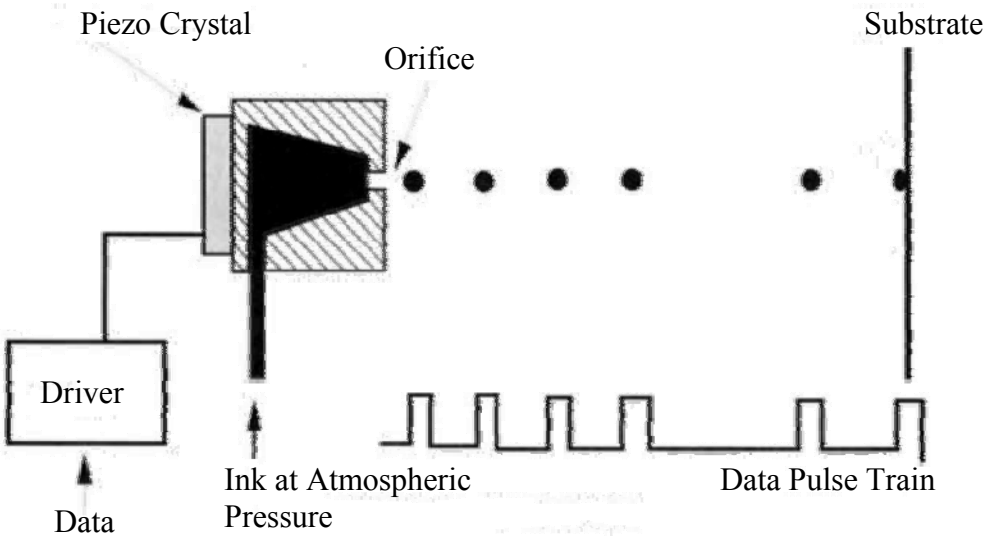

Figure 3.2: Schematic of a demand mode inkjet-printing system.

More specifically, the piezoelectric material, as part of its fabrication, is poled. To accomplish this, a strong electric field is applied to the piezoelectric material and then removed. This results in a poling field with the same orientation as the initial electric field. To actuate the piezoelectric material in extension mode, an electric field (weaker than the field used to pole the piezoelectric material) is applied. If the electric field is applied parallel to the poling field, then the piezoelectric material reacts in extension mode. In extension mode, the piezoelectric material lengthens in one dimension and shortens in the other. If the electric field is applied perpendicular to the poling field, the piezoelectric material reacts in shear mode. In shear mode, the piezoelectric material shears like a deck of cards in one dimension, with no change in the other dimension. By placing electrodes on the surface of the piezoelectric material, a section of the material can be made to move without affecting the surrounding material. By applying a voltage to the center electrode, an electric field is created between the center electrode and the ground electrodes. This creates the shear response in the piezoelectric material between the electrodes. By coupling the piezoelectric material to a pumping chamber that

communicates with a nozzle, an ink drop is formed, as shown in Figure 3.3 (a). The actual motion of the piezoelectric material is approximately one millionth of an inch. Another key element of the printing system is the "lung" [46]. The name derives from the human lung, where active gas exchange takes place in the human body. Lung technology addresses one of the difficulties of inkjet - air and air bubbles. The lung removes air from the ink, which reduces the relative concentration of air in the ink. This allows the ink to quickly dissolve air bubbles in ink passages as well as eliminate sites where air bubbles may be generated, as shown in Figure 3.3 (b). This leads to fast, reliable startups, and enables robust high frequency jetting.

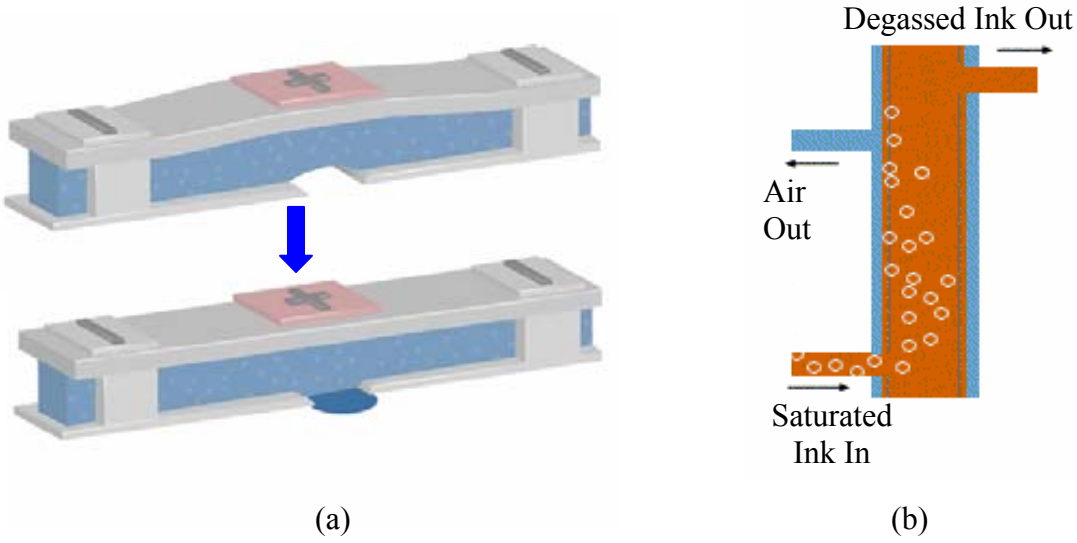

Figure 3.3: Schematic illustration of the key element in a demand mode inkjet-printing system: (a) a pumping chamber coupled with the piezoelectric material (b) the air bubble removing element.

Demand-mode inkjet systems have no fluid recirculation requirement, and this makes their use as a general fluid microdispensing technology more straightforward than the use of continuous mode technology. Besides, piezoelectric demand-mode inkjet printing does not create thermal stress on the fluid, and does not depend on a thermal process to impart acoustic energy to the working fluid, it is the most adaptable of the

inkjet printing technologies to fluid microdispensing in general, and in particular to rapid prototyping applications. In the latter research, demand mode inkjet printing system is applied.

Silver nano-particle inks are usually selected in the inkjet-printing process to ensure a good metal conductivity. Silver ink is sprayed from the cartridge nozzles to the substrate. Manual setting of the nozzle voltage can be applied in order to control the thrust and speed of the ink drops. When the nozzles are not jetting, a voltage is still applied, so that the ink is contained at the edge of the nozzles and is not dripping down to the substrate.

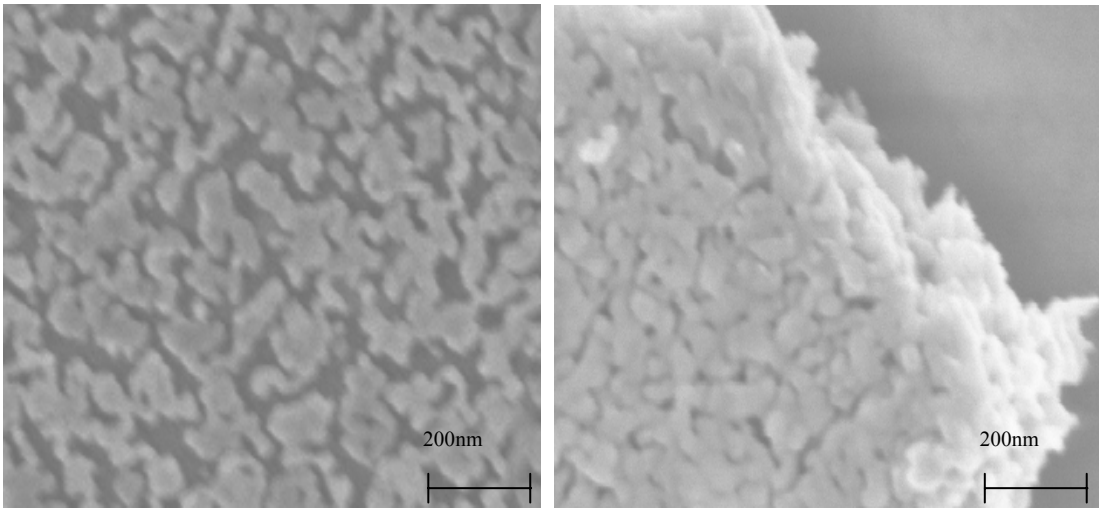

Figure 3.4: SEM images of a layer of printed silver nano-particle ink, after a 15 minutes curing at 100 ^{o}C and 150 ^{o}C, respectively.

After the silver nano-particle droplet is driven through the nozzle, a sintering process is necessary to remove excess solvent and to remove material impurities from the depositions. The sintering process also provides the secondary benefit of increasing the bond of the deposition with the paper substrate [47]. The conductivity of the conductive

ink varies from 0.4~2.5x10^7 Siemens/m depending on the curing temperature and duration time [48]. Figure 3.4 shows the difference between heating temperature 100 ^oC and 150 ^oC after a 15 minutes curing. At lower temperature, a large gap exists between the particles, resulting in a poor connection. When the temperature is increased, the particles begin to expand and gaps start to diminish. This guarantees a virtually continuous metal conductor, providing a good percolation channel for the conduction electrons to flow. The silver nano-particle ink electrical performance versus cure time at temperature in air is shown in Figure 3.5.

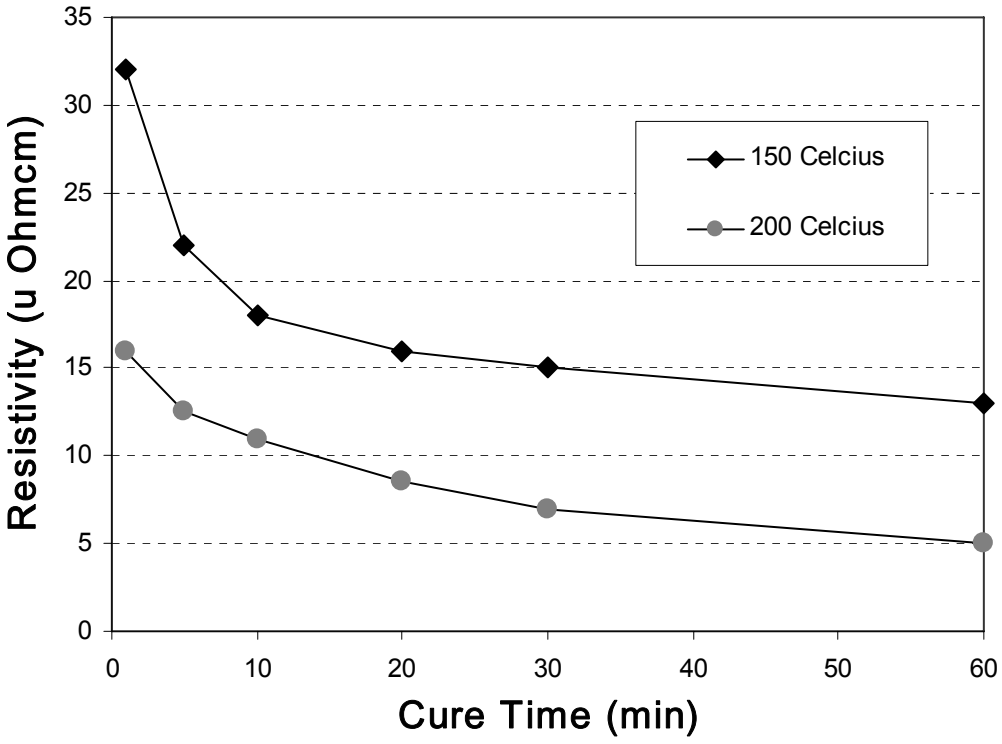

Figure 3.5: Silver nano-particle ink electrical performance versus cure time [48].

There is also a difference between sintering a thin-film layer and a bulk form. The temperature distribution can be assumed to be a constant in a thin-film layer; however, a significant temperature gradient in the bulk form, results in a different conductivity

distribution inside the inkjet-printed layers. The bulk inkjet-printed layer, which allows the realization of the right metal thickness, is the form used to ensure the conductivity performance of RFID modules. A curing temperature of 120 ^{o}C and duration time of two hours was used in the following fabrications to sufficiently cure the nano-particle ink. Alternatively, ultraviolet (UV) curing is widely used in the industry for rapid processing.

3.3 RF Characterization of Paper-based Substrate

Knowledge of the dielectric properties of the paper substrate becomes necessary for the design and modeling of any high-frequency structure such as paper-based RFID antennas. The two most important electrical parameters used to characterize an RF/microwave substrate are the relative permittivity and the loss tangent. Relative permittivity determines the characteristic impedance of transmission lines and the wavelength in the dielectric medium, and affects the performance of the antenna. Loss tangent determines the amount of loss in the dielectric medium and hence determines if a substrate is appropriate for a certain application depending on its power level requirements.

In this effort, a resonator method, namely the microstrip ring resonator method, was selected for the paper characterization. For the first time, a thorough analysis has been performed in order to provide accurate broad band dielectric properties of paper substrates in the UHF frequency band.

The most precise methods for determining RF characteristics of the substrate are the resonator-based methods, including parallel-plate resonators, microstrip ring resonators and cavity resonators. The parallel-plate resonator method is usually applied at low frequencies beneath UHF band [16]. Cavity resonators were proposed for characterization above 30 GHz [43], but have not been preferable in lower frequency

bands due to their large dimensions when the operational wavelength is at the scale of centimeters. When the operational wavelength is at the scale of centimeters, the configurations of microstrip ring resonators are more favorable compared with cavity resonators. Therefore, the microstrip ring resonator method was chosen to be used in the hereby presented paper characterization. In the UHF band, the microstrip ring resonator method provides dielectric information at periodic resonant peaks.

Among the critical needs for the selection of the right type of paper for electronics applications are the surface planarity, water-repelling ability, lamination capability for 3D module development, via-forming ability, adhesion ability, and co-processability with low-cost manufacturing. For the trial runs, a commercially available paper with hydrophobic coating was selected. The thickness of the single sheet of paper is 260±3 μm.

The layout of the microstrip ring resonator is shown in Figure 3.6. The ring resonator produces S_{21} results with periodic frequency resonances. In this method, relative permittivity ε_r can be extracted from the location of the resonances of a given radius ring resonator, while loss tangent $tan\delta$ is extracted from the quality factor of the resonance peaks along with the theoretical calculations of the conductor losses. Since the conductivity of the conductive ink varies with the curing temperature and duration time [49], an 18 μm thick copper foil was selected as the metallic material heat-bonded on both sides of the paper substrate, in order to accurately model and de-embed the conductive loss of the microstrip circuit. The photolithography process was conducted using a dry film photoresist followed by UV exposure and finally etching copper using a slow etching methodology.

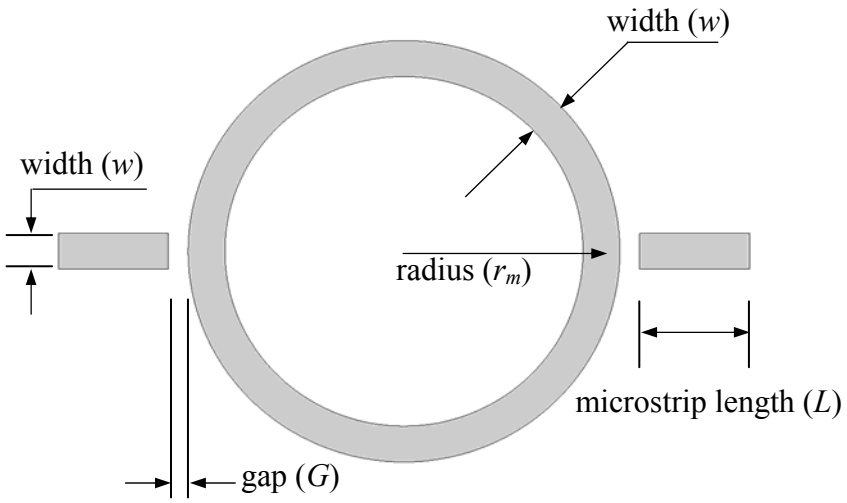

(a)

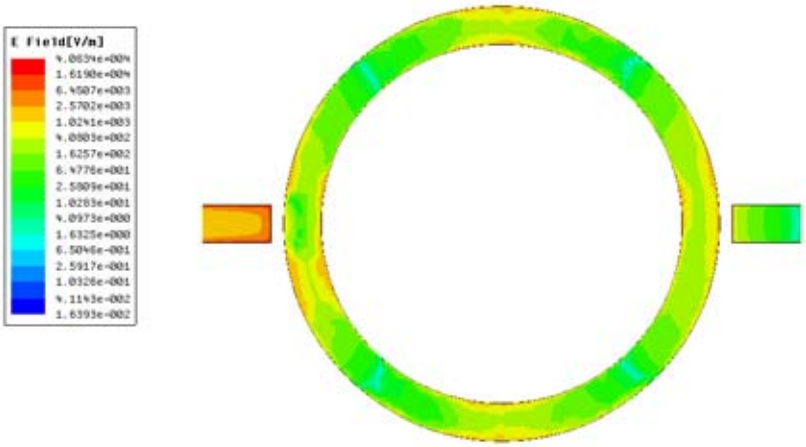

(b)

Figure 3.6: Microstrip ring resonator configuration: (a) schematic diagram (b) current distribution at the resonant peak at 1.4 GHz.

To investigate the sensitivity of the results to the paper thickness as well as to investigate the effect of the bonding process, three sheets and nine sheets of paper were directly heat-bonded together to grow thickness, without any extra adhesive layers. Two microstrip ring resonators were designed and fabricated on these two paper substrates,

respectively. The effects of the input and output feeding lines were de-embedded using the through-reflect-line (TRL) calibration on the TRL lines that were designed to be quarter-wavelength long at different frequencies over the range of measurement [50]. A reference plane was set at the edge of the coupling gap to the resonator. Therefore, only the response of the resonating ring element was effectively measured. The full-wave electromagnetic solver HFSS was used to assist the designs. Ring dimensions and TRL line lengths are shown in Table 3.1.

Table 3.1: Ring resonator and TRL line dimensions

	Ring A	Ring B
Radius of Ring (r_m)	40 mm	39.7 mm
Line Width (w)	7.46 mm	1.6 mm
TRL 1	11.467cm	6.515 cm
TRL 2	9.429cm	4.886 cm
TRL 3	6.288cm	2.44 cm
TRL 4	5.257cm	1.626 cm
TRL 5	3.568cm	1.218 cm
TRL Open	1.58cm	1.03 cm
TRL Short	3.26cm	2.06 cm

The measurements were performed using an Agilent 8530A Vector Network Analyzer (VNA), leading to the values listed in Table 3.2, which feature the peak positions, -3 dB bandwidth, and insertion loss at the resonant frequencies, as shown in Figure 3.7.

Table 3.2: Ring resonator resonant modes

	Resonant Modes	Resonating Freq. (MHz)	BW_{-3dB} (MHz)	Insertion Loss (dB)
Ring A	N=1	711.5	42.4	47.1
	N=2	1408	27.29	42.5
	N=3	2173	64.8	41.1
Ring B	N=1	736.3	56.97	63.2
	N=2	1490	93.92	57.2
	N=3	2243.7	153.3	64.5

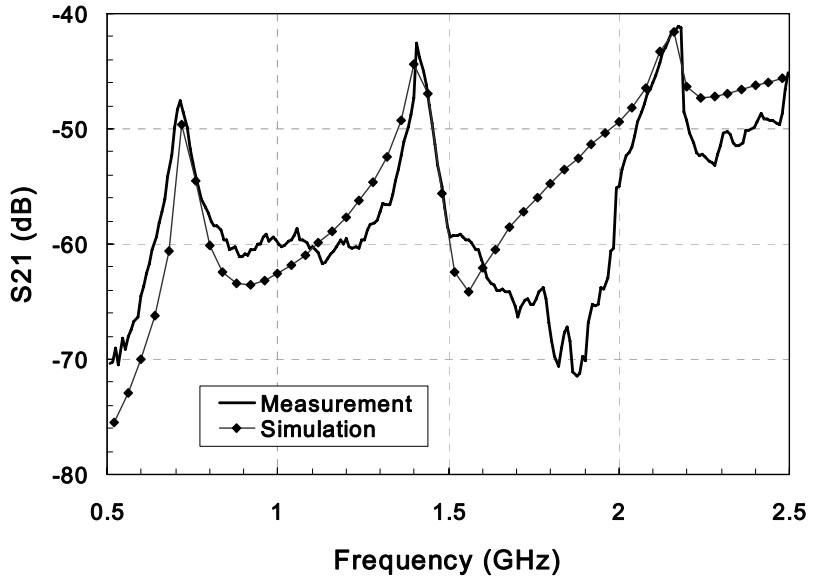

Figure 3.7: Measured and simulated S_{21} of the ring resonator configuration A.

The relative permittivity ε_r can be extracted from the effective relative permittivity ε_{eff} and the dimensions of the microstrip [51] using Equation 3.1.

$$\varepsilon_r = \frac{2 \times \varepsilon_{eff} + M - 1}{M + 1} \tag{3.1}$$

where ε_{eff} is a function of the ring radius r_m, the nth resonant frequency f_0 obtained from measurement of the insertion loss, and the speed of light in vacuum c [51], as defined in Equation 3.2,

$$\varepsilon_{eff} = \left(\frac{n \times c}{2 \times \pi \times r_m \times f_0} \right)^2 \tag{3.2}$$

and M in Equation 3.1 is a function of the thickness of the paper h and of the fringing effects on the microstrip edges, which can be calculated as a function of h and conductor thickness t [52], as shown in Equation 3.3.

$$M = \left(1 + \frac{12 \times h}{w_{eff}} \right)^{-0.5} \tag{3.3}$$

w_{eff} in Equation 3.3 is the effective strip width accounting for the non-zero strip thickness and is given by Equation 3.4.

$$w_{eff} = w + \frac{1.25 \times t}{\pi} \left(1 + \ln\left(\frac{2h}{t} \right) \right) \tag{3.4}$$

The values of the relative permittivity extracted at the three resonating modes' frequencies for each ring resonator are shown in Figure 3.8. The lowest value obtained was 3.2 and the highest was 3.5 in the range of 0.5-2.5 GHz, with a slight decrease with increasing frequency. The same behavior has been observed in other material characterization measurements conducted in low frequencies [16]. Lower ε_r is expected at a higher frequency band, as will be verified by the cavity resonator measurements in the next section. The uncertainty in ε_r includes errors due to the ring resonator dimensions, sample thickness and resonant frequency. Linear regression analysis was applied to estimate the confidence interval of ε_r results under the rule of least squares. A 95% two-

sided confidence interval is ±2.776 s{ε_r}, in which s{ε_r} is the unbiased estimator of variance σ{ε_r} [53]. The corresponding error bar was plotted in Figure 3.8.

The loss in the rings occurs mainly due to the conductors, lossy dielectrics and radiation. The loss tangent of the paper substrate is a function of only the attenuation due to the dielectric a_d at the resonant frequency [52] and is computed using Equation 3.5.

$$tan\delta = \frac{\alpha_d \times \lambda_0 \times \sqrt{\varepsilon_{eff}}\left(\varepsilon_r - 1\right)}{8.686 \times \pi \times \varepsilon_r \left(\varepsilon_{eff} - 1\right)} \tag{3.5}$$

where λ_0 is the wavelength of the free-space radiation from the rings at the resonant frequencies. a_d was extracted by subtracting the attenuation resulting from the conductor a_c and radiation a_r from the total attenuation a_{total} that occurs in the structure at the resonant frequencies.

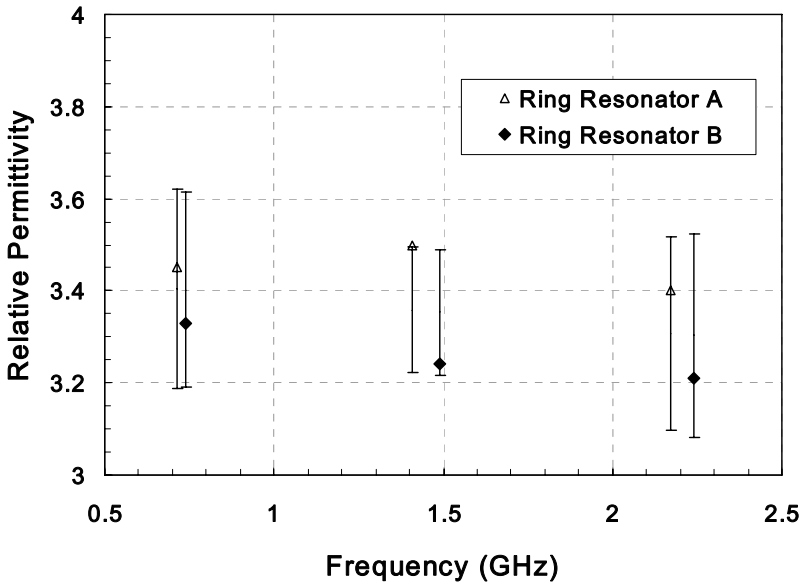

Figure 3.8: Extracted relative permittivity of paper at the resonant frequencies listed in Table 3.2.

The ring attenuation due to radiation was computed using [54][55][56] and was found to be negligible, and therefore ignored in the computation of the attenuation due to the dielectric. The attenuation in the rings due to conductor losses was computed using formulas given in [52][57][58]. However, the result given by the formula in [52] was chosen since it included the effect of surface roughness, which is shown in Equation 3.6,

$$\alpha_c = \frac{R_{ss}}{Z_0 * h} \times \frac{8.686}{\left(\frac{w_{eff}}{h} + \frac{2}{\pi} \ln\left(2\pi \times e\left(\frac{w_{eff}}{2h} + 0.94 \right) \right) \right)^2} \times \left(\frac{w_{eff}}{h} + \frac{\frac{w_{eff}}{\pi h}}{\frac{w_{eff}}{2h} + 0.94} \right) \times \times \left(1 + \frac{h}{w_{eff}} + \frac{h}{\pi \times w_{eff}} \left(\ln\left(\frac{2h}{t} + 1 \right) - \frac{\left(1 - \frac{t}{h} \right)}{\left(1 + \frac{t}{2h} \right)} \right) \right) \tag{3.6}$$

where R_{ss} is the AC resistance of the copper conductor in the rings in ohms that includes the effects of surface roughness Δ and skin depth ζ, as given by Equation 3.7.

$$R_{ss} = \sqrt{\frac{\pi \mu_0 f_0}{\sigma_{Cu}}} \times \left(1 + \frac{2}{\pi} \tan^{-1}\left(1.4 \times \left(\frac{\Delta}{\varsigma} \right)^2 \right) \right) \tag{3.7}$$

The total attenuation in the resonator is obtained from its unloaded quality factor (Q_0), as given in Equation 3.8.

$$\alpha_{total} = \frac{\pi}{Q_0 \lambda_{eff}} \tag{3.8}$$

where the effective wavelength of the TEM signal in the ring resonator λ_{eff}, calculated as a function of the free-space wavelength, λ_0, using Equation 3.9.

$$\lambda_{eff} = \frac{\lambda_0}{\sqrt{\varepsilon_{eff}}} \tag{3.9}$$

The unloaded quality factor Q_0 in Equation 3.8 is obtained from the insertion loss (LA) and the -3 dB bandwidth measured at the resonant frequency (f_0) using Equation 3.10.

$$Q_0 = \frac{f_0}{BW_{-3dB} \times \left(1 - 10^{-L_A/20}\right)} \tag{3.10}$$

The loss tangent extracted from ring B at three different resonating frequencies is shown in Figure 3.9. It shows values between $6x10^{-2}$ and $8x10^{-2}$. With the aim of verifying the loss tangent by other methods, a simulation-based transmission line (TL) method was utilized. A microstrip line with length 74.8 mm and width 2.53 mm was fabricated on the same paper material. Simulation results for conductor and radiation losses, a_c and a_r, respectively, of the microstrip lines were subtracted from the total loss a_{tot}. This was done by simulating a microstrip line with no dielectric loss in HFSS and extracting a_c and a_r, then subtracting these effects from the total measured loss. The TL method results are also plotted in Figure 3.9, showing good agreement with the microstrip ring resonator method.

Regression analysis from the *tanδ* data set revealed that linear regression was not a good estimation in calculating the uncertainty in *tanδ.* Since the uncertainty of the measured quality factor Q_0 is the major error source [59], if other uncertainties are neglected, such as resonant frequency, the uncertainty in *tanδ* can be calculated from the uncertainty in the measured Q_0. For these sets of measurements, a 10% uncertainty in measured Q_0 was assumed [60]. The calculated uncertainty in *tanδ* is shown in the error bar in Figure 3.9.

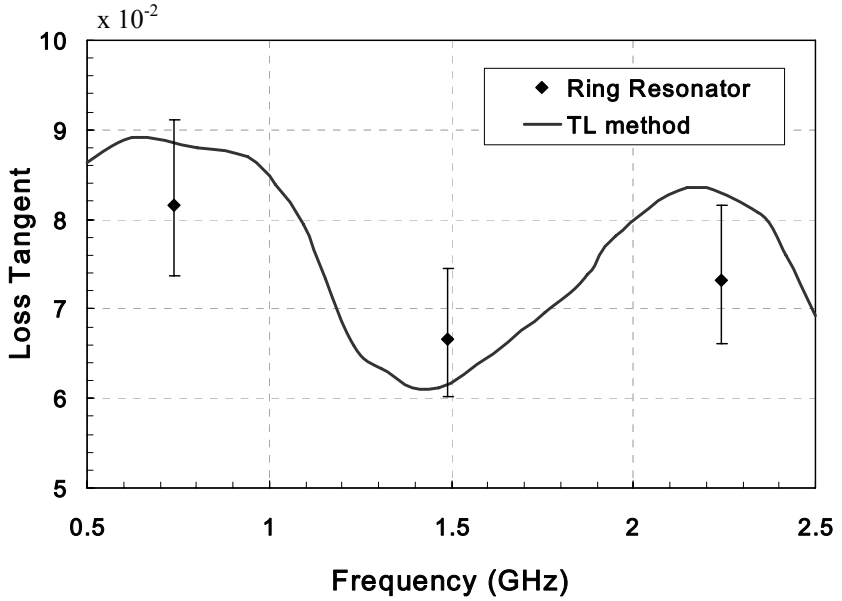

Figure 3.9: Paper loss tangent versus frequency measured with the microstrip ring resonator method and TL method. Error bar shows the variance with 10% uncertainty in measured quality factor Q_0.

The average values of the measured relative permittivity (3.2) and the loss tangent ($7.7x10^{-2}$) were adopted in the full-wave HFSS simulation. Good agreement in terms of resonant peak positions between measured and simulated results is shown in Figure 3.7.

Notice that when frequency range extends to 30 GHz, the roughness of the metal surface potentially approaches the skin depth, resulting in an inaccurate loss tangent extraction, which usually requires acceptable theoretical equations for microstrip conductor losses [61]. In this case, the cavity resonator method provides a higher level of accuracy compared with the other methods and does not require a pretreatment on the substrate [43].

3.4 RFID Tag on Paper Substrate using Inkjet-Printing Technology

The realization of paper substrate RF dielectric characterization in the preliminary research paves the way for a system-level solution for ultra-low-cost production in UHF,

wireless and microwave applications. For example, the major challenges existing in today's RFID technologies advancing toward the practical large-scale implementation stage is to lower the cost of the RFID tags and reduce the design and fabrication cycle. Most cost models indicate that individual tags must cost less than 1 cent to be economically viable for practical applications [11]. The effective characterization of paper in substrate a wireless/RF frequency band provides the possibility of dramatically reducing the cost of RFID tags.

To achieve this design goal, a T-match folded bowtie half-wavelength dipole antenna [62] was designed and fabricated on the characterized paper substrate by inkjet-printing. This design was used for matching the passive antenna terminals to the TI RI-UHF-Strap-08 IC with resistance R_{IC} = 380Ω and reactance modeled by a capacitor with value C_{IC} = 2.8pF [63]. The RFID prototype structure is shown in Figure 3.10 along with dimensions, with the IC placed in the center of the T-match arms. The T-match arms are also responsible for matching the impedance of the antenna terminals to that of the IC through the fine tuning of the length L_3, height h, and width W_3.

The design was inkjet-printed with a Dimatix Materials Printer DMP-2800. In measurement, a GS 1000 μm pitch probe connected to a UHF balun to ensure the balanced signal between the arms of the T-match folded dipole antenna was used for impedance measurements. To minimize backside reflections of this type of antenna, the inkjet-printed antennas were placed on a custom-made probe station using high-density polystyrene foam with a low relative permittivity of value 1.06 resembling that of the free space [64]. The calibration method used was short-open-load-thru (SOLT). The measurement setup is shown in Figure 3.11.

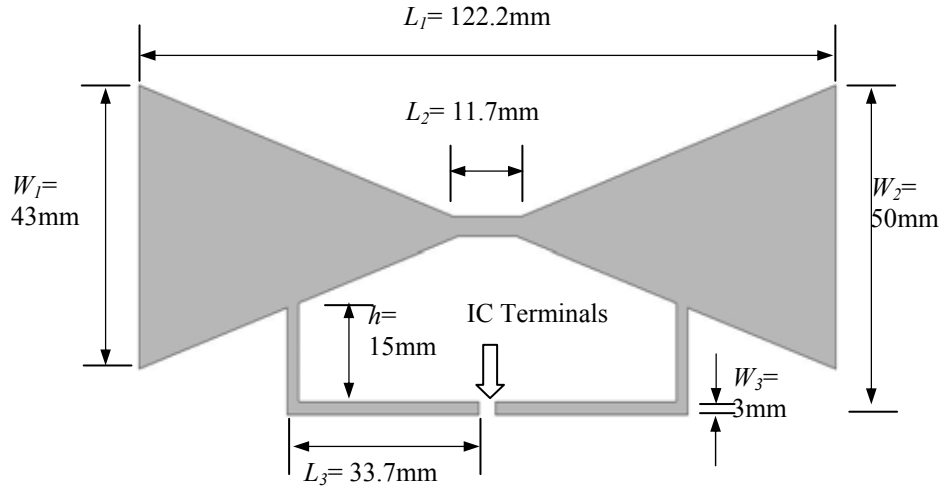

Figure 3.10: T-match folded bowtie RFID tag module configuration. The dimensions were optimized based on the paper substrate characterization results.

Figure 3.11: Photograph of the impedance measurement using GS pitch probe.

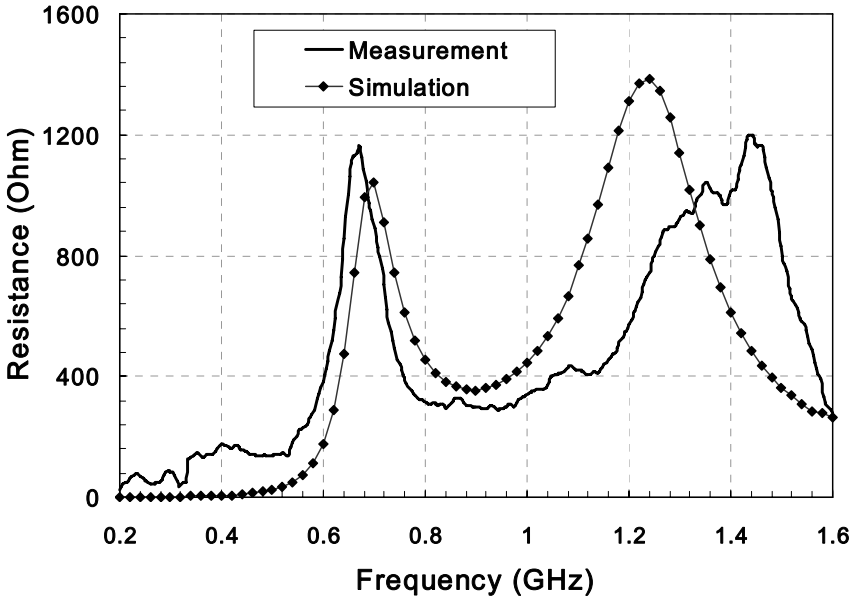

(a)

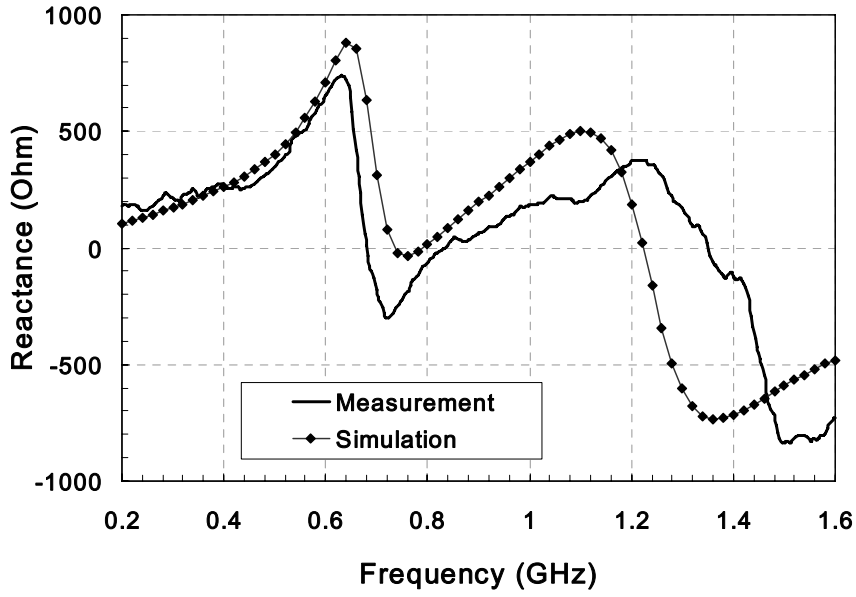

(b)

Figure 3.12: Measured and simulated input resistance and reactance of the inkjet-printed RFID tag, (a) Resistance (b) Reactance.

Figure 3.12 shows the impedance plots. As shown in Figure 3.12(a), the simulated resistance for the antenna in the UHF RFID frequency range maintains a value close to 380 Ohms between the two successive peaks. The reactance part of the impedance, as shown in Figure 3.12(b), features a positive value with a linear variation with frequency, pertaining to an inductance value that conjugately matches or equivalently cancels the effect of the 2.8 pF capacitance of the IC. Fairly good agreement was found between the simulation and measurement results. The distortion is possibly due to the effect of the metal probe fixture, which affects the measured radiating near field.

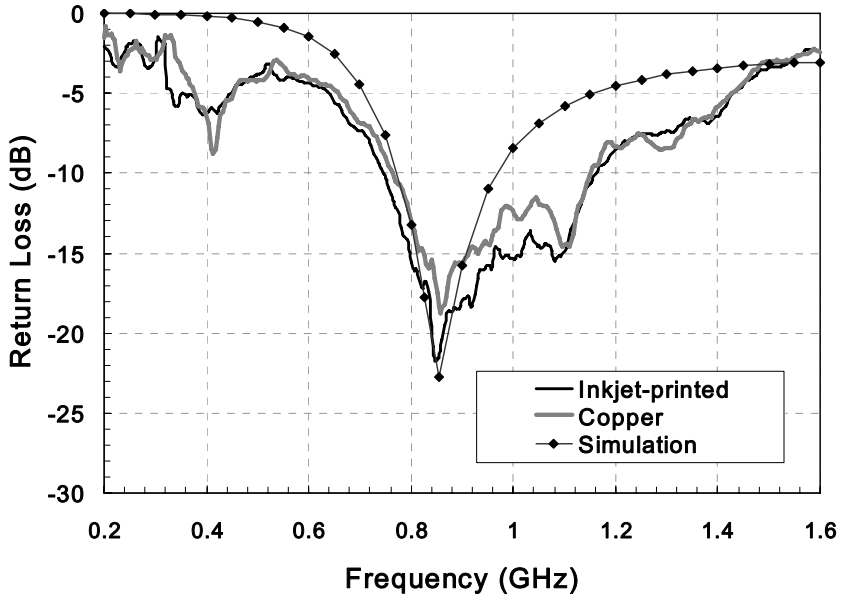

Figure 3.13: Return loss of the RFID tag antenna which covers the universal UHF RFID band.

The return loss of this antenna was calculated based on the power reflection coefficient which takes into account the reactance part of the IC's impedance [23]. The return loss plot is shown in Figure 3.13, demonstrating good agreement for both paper

metallization approaches. The nature of the bowtie shape of the half-wavelength dipole antenna body allows for a broadband operation, with a designed bandwidth of 190MHz corresponding to 22% around the center frequency 854 MHz, which covers the universal UHF RFID bands. It has to be noted that the impedance value of the IC stated above was provided only for the UHF RFID frequency which extends from 850 MHz to 960 MHz; thus, the return loss outside this frequency region, shown in Figure 3.13, may vary significantly due to potential IC impedance variations with frequency.

To verify the performance of the ink-jet printed RFID antenna, measurements were performed on a copper-metallized antenna prototype with the same dimensions fabricated on the same paper substrate using the slow etching technique mentioned before. The return loss results in Figure 3.13 show that the return loss of the inkjet-printed antenna is very slightly larger than the copper one. Overall, good agreement between the copper etched and the inkjet-printed antennas was observed despite the higher metal loss of the silver-based conductive ink.

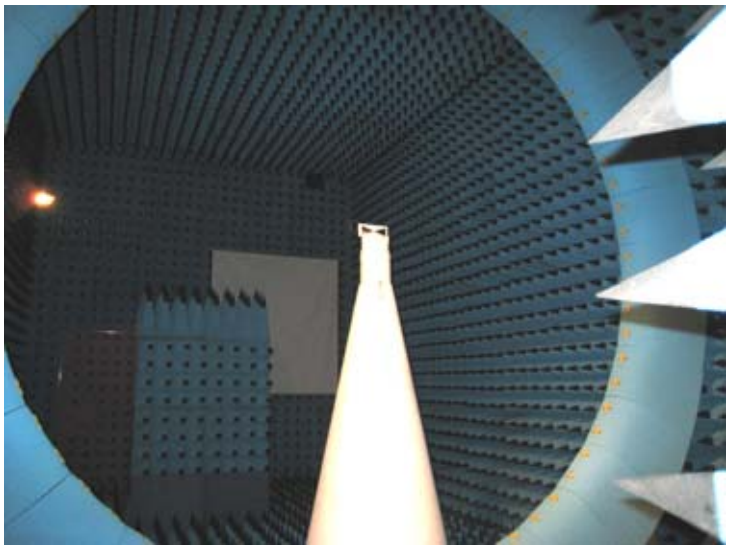

Figure 3.14. Photograph of the radiation pattern measurement in a microwave chamber.

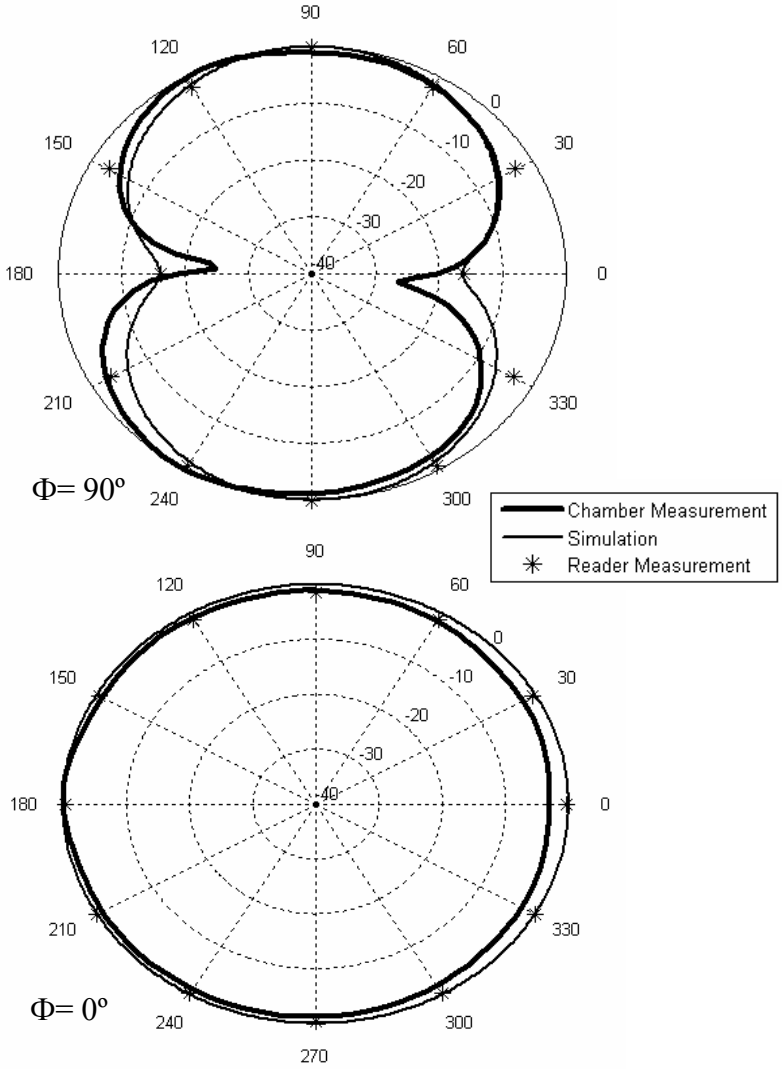

Figure 3.15: Normalized 2D far-field radiation pattern plots of simulation, chamber measurement and tag reading distance measurement. An omnidirectional radiation pattern can be observed at Φ= 0º plane with directivity around 2.1 dBi.

The radiation pattern of the inkjet-printed antenna was measured in a microwave chamber, as shown in Figure 3.14. The radiation pattern is almost uniform (omnidirectional) at 915 MHz with directivity around 2.1 dBi. The IC strap was attached to the IC terminal with H2OE Epo-Tek silver conductive epoxy cured at 80 ^{o}C. An UHF RFID reader was used to detect the reading distance at different directions to the tag. These measured distances are theoretically proportional to the actual radiation pattern.

The normalized radiation patterns of simulation, microwave chamber measurement and reader measurement are plotted in Figure 3.15, showing very good agreement between simulations and measurements, which can also be verified for other frequencies within the antenna bandwidth.

3.5 Inkjet-printed RFID Tags with Ink-usage Optimization

After introducing the paper-based substrate into the low-cost RFID tag design methodology, conductive ink has become the major cost factor of an RFID tag instead. Further reduction of the cost requires the optimization work on the ink's side. Minimizing the amount of ink used per antenna will save thousands of dollars in the mass production. The methods of minimizing the ink usage by reducing solid printed surfaces with alternative designs, while maintaining the tag antenna performance will be examined on a benchmark antenna without loss of generality. Then the ink-usage reduction method will be applied on a commercial RFID tag to test the performance.

The benchmark "solid" bowtie dipole antenna working at European UHF RFID band is shown in Figure 3.16. Figure 3.17 shows the step by step process performed to gradually reduce the amount of conductive ink utilized, with the current distribution and return loss performances.

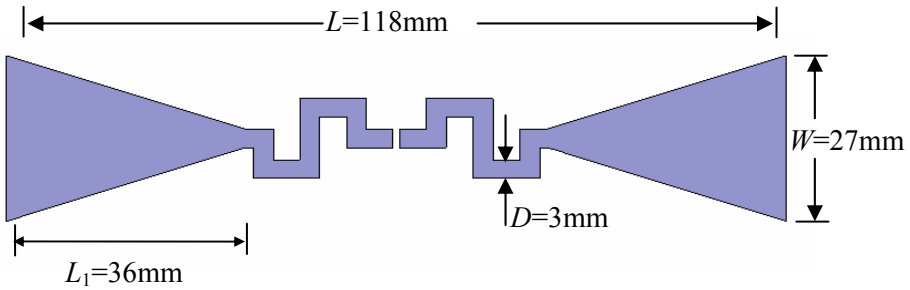

Figure 3.16: The benchmark bowtie dipole antenna configuration.

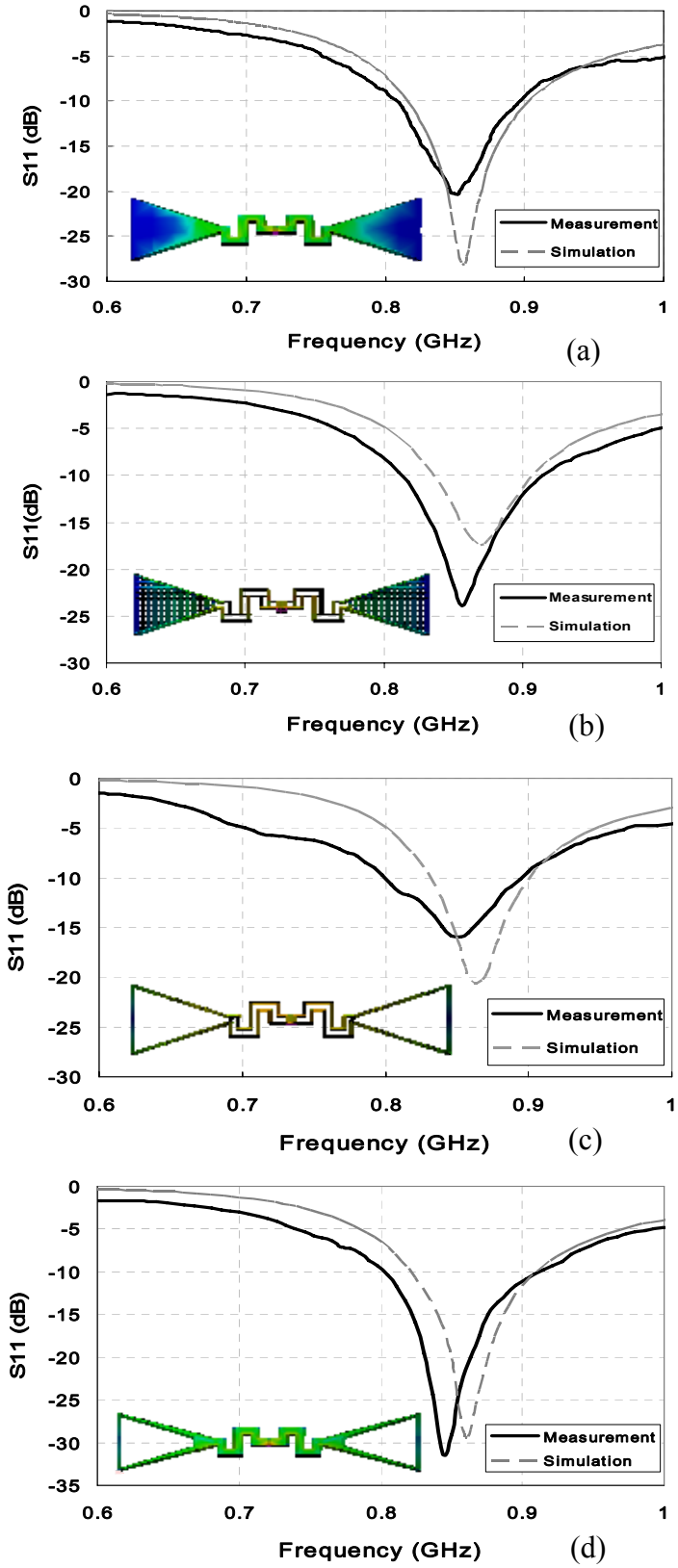

Figure 3.17: Current distribution and return loss comparison of four inkjet-printed antenna designs at European RFID band.

A straight forward solution of reducing the amount of the ink used is to replace the original structure with a grid pattern. Figure 3.17(b) shows an alternative design with thin wire grid of width 0.3 mm. A slightly degraded but acceptable performance is maintained, as depicted in Table 3.3. When the grid lines became sparser, like the one depicted in Figure 3.17(c), the ink saved is about 94% compared with the original one, however, the radiation efficiency decreased below 90% and the BW started to shrink. The major reason is that grid lines disrupt the current flow path and distort the current distribution. One can clearly observe from the current distribution simulation in the Figure 3.17(a) that the highest concentration is mainly occurring closest to the center of the radiating body. Based on this phenomenon, an alternative design was realized, as shown in Figure 3.17(d). Solid areas are only cleared in the region where current distribution is the weakest. In this way, most of the area in the central feeding strips is remained and large area of the bowtie arms is removed. As shown in the current distribution plot, the surface current almost remained undistorted in this topology. Radiation efficiency of 99% was maintained, and a better impedance matching was even achieved, resulted in a 0.2% wider BW.

Table 3.3: Simulated performance comparison for the antennas shown in Figure 3.17

	BW (%)	EFF. (%)	Gain (dBi)
(a)	10.1	99	1.94
(b)	8.66	91	1.66
(c)	7.9	89	1.61
(d)	10.3	99	2.03

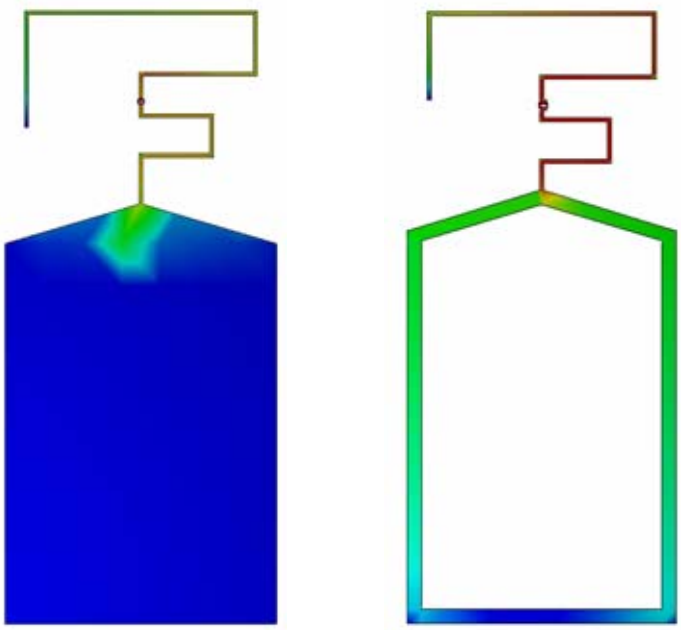

(a) (b)

Figure 3.18: Current distribution comparison of a commercial RFID tag antenna and the proposed modified design with ink-usage optimization.

Table 3.4: Simulated performance comparison for the antennas shown in Figure 3.18

	BW (%)	EFF. (%)	Gain (dBi)
(a)	5.4	90.6	1.48
(b)	5.2	90.4	1.49

The same design topology can be used to lower the cost of existing commercial RFID tags. To verify the effectiveness of using current distribution plot to help reducing the inkjet-printing area, an ink-usage-optimization RFID tag based on an Intermec Windshield Sticker tag [65] was fabricated for performance comparison. The commercial tag has been widely used on toll road collection applications. However, the monopole ground costs a large area for the conductive ink. The current distribution and the

modified schematic layout are depicted in Figure 3.18, showing only the edge of the monopole ground is remained in the modified design. The meanderline dimensions of the monopole arm were also modified to ensure a good matching to the IC chip impedance, because paper substrate was used instead of polyethylene terephthalate (PET) for this low-cost tag design which changed the antenna input impedance. The amount of the conductive ink used is around 12% of the original design. Table 3.4 shows the antenna performance comparison between these two tags.

Photograph of the fabricated is shown in Figure 3.19. The key values of the ink-usage-optimization RFID tag are summarized in Table 3.5. The tag was attached on a glass surface with 0.5mm paper substrate spacer. The measured maximum reading range is 4.0 m with a circularly polarized reader antenna. The comparison of the measured reading distances is summarized in Table 3.6. The higher range of the modified tag is possibly due to the better impedance matching achieved during the design of the monopole arm. Overall, 88% of the conductive ink was saved while a competing performance was achieved.

Figure 3.19: Photograph of the proposed inkjet-printed RFID tag on paper-based substrate with ink-usage optimization.

Table 3.5: Ink-usage-optimization RFID tag key parameters

EIRP	Gain (G)	Antenna (Z_{ant})	Chip (Z_{IC})	τ	P_{th}
4 W	1.49 dBi	43.7+j123 Ω	33-j112 Ω	0.96	-9 dBm

Table 3.6: Comparison of the read range of the windshield tags

	Ink-usage-optimization Tag	Commercial Windshield Tag
Ink Usage	12%	100%
Read Distance	4.0 m	3.9 m

* 4W EIRP, circularly polarized reader antenna

3.6 Chapter Summary

In this chapter, the dielectric characteristics of paper have been investigated in the UHF range and have been utilized to design and fabricate RF passive structures using an inkjet-printing process. A compact RFID tag module, with T-match folded bowtie structure to match the antenna to the IC, was printed on the characterized paper substrate and tested, featuring a very good overall performance. The ink-usage-optimization techniques have also been demonstrated to further reduce the price of RFID tag fabrication on the material cost aspect. This research effort verifies that paper-based inkjet-printing topologies offer a very low-cost, eco-friendly solution to system-level packaging for UHF, wireless and microwave applications.

CHAPTER 4

CONFORMAL MAGNETIC COMPOSITE RFID

This chapter introduces a novel flexible magnetic composite material for RFID antennas. First, one conformal RFID tag working at 480MHz is designed and fabricated as a benchmarking prototype and the miniaturization concept is verified. Then, the impact of the material is thoroughly investigated using a hybrid method involving electromagnetic and statistical tools. Two separate statistical experiments are performed, one for the analysis of the impact of the relative permittivity and permeability of the proposed material and the other for the evaluation of the impact of the dielectric and magnetic loss on the antenna performance. Finally, the effect of the bending of the antenna is investigated, both on the S-parameters and on the radiation pattern. The successful implementation of the flexible magnetic composite material enables the significant miniaturization of RF passives and antennas in UHF frequency bands, especially when conformal modules that can be easily fine-tuned are required in critical biomedical and pharmaceutical applications.

4.1 Motivation

The demand for flexible miniaturized RFID tags has rapidly increased due to the requirements of automatic identification in various areas, such as item-level tracking and patient life-signs monitoring [66][67]. The technology for RFID systems continuously improves and extends to structures of non-planar shapes and to conformal sensors for WBAN [68]. Also, there is an increased demand for miniaturization, potentially addressed by the choice of substrate material, particularly magnetic materials [69]. The magnetic materials allow the miniaturization of the circuits without the use of a very large dielectric constant substrate. Three-dimensional transponder antennas that utilize

wound coil inductors do make use of magnetic cores, but they are quite bulky and impractical. On the other side, flexible magnetic materials for two-dimensional embedded conformal planar antennas have not yet been successfully realized for standard use. This chapter introduces for the first time a novel, mechanically flexible magnetic composite for printed circuits and two-dimensional antennas, which can reap the same miniaturization and tuning benefits as the non-flexible magnetic cores used for three-dimensional antennas.

One of the most significant challenges for applying new magnetic materials is understanding the interrelationships of the properties of the new materials with the design and performance of the specific topology (e.g., radiation pattern, scattering parameters). In previous studies, it has often been cited that the objectives of miniaturization and improved performance are tempered by the limited availability of materials that possess the required magnetic properties, while maintaining an acceptable mechanical and conformality performance [70]. Recently, the formulation of nano-size ferrite particles has been reported [71] and the formulation of magnetic composites comprising ferrite filler and organic matrix has been demonstrated [72]. The implication of new magnetic materials has not yet been investigated for specific electromagnetic (EM) systems above the low MHz range. Additionally, in the case of complex microwave systems involving numerous interconnects, dielectric interfaces, or radiating structures, the simultaneous optimization of the structure geometry along with the material may be necessary to achieve the optimal targeted performance. The aim of this work is to provide a basis for this co-design of materials and electromagnetic structures, namely, for the benchmarking case of a novel flexible magnetic composite, a BaCo ferrite-silicone composite, and a UHF RFID antenna, respectively. Compared with the lower frequency tags operating in the LF and HF bands that suffer from limited read range, RFID tags operating in the UHF band are forecast to find the widest use due to their higher read range and higher data transfer rate in a more miniaturized size [73]. The UHF RFID bands vary in frequency,

power levels, number of channel and sideband spurious limits of the RFID readers signal, depending on the application and the area of operation, such as 866-956 MHz in North America/Europe for EPC GEN2 item-level tracking and the lower band around 400MHz for bio-applications.

Specifically, in this study, a benchmark structure was first designed for 480 MHz in a full-wave simulator for an unfilled silicone substrate; then the magnetic particles, namely the Co2Z powder from Trans-Tech, were added and the same antenna was redesigned for 480 MHz by reducing its physical size, thus proving the miniaturization concept. It is well known that the size of the antenna is inversely proportional to the square root of the product of effective permittivity and effective permeability. Therefore, a non-magnetic material would have to have a permittivity close to about 18 to give comparable miniaturization capability, which is high compared to the permittivity of 7.14 for the magnetic material used in this work. The next step was the fabrication of the material and the measurement of the dielectric and magnetic characteristics, including loss. The benchmarking miniaturized antenna was fabricated on the magnetic composite and its performance was measured validating the simulations with the measured data [74]. Furthermore, the impact of the material on the system-level performance of the antenna was thoroughly investigated using a hybrid method including electromagnetic simulators and statistical tools: first, the very important issue of dielectric and magnetic losses, then both the relative permittivity and permeability. Finally, the performance of the antenna when conformed on a foam cylinder was measured, both the S-parameters and radiation pattern, and it was concluded that the antenna is still functional even for a tight bending radius of 27mm. Magnetic materials can provide RF designers with increased options in their system design, especially if their effects are better understood. This detailed analysis of the system-level impact of the electrical parameters of the magnetic composite attempts to bring more understanding and to enable a more extensive future use of such materials. The presented magnetic substrate is the first flexible magnetic composite tested

and proven for the 480 MHz bandwidth with acceptable magnetic losses, which makes it usable for lightweight conformal/wearable applications like pharmaceutical industry and wireless health monitoring in hospital, ambulance and home-based patient care, as well as wearable communication and authentication devices.

4.2 Material Development

The first step for this work was to develop a magnetic composite that provides the advantage of low-temperature processing for compatibility with organic substrate processing, mechanical flexibility, and high adhesion. With regard to these three properties, the magnetic composite would have to be compatible with common substrates used for RFID, such as PET and polyimide. Additionally, the composite dielectric loss can affect circuit performance, thus low dielectric loss should be targeted. For these objectives, the properties of candidate materials should include low-temperature processability, high mechanical flexibility, high adhesion, and low dielectric loss. Dielectric constant can also affect the circuit performance and should be carefully monitored. The matrix materials considered candidates for this proposed work included silicone and benzocyclobutene (BCB). Silicone provides reasonable viscosities required for good filler mixing during processing, that is, not too low to promote settling and not too high for uniform mixing. Additionally, silicone provides the properties of mechanical flexibility and, for some formulations, good adhesion.

After careful analysis, the matrix material was chosen to be Dow Corning Sylgard 184 silicone. The dielectric parameters of the unfilled silicone, used in the initial antenna design, are ε_r= 2.65 and $tan\delta_\varepsilon$= 0.001. The choice for the magnetic composite was Co_2Z powder supplied by Trans-Tech. A 40 vol% ferrite paste was produced with a mixer at 240 rpm (rotations per minute) and 110°C for 30 minutes. The paste was transferred into a flat mold and vacuum cured with a hold confirmed to occur at >125°C for 50 minutes to produce a 1.3 mm thick substrate.

The material was measured using an HP4291A impedance analyzer to obtain complex permittivity (ε) and permeability (μ) (real and imaginary parts) with material fixtures 16453A for ε and 16454A for μ over the frequency range of 1MHz to 1.8GHz. There were 5 measurements taken for each ε_r, μ_r, $tan\delta_e$ and $tan\delta_m$. The summary statistics, including the mean and 95% confidence intervals (CI) for ε_r, μ_r, $tan\delta_e$ and $tan\delta_m$ of the ferrite composite at 480 MHz are given in Table 4.1. Based on these results, the values used in the model were $\varepsilon_r = 7.14$, $\mu_r = 2.46$, $tan\delta_e = 0.0017$ and $tan\delta_m = 0.039$.

Table 4.1: Mean and 95% confidence intervals for ε and μ measurements of ferrite composite at 480 MHz

	mean	*Lower CI*	*Upper CI*
ε_r	7.142	7.083	7.201
μ_r	2.463	2.457	2.468
$tan\delta_\varepsilon$	0.0017	0.0005	0.0028
$tan\delta_\mu$	0.0391	0.0358	0.0424

4.3 Antenna Design and Measurement

One of the main challenges in designing an RFID tag is the impedance matching between the terminals of the tag antenna and those of the IC. This requires a conjugate matching technique, such as series or parallel stubs and/or using inductively coupling. The matching network of the tag has to guarantee the maximum power delivered to the IC, which is used to store the data transmitted to and receive from the RFID reader. The return loss of RFID antenna can be calculated based on the power reflection coefficient which takes into account the reactance part of the IC impedance [75]:

$$|S|^2 = \left| \frac{Z_{IC} - Z_{ANT}^*}{Z_{IC} + Z_{ANT}} \right|^2 \tag{4.1}$$

where Z_{IC} represents the impedance of the IC and Z_{ANT} represents the impedance of the antenna terminals with Z_{ANT}* being its complex conjugate.

Another challenge is the dimensions of the RFID tag. The free space wavelength at 480MHz is 625 mm. For an application as wristband patient monitoring, it is clear that the miniaturization of the tag becomes a priority.

To verify the miniaturization benefits of the presented magnetic composite, a folded bowtie meander line dipole antenna was designed and fabricated on the characterized magnetic composite material substrate. The RFID prototype structure is shown in Figure 4.1 along with dimensions, with the IC placed in the center of the shorting stub arm.

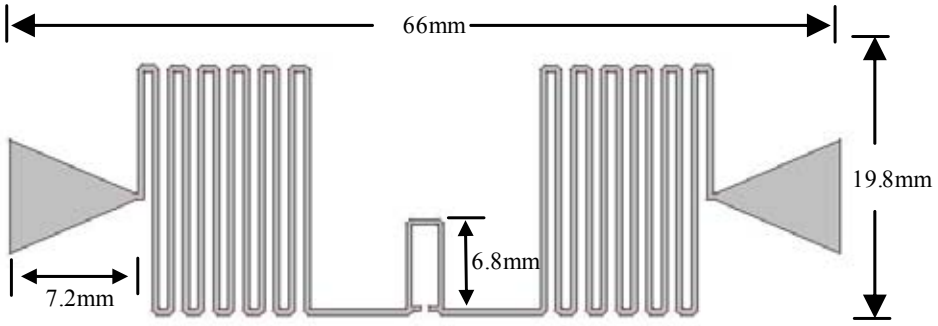

Figure 4.1: Configuration of the RFID tag module on magnetic composite substrate.

The nature of the bowtie shape of the half-wavelength dipole antenna body allows for a more broadband operation [76]. The meander line helps further miniaturizing the antenna structure [77]. The shorting stub arm is responsible for the matching of the impedance of the antenna terminals to that of the IC through the fine tuning of the length.

Next, a GS 1000μm pitch probe was used for impedance measurements. In order to minimize backside reflections, the fabricated antenna was placed on a custom-made probe station using high density polystyrene foam with low relative permittivity of value 1.06, resembling that of the free space. The calibration method used was short-open-load-thru (SOLT). The initial structure was designed for the lower end of the UHF spectrum and was modeled using Zeland IE3D full wave EM software. The initial substrate was pure silicone (ε_r= 2.65 and $tan\delta_\varepsilon$= 0.001) of 1.3mm thickness. The same dimensions of the antenna were maintained for the magnetic composite material. The Return Loss plot is shown in Figure 4.2, demonstrating a frequency down shifting of 20% due to the enhanced combined relative permeability and relative permittivity, which proves the miniaturization concept. Figure 4.2 shows very good agreement for the simulations vs. measurements for the antenna on the magnetic composite.

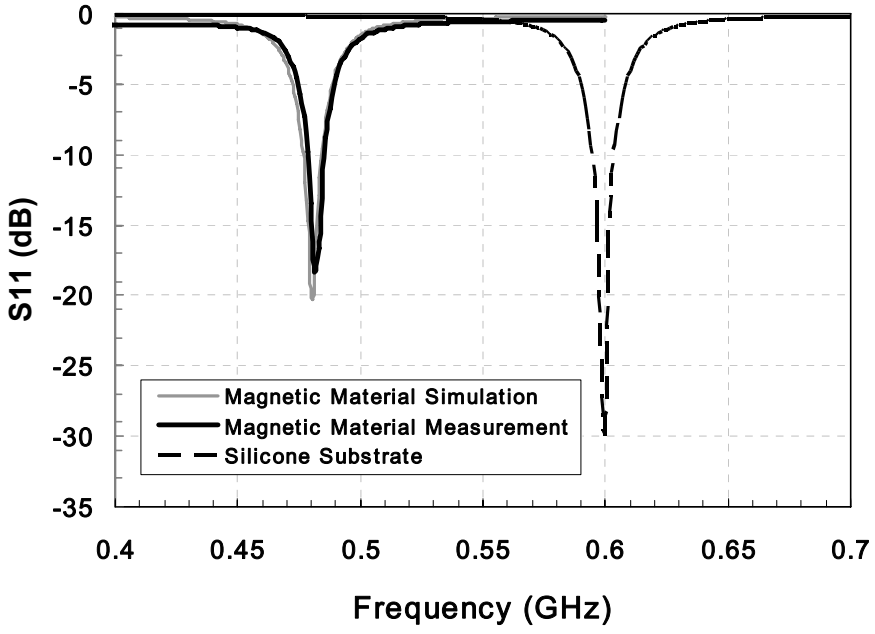

Figure 4.2: Measured and simulated return loss of the RFID tag antenna on the magnetic material with the comparison of the one on the silicone substrate.

The radiation pattern comparison of simulation vs. measurements of the RFID tag module on magnetic substrate is shown in Figure 4.3, showing good agreement. The radiation pattern is almost uniform (omnidirectional) at 480 MHz with a gain around -4.63dBi.

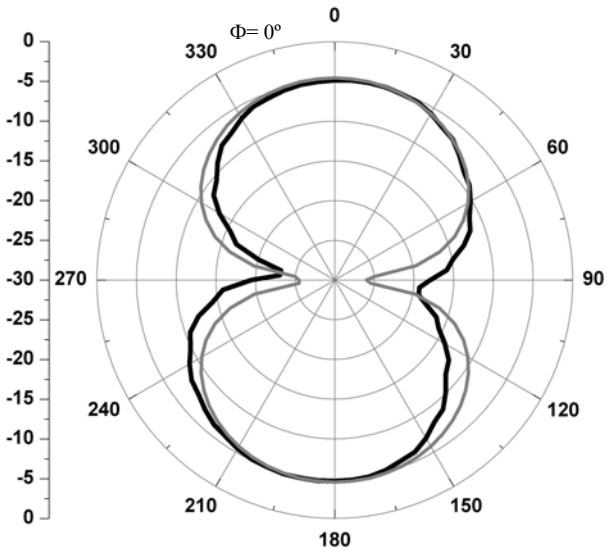

(a)

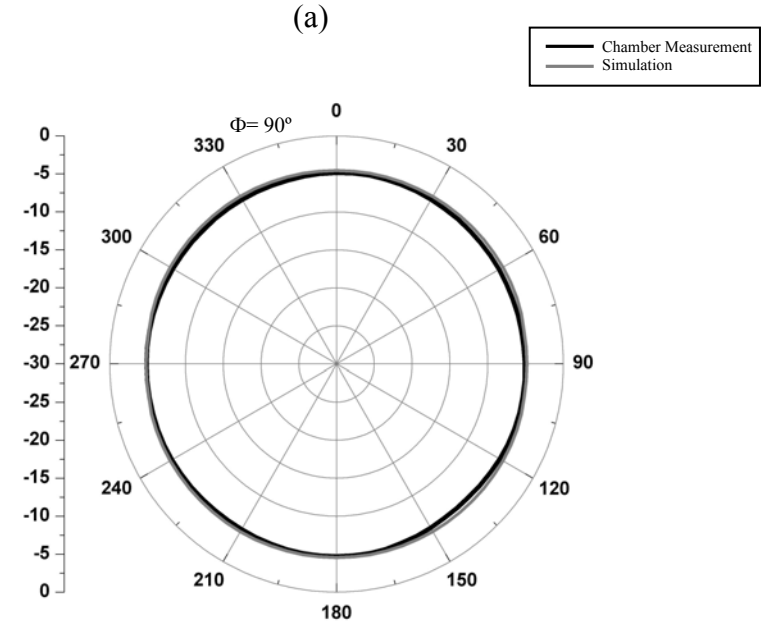

(b)

Figure 4.3: Simulated vs. measured 2D radiation plots for (a) $\phi = 0^o$ and (b) $\phi = 90^o$.

4.4 Magnetic Composite Impact on Antenna Performance

One of the most critical factors in the magnetic composite fabrication was the control of the permittivity and permeability values, so a careful analysis of the impact of both the dielectric and magnetic performance based on the fabrication variability was necessary. These material properties are not mutually exclusive. The permittivity [78] and permeability [79] are both governed by the molecular arrangement (lattice structure) and elemental composition of the material, which prevents the tuning of these properties independently. So the following analysis does not attempt to optimize the material parameters, but rather to quantify the effect of the parameters on the system-level performance of the antenna.

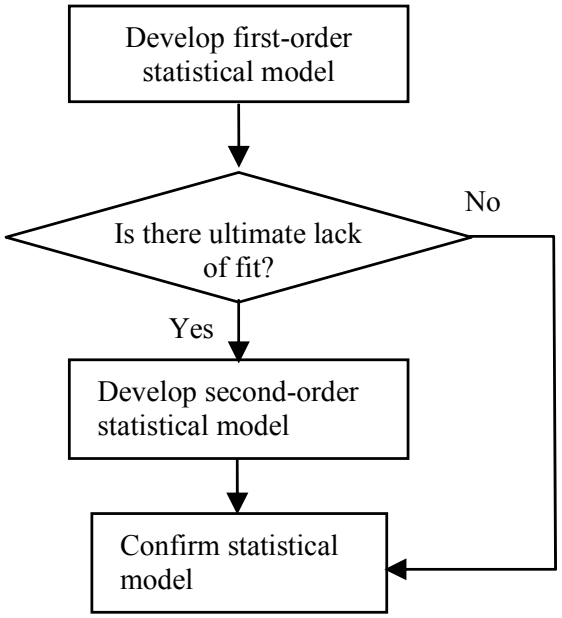

Figure 4.4: Procedure for statistical model development.

First, the impact of the loss tangents was investigated. The methodology used involves electromagnetic simulations and statistical tools and is presented as a flowchart in Figure 4.4. First, Design of Experiments (DOE) [80] is performed to develop the first

order (linear) statistical model, including both loss tangents, dielectric and magnetic. Then, the model is checked for ultimate lack of fit, more specifically, if curvature might be present in the output response. If curvature in the response is detected, the analysis is extended to additional points indicated by the Response Surface Methodology (RSM) [80] which can account for curvature through second-order model development. Usually, these second-order models are reasonable approximations of the true functional relationship over relatively small regions. Once validated using statistical diagnostic tools, the models approximate the actual system within the defined design space. Hybrid methods including statistical tools and EM simulations have been extensively used for RF and microwave systems analysis and optimization [81].

The statistical experimentation method chosen for the first-order statistical model is a full factorial DOE with center points. The factorial designs are used in statistical experiments involving several (k) factors where the goal is the study of the joint effects of the factors on a response and the elimination of the least important ones from further optimization iterations. The 2^k factorial design is the simplest one, with k factors at 2 levels each. It provides the smallest number of runs for studying k factors and is widely used in factor screening experiments [80]. Center points are defined at the center of the design space and enable investigating validity of the model, including curvature in the response, and account for variations in the fabrication process of the structure. Since the statistical models are based on deterministic simulations, the variations of the center points were statistically simulated assuming a 3σ process with a $\pm 2\%$ tolerance for both $tan\delta_\varepsilon$ and $tan\delta_\mu$.

Table 4.2 Ranges for the input variables

Variable	Low value "-"	High value "+"	Center point
$tan\delta_\varepsilon$	0.00136	0.00204	0.0017
$tan\delta_\mu$	0.0312	0.0468	0.039

In this case, since we have two input variables, a 2^2 full factorial DOE was performed for the first-order statistical model, with the following 4 output variables as the antenna performance figures of merit: resonant frequency f_{res}, minimum return loss RL, maximum gain at 480 MHz G, and the -10 dB bandwidth BW. The ranges of the input variables are presented in Table 4.2, while ε_r and μ_r have been kept at their nominal values of 7.14 and 2.46 respectively.

The first-order models showed curvature in all of the responses, and RSM was needed for the second-order statistical model. Validation of the models was investigated, with all but the BW validated for the normality assumption, and the equal variance was validated for RL and G, but not for f_{res} and BW. The four models are given by Equations 4.2 – 4.5. An interesting result is the fact that the resonant frequency is not dependent upon $\tan\delta_\varepsilon$. This is due to the fact that the interval of analysis of $\tan\delta_\varepsilon$ shown in Table 4.2, chosen based on the real material, is of an order of magnitude smaller than $\tan\delta_\mu$, because $\tan\delta_\varepsilon$ is of an order of magnitude smaller than $\tan\delta_\mu$ and the intervals are chosen to be 20% up and down the center point value. However, when reflected in loss and bandwidth in Equations 4.3 – 4.5, even the much smaller $\tan\delta_\varepsilon$ becomes significant.

$$f_{res}(MHz) = 480.47 - 0.024\left(\frac{\tan\delta_m - 0.039}{0.0078}\right) - 0.013\left(\frac{\tan\delta_m - 0.039}{0.0078}\right)^2 \tag{4.2}$$

$$RL(dB) = -20.34 + 0.18\left(\frac{\tan\delta_e - 0.0017}{0.00034}\right) + 2.48\left(\frac{\tan\delta_m - 0.039}{0.0078}\right) - 0.062\left(\frac{\tan\delta_m - 0.039}{0.0078}\right)^2 - 0.43\left(\frac{\tan\delta_e - 0.0017}{0.00034}\right)\left(\frac{\tan\delta_m - 0.039}{0.0078}\right) \tag{4.3}$$

$$G(dBi) = -4.57 - 0.019\left(\frac{\tan\delta_e - 0.0017}{0.00034}\right) - 0.26\left(\frac{\tan\delta_m - 0.039}{0.0078}\right) - 0.0044\left(\frac{\tan\delta_m - 0.039}{0.0078}\right)^2 + 0.0005\left(\frac{\tan\delta_e - 0.0017}{0.00034}\right)\left(\frac{\tan\delta_m - 0.039}{0.0078}\right) \tag{4.4}$$

$$BW(MHz) = 7.69 + 0.000008\left(\frac{\tan\delta_e - 0.0017}{0.00034}\right) + 0.038\left(\frac{\tan\delta_m - 0.039}{0.0078}\right) - 0.031\left(\frac{\tan\delta_m - 0.039}{0.0078}\right)^2 - 0.005\left(\frac{\tan\delta_e - 0.0017}{0.00034}\right)\left(\frac{\tan\delta_m - 0.039}{0.0078}\right) \tag{4.5}$$

The models allow for the "a priori" prediction of the antenna performance with respect to either figure of merit or all simultaneously allocating any weight factors to each one of them. The goals chosen in this case were a specific f_{res} of 480 MHz (center

point value), maximum gain G, minimum return loss RL, and maximum bandwidth BW, all with equal weight. The surfaces for the four figures of merit as a function of the input parameters are presented in Figure 4.5, indicating the curvature in the models. The values that satisfied the four goals within the ranges presented in Table 4.2 were $tan\delta_\varepsilon = 0.00136$ and $tan\delta_\mu = 0.032427$, leading to the predicted values of the four figures of merit of f_{res} = 480.48 MHz, RL = -22.97 dB, G = -4.32 dBi and BW = 7.63 MHz. So, ideally, these values of the loss tangents would provide optimal performance of the antenna for the above mentioned goals. The models indicate that the resonant frequency decreases with the losses, as the gain and the return loss obviously degrade. For the bandwidth, although the model is significant and shows an increase of the bandwidth with dielectric loss, the absolute numbers in the RSM vary only between 7.61 and 7.7 MHz, which is not a large difference for practical applications.

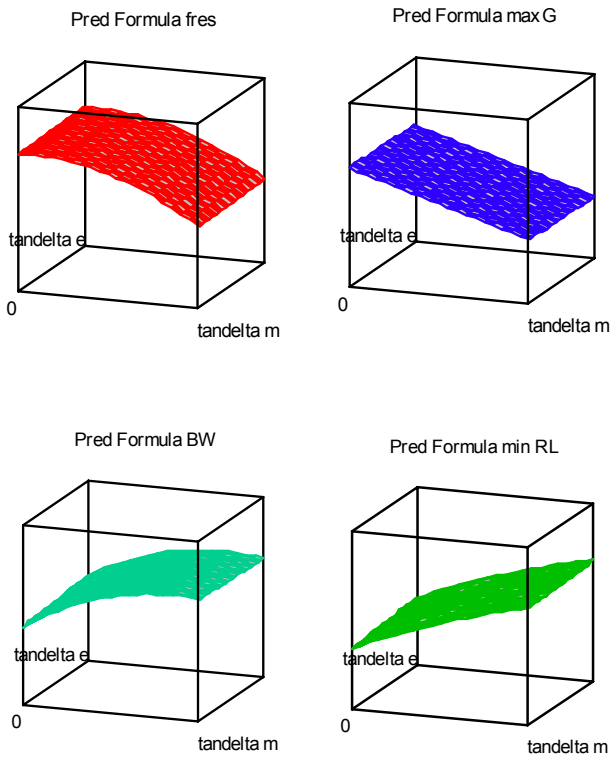

Figure 4.5: Surfaces of possible solutions for outputs.

The consideration of the relative permeability in the antenna design requires a more detailed analysis of its impact, together with the relative permittivity, on the antenna performance. The next statistical experiment analyzes the impact of these two parameters on the same major antenna outputs: resonant frequency f_{res}, minimum return loss RL, maximum gain at the resonant frequency G, and the 10 dB bandwidth BW.

The methodology used is the same as the one used for the loss tangent analysis and shown in Figure 4.4.

Table 4.3 Ranges for the input variables

Variable	Low value "-"	High value "+"	Center point
ε_r	5.712	8.568	7.14
μ_r	1.968	2.952	2.46

In this case, since we have two input variables, the same 2^2 full factorial DOE was performed for the first-order statistical model, with the ranges of the input variables presented in Table 4.3, while $tan\delta_\varepsilon$ and $tan\delta_\mu$ have been kept at their nominal values of 0.0017 and 0.039 respectively.

$$f_{res}(MHz) = 480.61 - 15.19\left(\frac{\varepsilon_r - 7.14}{1.428}\right) - 9.5\left(\frac{\mu_r - 2.64}{0.492}\right) + 1.01\left(\frac{\varepsilon_r - 7.14}{1.428}\right)^2 + 1.46\left(\frac{\mu_r - 2.64}{0.492}\right)^2 \quad (4.6)$$

$$RL(dB) = -20.34 + 1.19\left(\frac{\varepsilon_r - 7.14}{1.428}\right) - 2.78\left(\frac{\mu_r - 2.64}{0.492}\right) + 0.39\left(\frac{\varepsilon_r - 7.14}{1.428}\right)\left(\frac{\mu_r - 2.64}{0.492}\right) - 0.14\left(\frac{\varepsilon_r - 7.14}{1.428}\right)^2 - 0.11\left(\frac{\mu_r - 2.64}{0.492}\right)^2 \quad (4.7)$$

$$G(dBi) = -4.56 - 0.19\left(\frac{\varepsilon_r - 7.14}{1.428}\right) + 0.032\left(\frac{\mu_r - 2.64}{0.492}\right) + 0.0087\left(\frac{\varepsilon_r - 7.14}{1.428}\right)^2 + 0.0024\left(\frac{\mu_r - 2.64}{0.492}\right)^2 \quad (4.8)$$

$$BW(MHz) = 7.68 - 0.35\left(\frac{\varepsilon_r - 7.14}{1.428}\right) - 0.09\left(\frac{\mu_r - 2.64}{0.492}\right) + 0.037\left(\frac{\varepsilon_r - 7.14}{1.428}\right)\left(\frac{\mu_r - 2.64}{0.492}\right) + 0.022\left(\frac{\varepsilon_r - 7.14}{1.428}\right)^2 - 0.029\left(\frac{\mu_r - 2.64}{0.492}\right)^2 \quad (4.9)$$

The first order models showed curvature in all of the responses, and RSM was needed for the second-order statistical model. The validation of the models was investigated. For the normality of residuals assumption, all models but *G* have normally distributed residuals. For the validation of the equal variance of residuals assumption, all the models had equal variance of residuals. The four models are given by Equations 4.6 – 4.9.

The antenna performance was predicted again for the same goals: f_{res} of 480 MHz (center point value), maximum gain *G*, minimum return loss *RL*, and maximum bandwidth *BW*, all with equal weight. The surfaces for the four figures of merit as a function of the input parameters are presented in Figure 4.6, indicating slight curvature in the models. The values that satisfied the four conditions within the ranges presented in Table 4.3 were $\varepsilon_r = 6.41$ and $\mu_r = 2.95$, leading to the values of the four figures of merit of f_{res} = 480.56 MHz, *RL* = -24.08 dB, *G* = -4.42 dBi and *BW* = 7.73 MHz. The models indicate that the resonant frequency decreases with the relative permittivity and permeability, which again proves the miniaturization concept. For the bandwidth and the gain, although the models are significant, the absolute numbers in the RSM vary only between 7.23 – 8.22 MHz for the bandwidth and 4.27 - 4.81 dBi for the gain, which are not large differences for practical applications.

The consideration of the relative permeability in the antenna design requires a more detailed analysis of its impact, together the material parameters, but rather to quantify the effect of the parameters on the system-level performance of the antenna. Even if the two values of $tan\delta_\varepsilon = 0.00136$ and $tan\delta_\mu = 0.032427$ or $\varepsilon_r = 6.41$ and $\mu_r = 2.95$ cannot be achieved simultaneously, this analysis gives a thorough understanding of the effects and provides the designer with a systematic approach in choosing the materials and the antenna geometry.

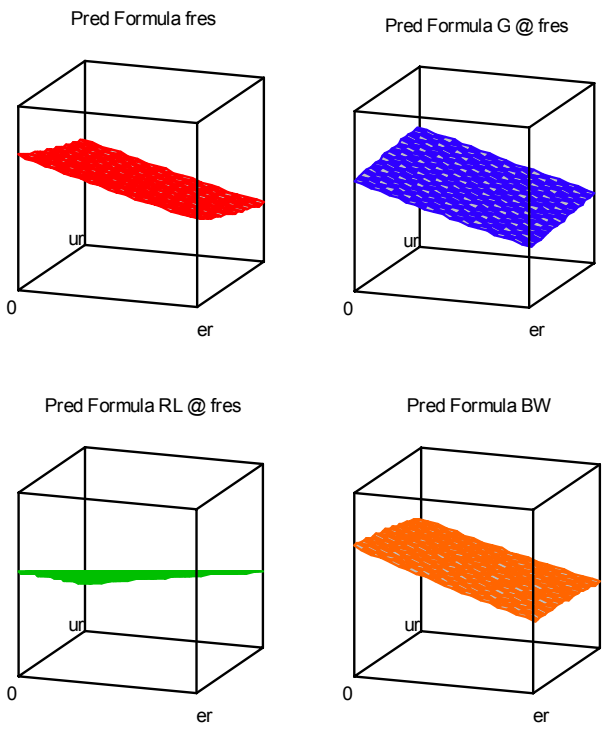

Figure 4.6: Surfaces of possible solutions for outputs.

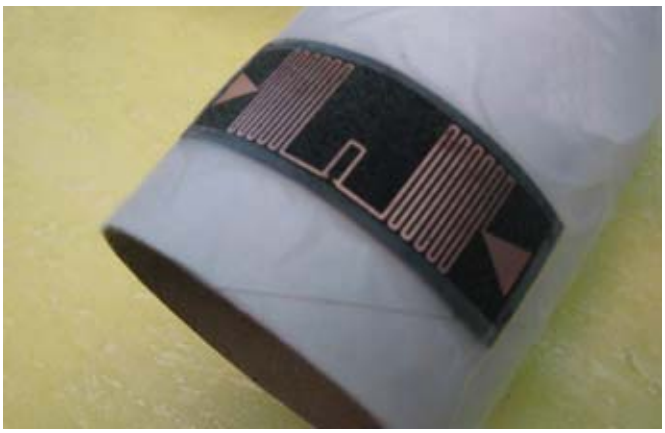

Figure 4.7: Photograph of the conformal RFID tag on a foam cylinder.

4.5 Conformal Performance

In order to verify the performance of the proposed RFID antenna in conformal applications, measurements were performed by conforming the same RFID tag onto a foam cylinder, as shown in Figure 4.7. The radius of the cylinder was chosen to be very small at 27mm, in order to explore the limits of the design. The result in Figure 4.8 shows that the return loss of the fabricated antenna is shifted down by 22 MHz with a center frequency at 458 MHz. Previous results [74] showed a shift of 6 MHz for a lower curvature of 54mm radius, which proves that the shift is increasing with the curvature level. Overall, the antenna still has good performance if the shift in frequency is considered at the beginning of the design process, even for such a large bend. Figure 4.9 shows the radiation patterns for the straight and conformal antennas. The doughnut shape is slightly degraded for the conformal antenna and the maximum gain drops from -4.63 dBi to -7.37 dBi.

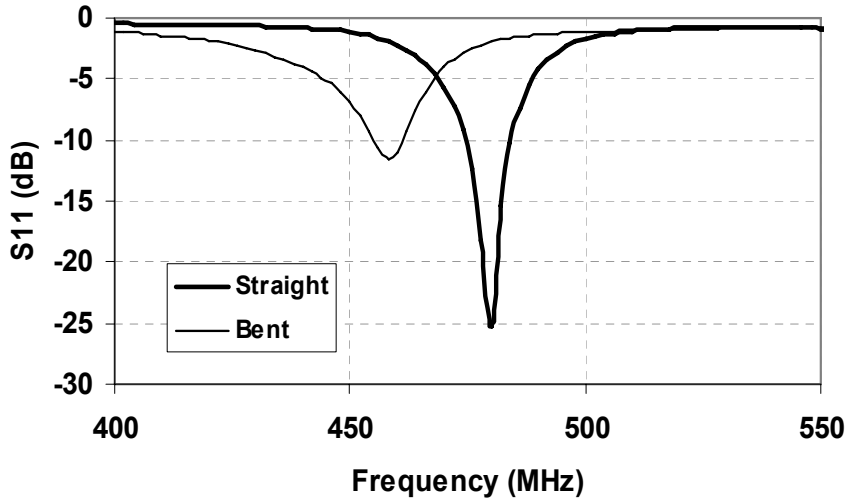

Figure 4.8: Measured return loss of the flat RFID tag and the conformal RFID tag. 20 MHz frequency down shifting is observed.

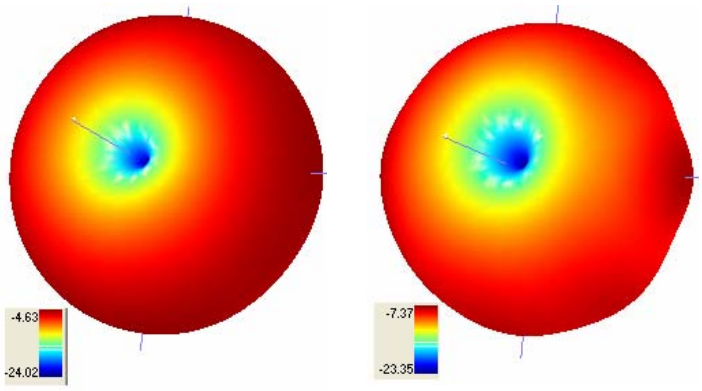

(a) (b)

Figure 4.9: Measured radiation pattern of (a) the flat RFID tag and (b) the conformal RFID tag.

The flexible nature of the proposed substrate enables the RFID tag module's application in various areas where flat surface is hard to find, such as the applications in wireless health monitoring and pharmaceutical drug bottle tracking.

4.6 Chapter Summary

The research work presented in this chapter is the first demonstration of a flexible magnetic composite proven for the 480 MHz bandwidth with acceptable magnetic losses that makes it usable for small size, lightweight conformal applications like wireless health monitoring in pharmaceuticals, hospital, ambulance and home-based patient care. A combination of electromagnetic tools and measurements has been used to investigate the impact of magnetic composite materials to the miniaturization of RFID antennas considering geometric and material parameters, as well as conforming radius. This approach has been applied to the design of a benchmarking conformal RFID tag module and has enabled the assessment of implication that the choice of materials have on this design, specifically the antenna miniaturization by using the magnetic composite vs. pure silicone. A real composite material has been fabricated and the performance of the

miniaturized antenna predicted using the models. Next, the important issues of the dielectric and magnetic losses have been addressed by performing a thorough statistical analysis to investigate the impact of the losses on the antenna performance. Furthermore, since the permeability was first introduced in this chapter for a conformal anternna, the impact of the relative permeability in conjunction with relative permittivity were addressed together in another statistical analysis. The losses impact the resonant frequency, return loss, and antenna gain, whereas the dielectric constant and magnetic property mostly decrease the resonant frequency, thus proving the miniaturization concept.

CHAPTER 5

RFID-ENABLED GAS SENSOR UTILIZING INKJET-PRINTED CARBON NANOTUBES

This chapter introduces the integration of a conformal RFID antenna with a single-walled carbon nanotube (SWNT) composite in a chipless RFID node for toxic gas detection. The electrical performance characterization of the inkjet-printed SWNT film is also reported up to 1 GHz. The whole module is realized by inkjet printing on a low-cost paper-based substrate and the RFID tag is designed for the European UHF RFID band. The electrical conductivity of the SWNT film changes in the presence of very small quantities of toxic gases like ammonia and nitrogen oxide, resulting in the variation of the backscattered power level which can be easily detected by the RFID reader to realize reliable wireless toxic gas sensing.

5.1 Motivation

As the demand for low cost, flexible and power-efficient broadband wireless electronics increases, the materials and integration techniques become more and more critical and face more challenges, especially with the ever growing interest for “cognitive intelligence” and wireless applications, married with RFID technologies. This demand is further enhanced by the need for inexpensive, reliable, and durable wireless RFID-enabled sensor nodes that is driven by several applications, such as logistics, Aero-ID, anti-counterfeiting, supply-chain monitoring, space, healthcare, pharmaceutical, and is regarded as one of the most disruptive technologies to realize truly ubiquitous ad-hoc networks. Hence, the two major challenges for such applications are the choice of the material and the advanced integration capabilities. The choice of paper or LCP as the substrate material presents multiple advantages and has established the organic substrate

as the most promising materials for UHF RFID applications: their high biodegradability with respect to other ceramic substrates such as FR-4, requiring only months to turn into organic matter in land-fills. Previous research work has demonstrated the successful development of fully inkjet-printed RFID modules on paper. The next challenge is to integrate the sensor on the paper substrate as well.

From the power consumption prospect, RFID-enabled sensors can be divided into two categories: active ones and passive ones. The active RFID-enabled sensor tags use batteries to power their communication circuitry, and benefit from relatively long wireless range. However, the need of external battery limits their applications to where battery replacements are only possible and affordable. Battery technology is mature, extensively commercialized, and completely self-contained. However, given current energy density and shelf-life trends, even for relatively large batteries and conservative communication schedules, the mean time to replacement is only a year or two. For some applications, such as harsh environment monitoring, in which battery changing is not easy, the problem is aggravated significantly. Concerns over relatively short battery life have restricted wireless device applications.

Researchers have been looking for passive RFID-enabled sensor solutions. Some passive RFID prototypes for sensing applications have been proposed [82][83]. However, the sensing capabilities are usually realized by adding a discrete sensor or a special coating to the RFID tag, resulting in the difficulty in low-profile integration. Plus, the sensitivity is usually low. Therefore, there has been a growing interest in looking for new materials in RFID sensing applications: an ultra sensitive composite which can be printed directly on the same paper together with the antenna, for a low cost, flexible, highly integrated RFID module.

5.2 Inkjet-printed SWNT

Carbon nanotubes (CNT) represent one of the most promising materials in the environmental sensor field since the discovery of multi-walled CNT (MWNT) initially tagged as "helical microtubes of graphitic carbon" by Iijima in 1991 [84]. To date, single-walled CNT (SWNT) has attracted most extensive attention due to the relatively simple structures and easy prediction of properties by theoretical calculations. The geometrical structure of an SWNT can be seen as a cylindrical roll-up of a shingle sheet of graphene, as shown in Figure 5.1.

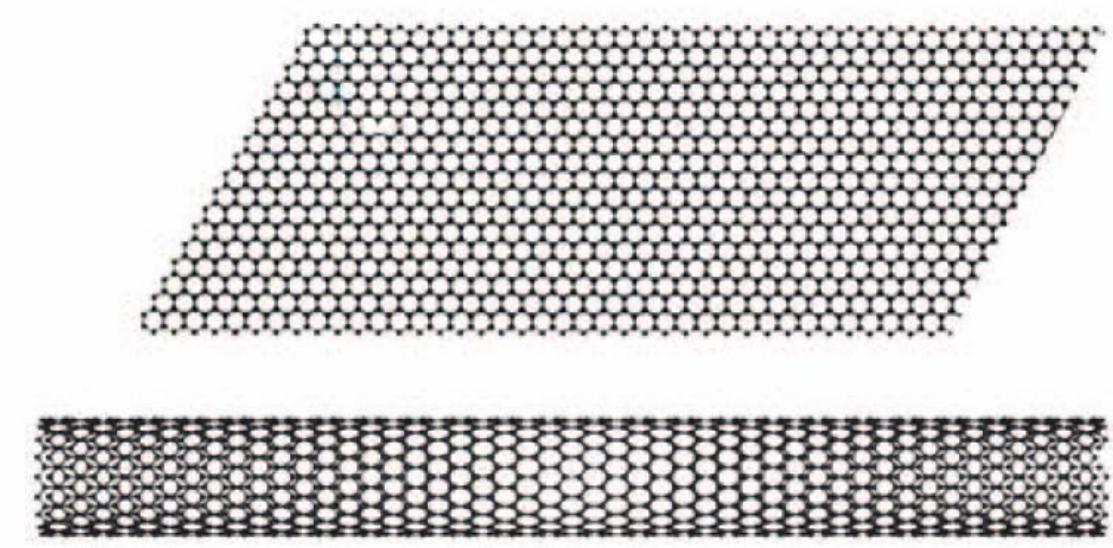

Figure 5.1: Schematic illustration of a graphene sheet and a single-walled carbon nanotube.

CNT has shown sensitivity towards extremely small quantities of gases, such as ammonia (NH_3) and nitrogen dioxide (NO_2). Due to the distortion of the electron clouds of CNT from a uniform distribution in graphite to asymmetric distribution around cylindrical nanotubes, a rich π-electron conjugation forms outside of the CNT, making it electrochemically active [85]. The electrical properties of CNT are extremely sensitive to charge transfer and chemical doping effects by various molecules. When electron-

withdrawing molecules (e.g. NO_2) or electron-donating molecules (e.g. NH_3) were absorbed by the semiconducting CNT, as shown in Figure 5.2, they will change the density of the main charge carriers of the nanotube, with changes the conductance of CNT. This behavior forms the basis for applications of CNT as electrical chemical gas sensors.

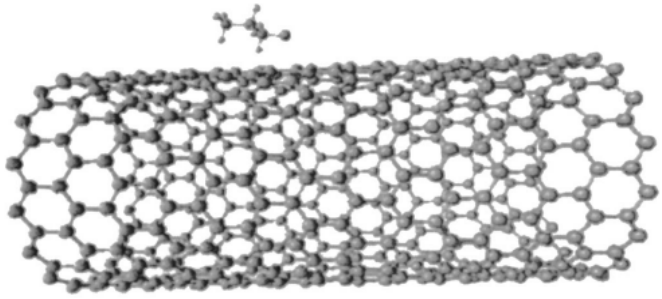

Figure 5.2: Schematic geometry of SWNT with a molecule absorbed on its external surface.

The ability to monitor the leakage of NH_3 and NO_2 in the air is important, because both chemicals adversely affect human and environmental health [86]. NH_3 is primarily a concern in areas of high agricultural activity, because it is a natural waste product of livestock, but industrial sources include the manufacturing of basic chemicals, metals, and textiles products as well as automotive emissions. High levels of NH_3 can result in irritation to the eyes and respiratory tracts of humans and can negatively impact wildlife, livestock, and agricultural health. NO_2 is also a potentially toxic gas that can lead to respiratory symptoms in humans and detrimentally influence the growth of agriculture. Furthermore, atmospheric concentrations of either gas can lead to the creation of ground-level smog and acid rain.

Carbon Nanotube (CNT) composites have been found to be compatible with inkjet printing [87]. As a direct-write technology, inkjet printing transfers the pattern directly to the substrate. Due to its capability of jetting one single ink droplet in the

amount as low as 1 pl, it has widely drawn attention from the industrial world as a more accurate and economic fabrication method than the traditional lithography method. However, due to the insufficient molecular network formation among the inkjet-printed CNT particles at nano-scale, instabilities were observed in both the resistance and, especially, the reactance dependence on frequency above several MHz, which limits the CNT application in only DC or LF band [88]. To enable the CNT-enabled sensor to be integrated with RFID antenna at UHF band, a special recipe needs to be developed.

The SWNT is synthesized by using the electric arc discharge method and refer to as AP-SWNT [89]. The ratio of semiconducting to metallic SWNT produced through this method is 2 : 1. The nanotubes are produced using nickel/yttrium catalyst. Individual tube lengths range from 0.5-3μm and have an average diameter of 1.4 nm. SWNT tend to occur as bundles with bundle lengths of 1-5μm and average bundle diameters of 2-10nm. Two types of SWNT, namely, P2-SWNT and P3-SWNT were tested. Both of these types of nanotubes are purified from AP-SWNT. The difference is in the way they are purified. P2-SWNT is developed from purified AP-SWNT by air oxidation and catalyst removing. P3-SWNT is developed from AP-SWNT purified with nitric acid. P2-SWNT and P3-SWNT are materials of the same quality, but with different characteristics: P2-processing produces high purity material with almost no functionalities, while P3-material has the same carbonaceous and metal content purity, but it is more compatible with further chemical processing. A specific feature of P3-SWNT is the presence of carboxylic acid groups, which makes this material dispersible in water and other solvents and more compatible with further chemical processing including composite applications. Typically, P3-SWNT has 3-6 % carboxylic acid groups.

Compared with P2-SWNT, P3-SWNT has much higher functionality and is easier to disperse in the solvent. In experiments, P2-SWNT started to aggregate at the concentration lower than 0.1mg/ml, while P3-SWNT can go up to 0.4mg/ml and still show good dispersion. Therefore, P3-SWNT was selected for latter steps.

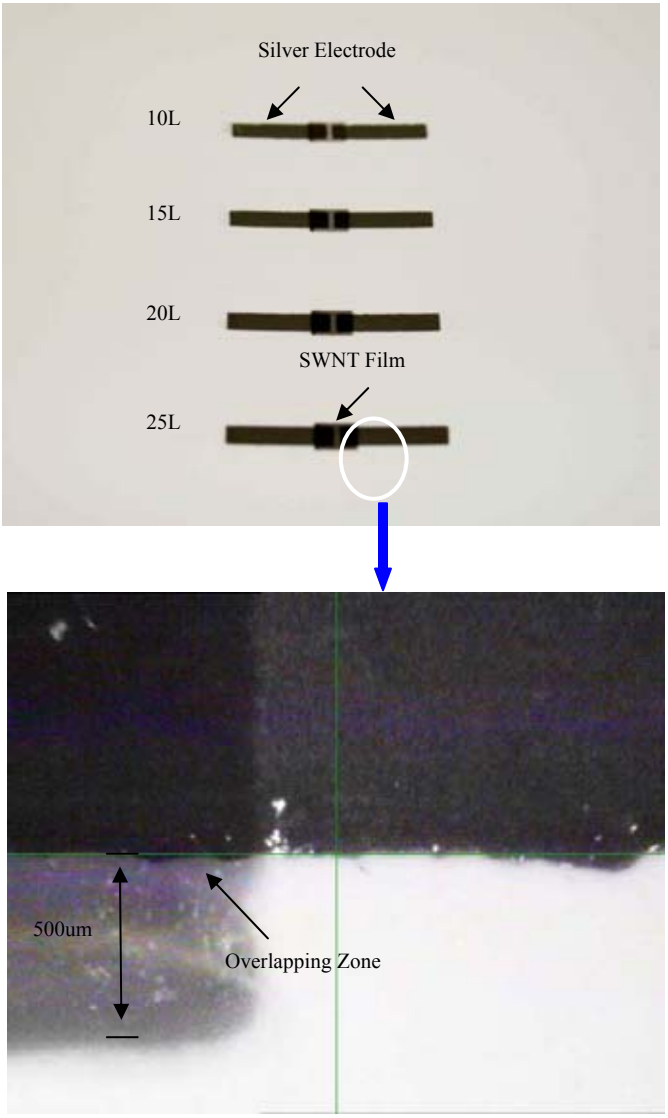

Figure 5.3: Photograph of the inkjet-printed SWNT films with silver electrodes. The SWNT layers of the samples from up to down are 10, 15, 20 and 25, respectively.

The sample SWNT powder was dispersed in DMF, a polar aprotic solvent. The concentration of the ink was 0.4mg/ml. This high concentration helped the nano particle network formation after printing; otherwise there would be instability in the impedance response versus frequency of the SWNT film due to insufficient network formation, such as a sharp dropping of resistance value after 10 MHz [83]. The diluted solution was

purified by sonication for 12 hours to prevent aggregations of large particle residues. This is important to avoid the nozzle clogging by SWNT flocculation during the printing process. Dimatix DMCLCP-11610 printer head was used to eject the SWNT ink droplet.

Silver electrodes were patterned with the nano-practical ink from Cabot before depositing the SWNT film, followed by a 140˚C sintering. The electrode finger is 2mm by 10mm with a gap of 0.8mm. Then, the 3mm by 2mm SWNT film was deposited. The 0.6mm overlapping zone is to ensure the good contact between the SWNT film and the electrodes. Four devices with 10, 15, 20 and 25 SWNT were fabricated to investigate the electrical properties. Figure 5.3 shows the fabricated samples.

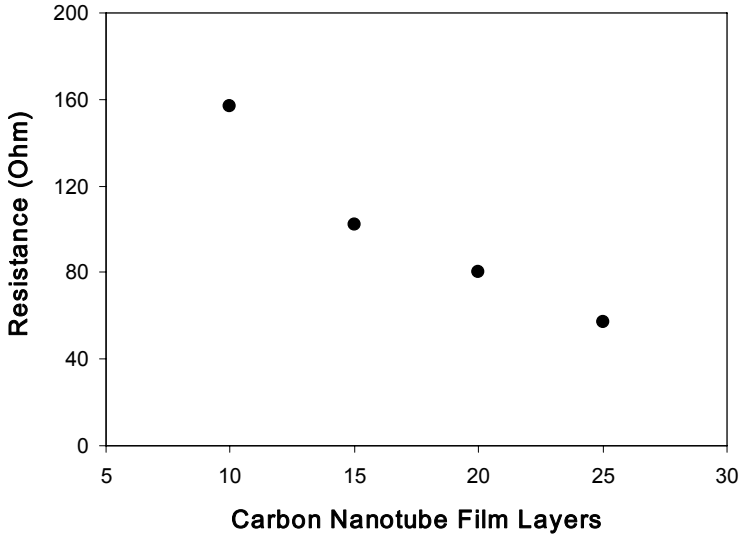

Figure 5.4: Measured DC electrical resistance of SWNT films.

CNT composites have an affinity for gas molecules. The absorption of gas molecules in the CNT tubes changes the conductivity of the material, which can be explained by the charge transfer of reactive gas molecules with semiconducting CNT. The electrical resistance of the fabricated device was measured by probing the end tips of the two electrodes. The DC results are shown in Figure 5.4. The resistance goes down when the number of SWNT layers increases. Since a high number of SWNT overwritten

layers will also help the nano particle network formation, 25-layer film is expected to have the most stable impedance-frequency response and selected for the gas measurement. In the experiment, 4% consistency ammonia, which was widely used in chemistry plants, was guided into an 18-inch tube-shape gas flowing chamber connected with an exhaust hood. The test setup is shown in Figure 5.5. The SWNT film exhibits a fast while monotonic impedance response curve to the gas flow [24]. A network vector analyzer (Rohde&Schwarz ZVA8) was used to characterize the SWNT film electrical performance at UHF band before and after the gas flowing. A GS probe was placed on the silver electrodes for the impedance measurements. The calibration method used was short-open-load-thru (SOLT). In Figure 5.6, the gas sensor of SWNT composite shows a very stable impedance response up to 1GHz, which verifies the effectiveness of the developed SWNT solvent recipe. At 868MHz, the sensor exhibits a resistance of 51.6Ω and a reactance of -j6.1Ω in air. After meeting ammonia, the resistance was increased to 97.1Ω and the reactance was shifted to -j18.8Ω.

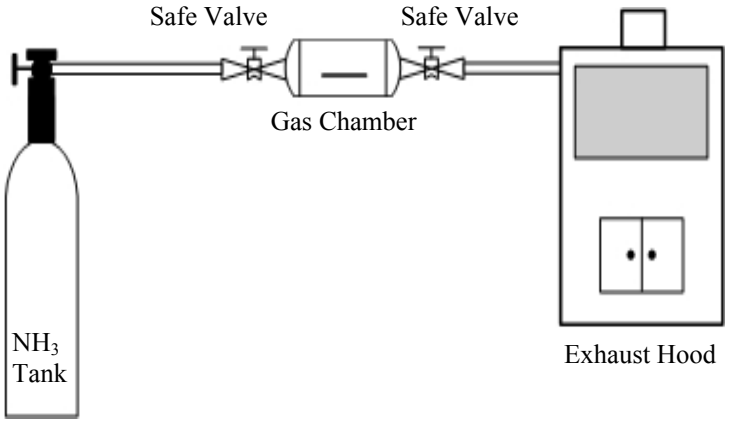

Figure 5.5: Schematic of NH_3 gas detection measurement.

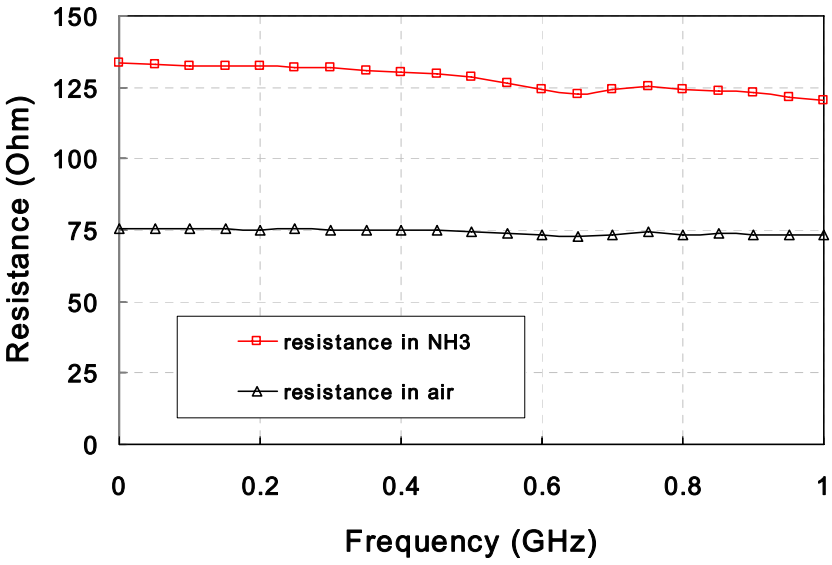

(a)

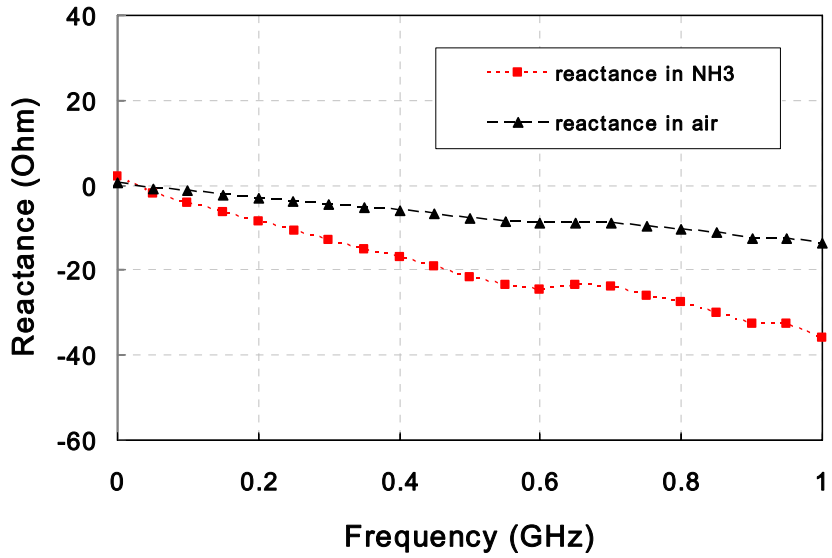

(b)

Figure 5.6: Measured impedance characteristics of SWNT film with 25 layers: (a) resistance (b) reactance.

5.3 RFID Tag Module

A passive RFID system operates in the following way: the RFID reader sends an interrogating RF signal to the RFID tag consisting of an antenna and an IC chip as a load. The IC responds to the reader by varying its input impedance, thus modulating the backscattered signal. The modulation scheme often used in RFID applications is

amplitude shift keying (ASK) in which the IC impedance switches between the matched state and the mismatched state [90]. The power reflection coefficient of the RFID antenna can be calculated as a measure to evaluate the reflected wave strength:

$$\eta = \left| \frac{Z_{Iload} - Z_{ANT}^{*}}{Z_{load} + Z_{ANT}} \right|^2 \tag{5.1}$$

where Z_{Load} represents the impedance of the load and Z_{ANT} represents the impedance of the antenna terminals with Z_{ANT}* being its complex conjugate. The same mechanism can be used to realize RFID-enabled sensor modules. The SWNT film functions as a tunable resistor Z_{Load} with a value determined by the existence of the target gas. The RFID reader monitors the backscattered power level. When the power level changes, it means that there is variation in the load impedance, therefore the sensor detects the existence of the gas, as illustrated in Figure 5.7.

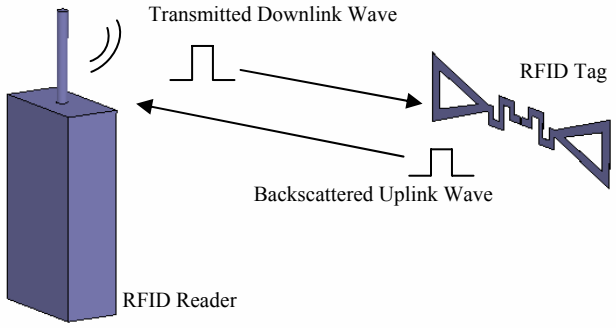

Figure 5.7: Conceptual diagram of the proposed RFID-enabled sensor module.

The expected power levels of the received signal at the load of the RFID antenna can be calculated using Friis free-space formula, as

$$P_{tag} = P_t G_t G_r \left(\frac{\lambda}{4\pi d} \right)^2 \tag{5.2}$$

where P_t is the power fed into the reader antenna, G_t and G_r is the gain of the reader antenna and tag antenna, respectively, and d is the distance between the reader and the tag.

Due to the mismatch between the SWNT sensor and tag antenna, a portion of the received power would be reflected back, as

$$P_{ref} = P_{tag}\eta \tag{5.3}$$

where η is the power reflection coefficient in Equation 5.1. Hence the backscattered power received by the RFID reader is defined as

$$P_r = P_{ref} G_t G_r \eta \left(\frac{\lambda}{4\pi d}\right)^2 = P_t G_t^2 G_r^2 \eta \left(\frac{\lambda}{4\pi d}\right)^4 \tag{5.4}$$

or written in a decibel form, as

$$P_r = P_t + 2G_t + 2G_r - 40\log_{10}\left(\frac{4\pi}{\lambda}\right) - 40\log_{10}(d) + \eta \tag{5.5}$$

where except the term of η, all the other values remain constant before and after the RFID tag meets gas. Therefore the variation of the backscattered power level solely depends on η, which is determined by the impedance of the SWNT film.

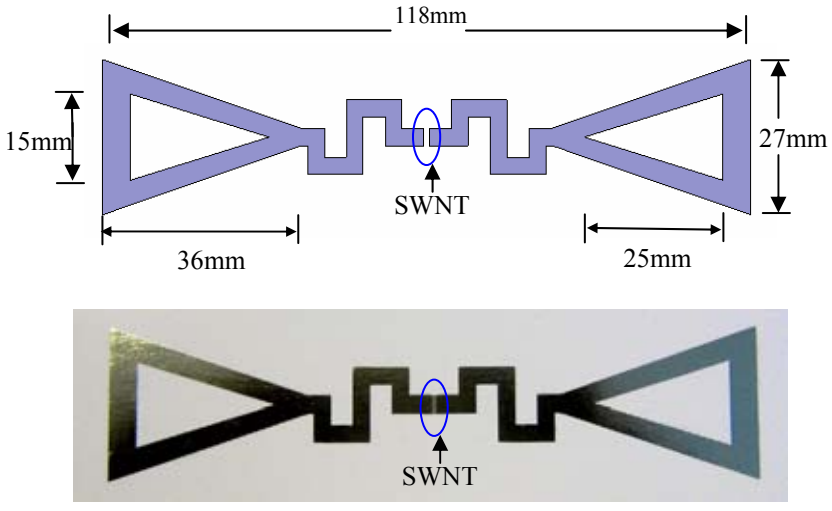

Figure 5.8: The RFID tag module design on flexible substrate: (a) configuration (b) photograph of the tag with inkjet-printed SWNT film as a load.

A bowtie meander line dipole antenna was designed and fabricated on a 100 μm thickness flexible paper substrate. The RFID prototype structure is shown in Figure 5.8 along with dimensions, with the SWNT film inkjet printed in the center. The nature of the bowtie shape offers a more broadband operation for the dipole antenna.

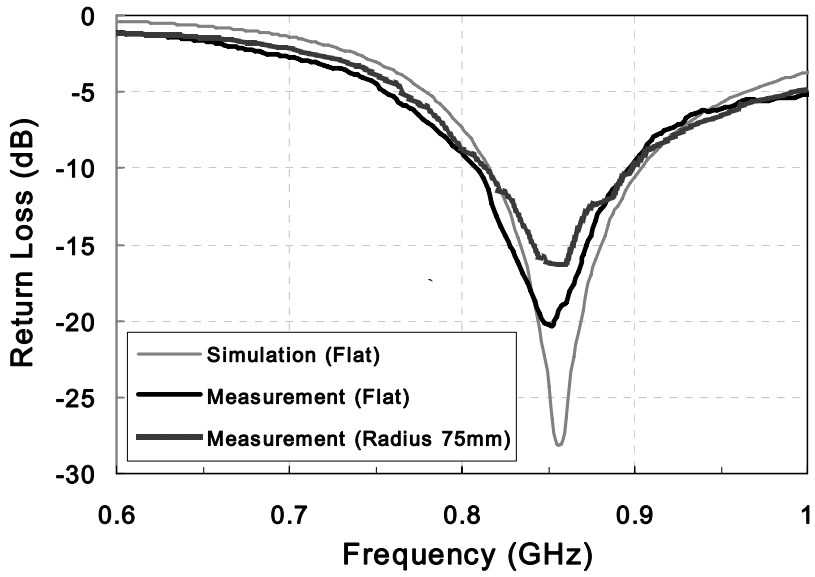

Figure 5.9: Simulated and measured return loss of the RFID tag antenna.

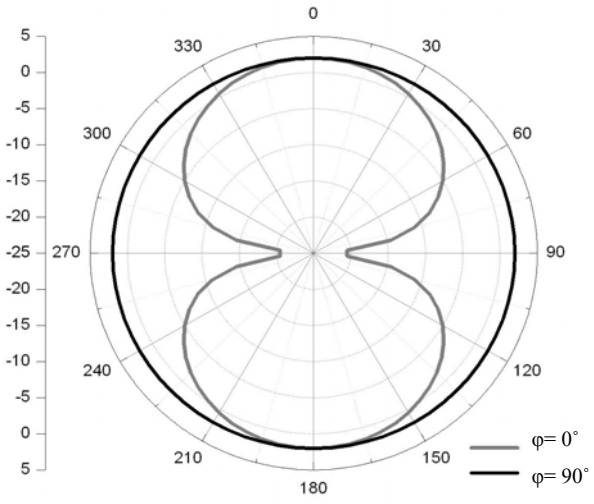

Figure 5.10: Far-field radiation pattern plots.

A dielectric probe station was used for the impedance measurements. The measured Z_{ANT} at 868MHz is 42.6+j11.4 Ω. The simulation and measurement results of the return loss of the proposed antenna are shown in Figure 5.9, showing a good agreement. The tag bandwidth extends from 810MHz to 890MHz, covering the whole European RFID band. The radiation pattern is plotted in Figure 5.10, which is almost omnidirectional at 868 MHz with directivity around 2.01 dBi and 94.2% radiation efficiency. In order to verify the performance of the conformal antenna, measurements were performed as well by sticking the same tag on a 75 mm radius foam cylinder. As shown in Figure 5.9, there is almost no frequency shifting observed, with a bandwidth extending from 814MHz to 891MHz. The directivity is slightly decreased to 1.99dBi with 90.3% radiation efficiency. Overall a good performance is still remained with the interested band covered. Figure 5.11 shows the photograph of the designed conformal tag.

Figure 5.11: Photograph of the conformal tag with a SWNT film in the center.

In air, the SWNT film exhibited an impedance of 51.6-j6.1 Ω, which results in a power reflection at -18.4 dB. When NH3 is present, SWNT film's impedance was shifted to 97.1-j18.8 Ω. The mismatch at the antenna port increased the power reflection to -7.6 dB. From Equation 5.5, there would be 10.8 dBi increase at the received backscattered

power level, as shown in Figure 5.12. By detecting this backscattered power difference on the reader's side, the sensing function can be fulfilled.

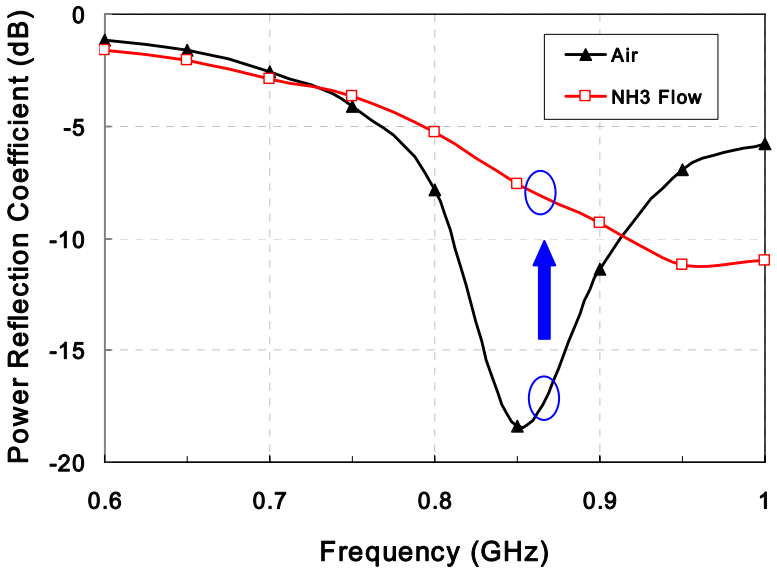

Figure 5.12: The power reflection coefficient of the RFID tag antenna with a SWNT film before and after the gas flow.

5.4 Chapter Summary

The inkjet printing method has been utilized for the first time to deposit SWNT film on a fully-printed UHF RFID module on paper to form a wireless gas sensor node. To ensure reliable inkjet printing, a SWNT ink solution has been developed. . The printed CNT particles were SWCNT, which were dispersed in dimethylformamide (DMF) solution and sonicated to meet the viscosity requirement for the inkjet printer. The impedance of the SWCNT film forms the sensor part. The impedance performance of the SWNT film was characterized up to 1GHz for the first time. The antenna was printed first, followed by the 25 layers of the dispersed SWCNT as a load with "gas-controlled" value. When 4% consistency ammonia was imported into the gas chamber, the SWCNT impedance changed from 51.6-j6.1 Ω to 97.1-j18.8 Ω at 868 MHz, resulting in a 10.8 dBi

variation in the backscattered power from the tag antenna, which can be easily detected by the RFID reader to realize the “real-time” gas detection. The design demonstrates the great applicability of inkjet-printed CNT for the realization of fully-integrated “green” wireless RFID-enabled flexible sensor nodes based on the ultrasensitive variability of the resistive properties of the CNT materials, and also illustrates the design of novel ultrasensitive passive RFID-enabled sensors.

CHAPTER 6

WEARABLE BATTERY-FREE ACTIVE RFID TAG WITH ENERGY SCAVENGER

This chapter presents the embodiment of wearable battery-free active RFID tags assisted with energy scavenging technique on flexible organic substrate. The state-of-the-art long-range RFID tag is realized by active RFID topology that requires the power supply. Until now, chemical-cell batteries have been sufficient, but replacing them is a costly nuisance, and this solution will become less practical as demands evolve. In this research, extraction of electrical energy from human body movement will be realized by the energy scavenger to power up the active RFID tag module on flexible organic substrate. This will also serve as a promising solution for wearable electronics.

6.1 Background

Over the past few years there has been an increasing focus on wearable electronics, which enable people to carry their personal wireless body-area network (WBAN) that provides medical, lifestyle, assisted living, mobile computing, and tracking functions for the user. Sensing and identification are the key functions of such application [91]. RFID technology will play an important role in this technology wave, since most business and manufacturing identification needs have supported the development and adoption of smaller, cheaper, and longer-range RFID tags. Solutions compatible with RFID standards find quicker acceptance and see faster improvement than other solutions [82].

Unfortunately, the very properties that make WBAN nodes attractive for these applications – low profile, wireless identification, and timely, long-term radio communication data – make powering them a challenge. Particularly challenging is the

production of an energy source that is tiny and possesses a long average time to replace yet can supply enough power for operation and wireless communication. Since Alessandro Volta invented the battery in 1799, batteries provided the world's first practical electricity source. However, until today, as electronics became smaller and required less power, ubiquitous computing's dream of wireless nodes is accompanied by the nightmare of battery replacement and disposal. For example, Figure 6.1 depicts the relative improvements in laptop computing technology from 1990-2003 [92]. As the graph indicates, the slowest trend in the mobile computing is the battery energy. Although new materials are revolutionizing the battery's form factor, its energy density proceeds a long flattening curve. Overcoming this trend requires moving to another energy source – harvesting energy from ambient environment. For the wearable electronics, the solution is the developing and storing electric energy at the devices themselves by scavenging waste energy from human activities [93].

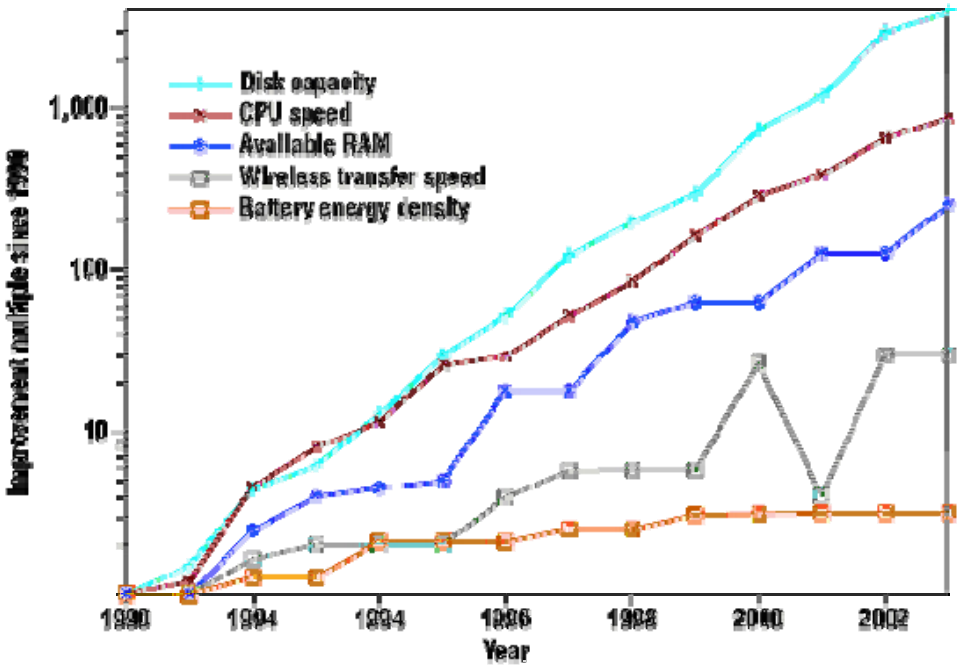

Figure 6.1: Increases in the performance of laptop computers from 1990-2003. The dip marks the removal of the Metricom network [92].

As the entire energy consumption of the RF communications unit must be scavenged form the human activity, the choice of energy scavenging technology is crucial. Numerous studies and experiments have been conducted to investigate the levels of energy that could be harnessed. A compilation of various power densities derived from various energy scavenging sources is listed in Table 6.1 [94].

Table 6.1 Power Density Comparison

Energy Source	Performance	Notes
Solar	100 mW/cm^2	sunlight
	100 uW/cm^2	room light
Thermoelectric	60 uW/cm^2	5˚C gradient
Vibration	5 uW	wrist watch – walking motion
	1 mW	wrist watch – shaking
Human Motion	0.93 W	blood pressure at 100 mmHg
	7 W	heel strike with 1 cm defection

It is clearly seen that solar energy under bright sunlight has the best performance in terms of power density, measured up to 100 mW/cm^2, but only 100 uW/ cm^2 in a typically illuminated office. The energy conversion efficiency of relatively inexpensive crystalline silicon solar cell modules is generally below 20% and closer to 10% for flexible amorphous silicon panels. Accordingly, the lack of strong, consistent sunlight constrains applications.

Thermoelectric modules harvest energy via heat transfer offered by objects at different temperatures. The Carnot cycle provides the fundamental limit to the energy obtained from a temperature difference. Carnot efficiencies are limited for small temperature difference. Although energy conversion efficiencies can achieve close to10% for 200 ˚C to 20 ˚C, typical efficiency for thermoelectric generators is less than 1% for temperature gradient from 40 ˚C to 20 ˚C, limited for wearable applications.

Human body is an under-estimated energy source which is continuously generating steady thermoelectric, blood pressure and motion energy outputs. For example, it has been shown that the heat flow generated by the human body creates a power density of about 20 mW/cm^2 on average. Ramsay and Clark [26] found that output power generated from blood pressure at 100 mmHg is about 0.93 watts. Paul Mitcheson [29] has proposed several forms of vibration-driven MEMS microgenerator using the motion of the human body to produce power at the scale of tens of microwatts. Thad Starner's investigation [27] analyzed different kinds of human activities and found that the heel strike during walking is a plentiful and readily tapped source of waste energy. Starner estimated that average 67 watts of power are generated in the heel movement of a 68 kg person walking at a brisk pace. Admittedly, scavenging most of that energy unobtrusively would be impossible. But even a small percentage of it would provide enough power to operate many of the body-worn systems on the market today. In this research, the critical requirement of the energy source is that some significant energy is required for a very short period of time needed to transmit a few packets of information bit through the active RFID in a wireless manner. Hence after evaluation of the possible energy sources and performances, piezoelectric pushbutton is chosen to be embedded in a shoe of which the sole and the heel platform would make an ideal test bed for exploring body-energy harvesting.

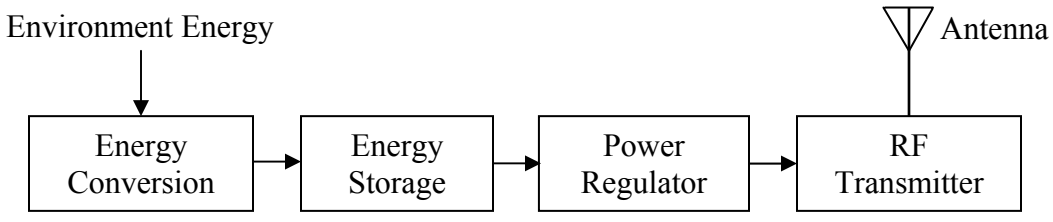

Figure 6.2: Block diagram of an active RFID tag driven by the energy harvesting unit.

6.2 Energy Harvesting Unit

Figure 6.2 depicts the block diagram of an active RFID tag driven by an energy harvesting unit. The key components of the system include the power generator / energy conversion device, energy storage device, power regulator circuit and a RF transmitter that will broadcast its encoded RFID ID and the stored information bits.

To scavenge the human walking strike power, a piezoelectric pushbutton is chosen due to its compactness, simplicity, relative low cost in terms of power density and energy requirement. The piezoelectric effect – a material's capacity to convert mechanical energy into electrical energy, and the inverse – is observable in a wide array of crystalline substances that have asymmetric unit cells. When an external force mechanically strains a piezoelectric element, these polarized unit cells shift and align in a regular pattern in the crystal lattice. The discrete dipole effects accumulate, developing an electrostatic potential between opposing faces of the element. Piezoelectric pushbutton has been widely used in the industries for gas lighting, for example, to be integrated in an igniter. When the piezoelectric pushbutton is pressed, a spring inside will be compressed. When the pressure exceeds a threshold, the spring-loaded hammer will be released that delivers a dynamic mechanical force to the piezoelectric element. Once the hammer strikes the piezoelectric element, a pressure wave is generated and reflected several times between the hammer and the element creating a mechanical resonance [95]. During this process, some mechanical energy will be converted by the piezoelectric element to electrical energy and be scavenged. The output voltage generated will follow similarly to an AC signal because of the dynamic polarization of the piezoelectric element [95]. The pushbutton is 35 mm long and 5 mm in diameter, has a deflection of 4.5 mm at a maximum force of 15 N. Since piezoelectric element produces high voltages at low currents, and RF transmitter circuitry requires low voltages at high currents, a step-down transformer is used for better match impedance to the latter circuitry. An amorphous-core device with a 25:1 turns ratio was chosen that transforms a peak of voltage close to a

thousand volts at the piezoelectric element down to tens of volts. The selected piezoelectric pushbutton and the step-down transformer are shown in Figure 6.3.

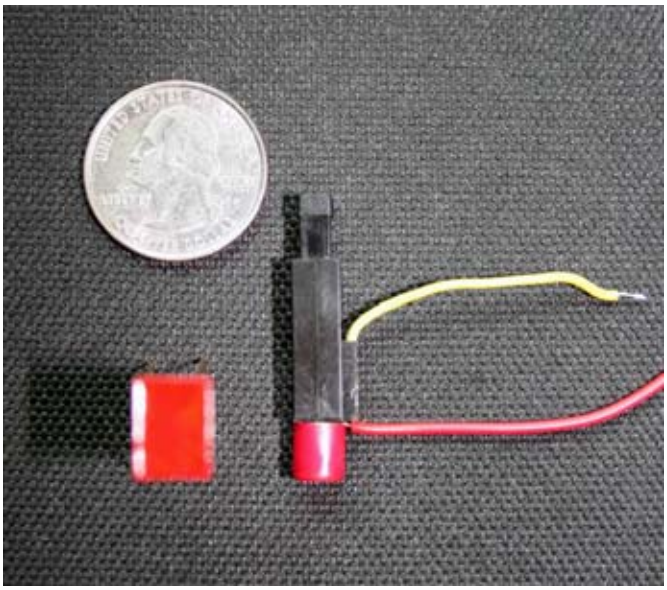

Figure 6.3: Photo of the piezoelectric pushbutton and the step-down transformer.

Since the piezoelectric pushbutton harvests energy pulse at a transient time span of micron seconds and the RF transmitter takes typically tens of milliseconds for a complete word transmission, an energy storage device is needed to store the generated electrical energy when the external power source is temporarily unavailable. Therefore, the RF transmitter can consume energy without interruption from the energy storage device instead of directly from the piezoelectric element until the next harvesting cycle. Rechargeable batteries could be used. However, this would not be the perfect solution concerning the goal of completely maintenance free active RFID tag, since such elements can barely survive for a few years [95]. As an alternative solution, a 4.7 *u*F tank capacitor is used in this research to integrate the charge transferred from a button strike. Additionally, the capacitor acts as a filter which smoothes the voltage ripples in the raw harvested electrical energy.

Power regulator circuit has two major functions, one is to convert the AC voltage from the piezoelectric element into a DC source through AC-DC full wave diode bridge rectification, and another is to regulate the DC voltage across the capacitor to 3 V by a DC linear regulator. MAX666 low-dropout linear regulator, which provides a stable 3 V supply until the tank capacitor's charge is drain below the reference level of the DC linear regulator, is selected. When the MAX666 is activated, the RF transmitter will be enabled, producing a serial ID broadcast.

6.3 Shoe-mounted Antenna Design

Typically, antenna performance is the first consideration of antenna design and optimization. Little attention is paid to other aspects, such as aesthetic appearance. The requirements of wearable electronics present a considerable design challenge to the antenna design technique. First, the antenna needs to be conformal to fit in the garment or shoes where almost no flat surface can be found. Traditional rigid antenna formation is not suitable for this situation. Second, the active UHF RFID band allocates at 433 MHz with a 69 cm free space wavelength which is at the scale of human body. This requires the antenna to be unobtrusive, low-profile and comfortable to wear. Third, the antenna needs to have robust performance at the presence of the human body. The existence of the human tissue will detune the performance of the antenna. At 433 MHz, antennas are physically larger and can not incorporate an effective ground plane to remain unobtrusive, so the body must be considered.

In this section, a shoe-mounted antenna is proposed for a proof-of-concept antenna design that uses company logo as the antenna configuration. In this design, the logo printed on the shoes serves as the antenna, and there would be no extra space needed to reserve for the antenna. Another obvious direct benefit brought by this integration is that the customer would not feel the obtrusive existence of the wearable electronics.

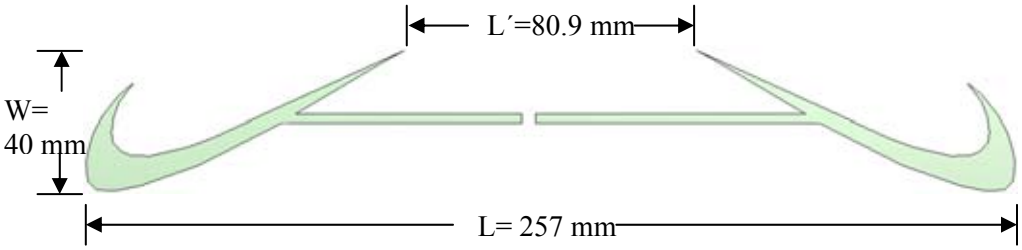

(a)

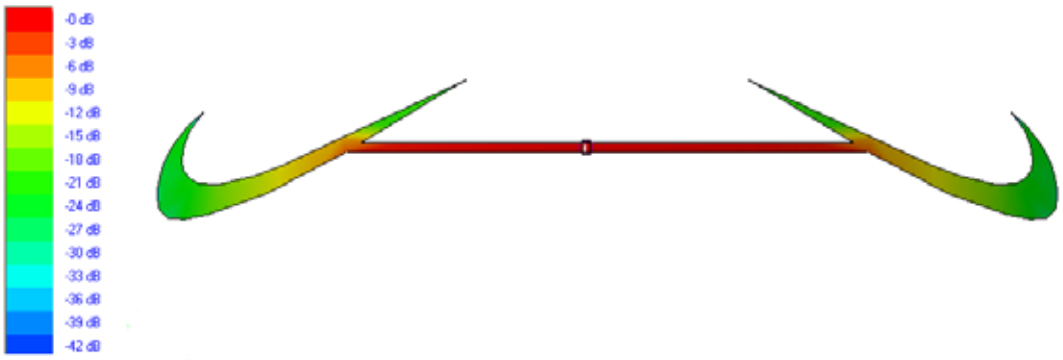

(b)

Figure 6.4: The shoe logo RFID tag antenna: (a) schematic configuration with dimensions (b) current density distribution.

The proposed structure is shown in Figure 6.4(a). A commercial shoe company logo was selected for the proof of concept to serve as the major radiating body of the shoe-mounted antenna. The center feeding is located in the back of the shoe, which will be connected to the output port of the RF transmitter. The Nike logos are on the both sides of the shoe, connected to the center feeding by strip lines. The whole structure is within a rectangular region of 257 mm x 40 mm, which can be easily fit into an adult size shoe. The antenna was inkjet printed by a Dimatix material printer on a hydrophobic paper substrate.

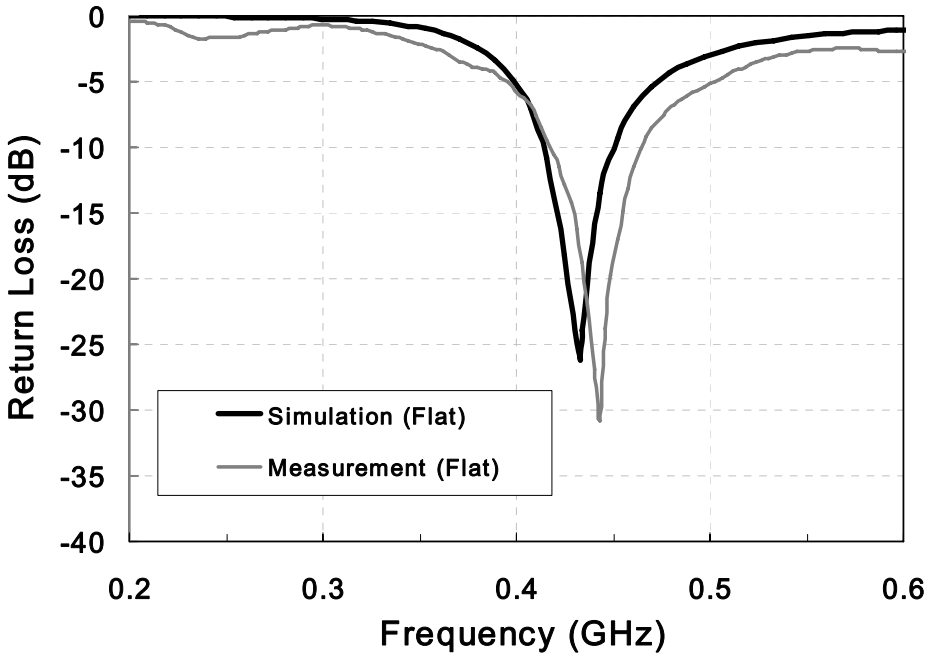

Figure 6.5: Measured and simulated return loss of the RFID tag antenna before mounted on the shoes.

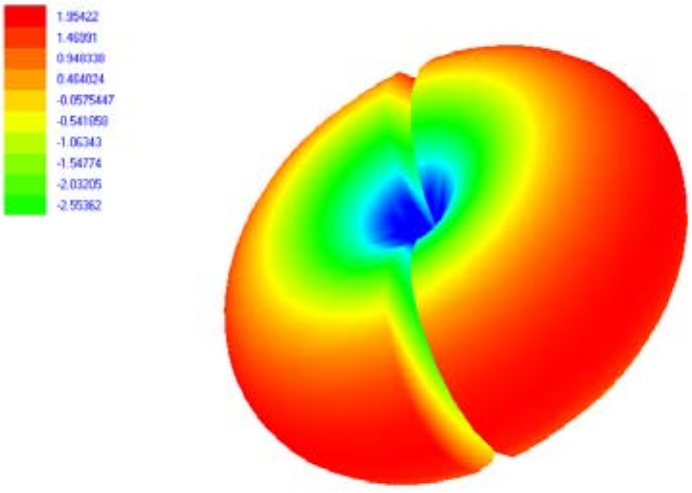

Figure 6.6: Far-field radiation pattern of the logo antenna.

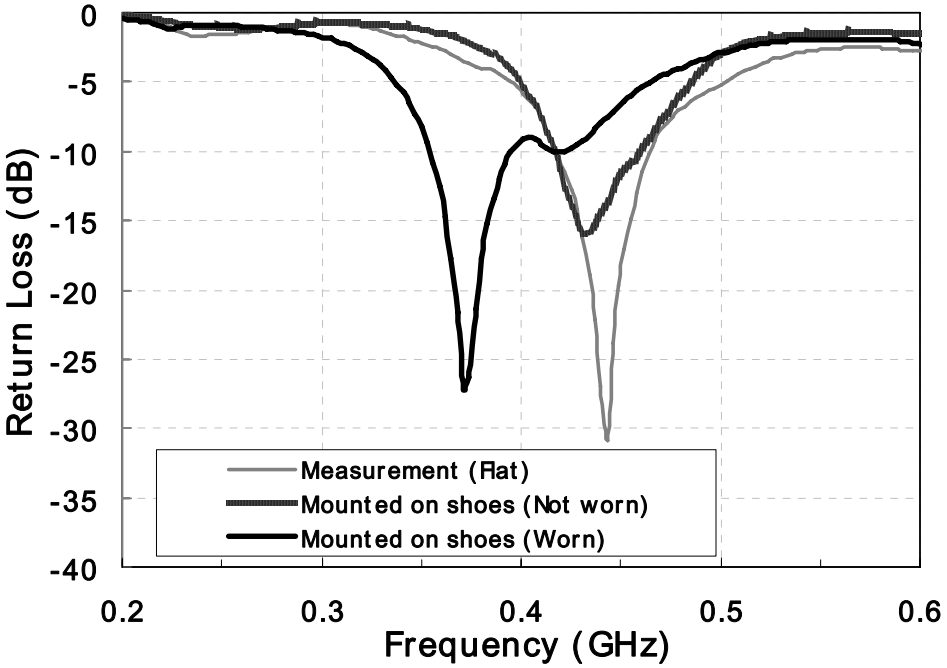

Figure 6.7: Measured return loss comparison of the RFID tag antenna mounted on the shoes with and without the human body effect.

The antenna structure intrinsically functions as a dipole. The current density distribution is depicted in Figure 6.4(b). A Rohde & Schwarz ZVA8 VNA was used to measure the antenna performance. The measured and simulated return loss of the RFID tag antenna before mounting on the shoes is shown in Figure 6.5. The measured BW of VSWR=2 extends from 419 MHz to 467 MHz, which is around 10.8% BW. The radiation pattern is plotted in Figure 6.6, which is almost omnidirectional at 433 MHz with gain around 1.95 dBi and 95.5% radiation efficiency.

After the tag antenna was mounted on the shoe, the maximum return loss was detuned from -31 dB up to -15.8 dB, because of the existence of the shoe and the bending of the logo to fit the shoe surface. But almost no frequency shift was observed, the BW still covers 433MHz, extending from 422 MHz to 464 MHz. When the shoe was worn, the human body influence on the antenna matching can be observed from the shifting of the resonant frequency, as shown in Figure 6.7. The central frequency is shifted down to

377 MHz. To be noticed, VSWR=2 is able to be maintained at 433 MHz. An acceptable matching is still achieved. This verifies the robust performance of the proposed wearable antenna design.

To measure the gain of the antenna after mounting on the shoe, the equipment was set up, as shown in Figure 6.8. The prototype antenna to be measured was treated as the transmitter and was connected with a coaxial cable to a signal generator. The tag antenna was attached at a height of h_t=1.22 m. Polystyrene foam was used to hold the shoe in place, simulating a free-space environment. The receiver antenna was connected with a coaxial cable to the Tektronix RSA3408A Real-time Spectrum Analyzer (RTSA) and was positioned at a fixed place that had also a height of h_r=1.22 m. Both distances were measured from the middle point of each antenna to the ground. The distance between the transmitter and the receiver was measured d=4.06 m.

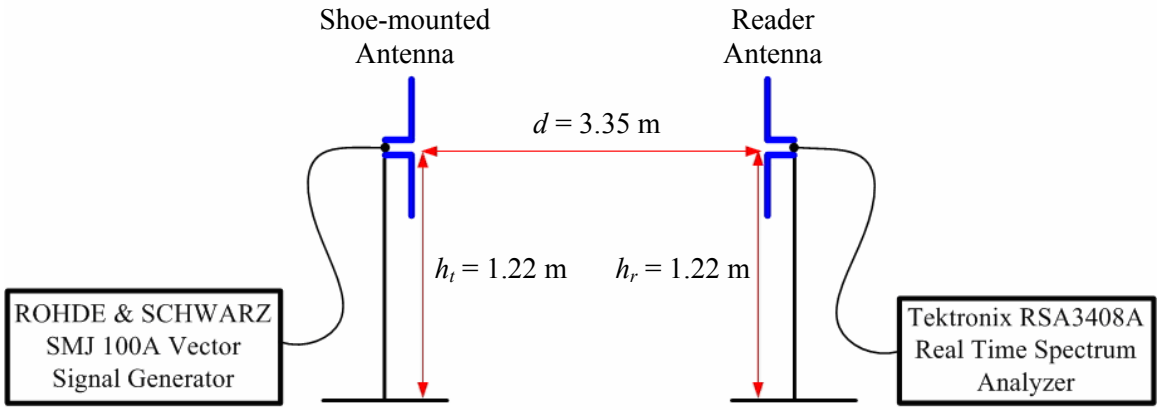

Figure 6.8: Gain measurement experimental setup.

$$r = \sqrt{\frac{\lambda}{\left(\frac{1}{d_t} + \frac{1}{d_r}\right)}} \tag{6.1}$$

For the measurement setup used, the maximum radius of the first Fresnel zone obtained at a midpoint between the transmitter and receiver was determined using Equation 6.1 [96], where λ is the wavelength of the transmitted signal. The lengths d_t and d_r in Equation 6.1 represent the distance of the Fresnel zone cross section under consideration from the transmitter and receiver, respectively, as shown in Figure 6.9.

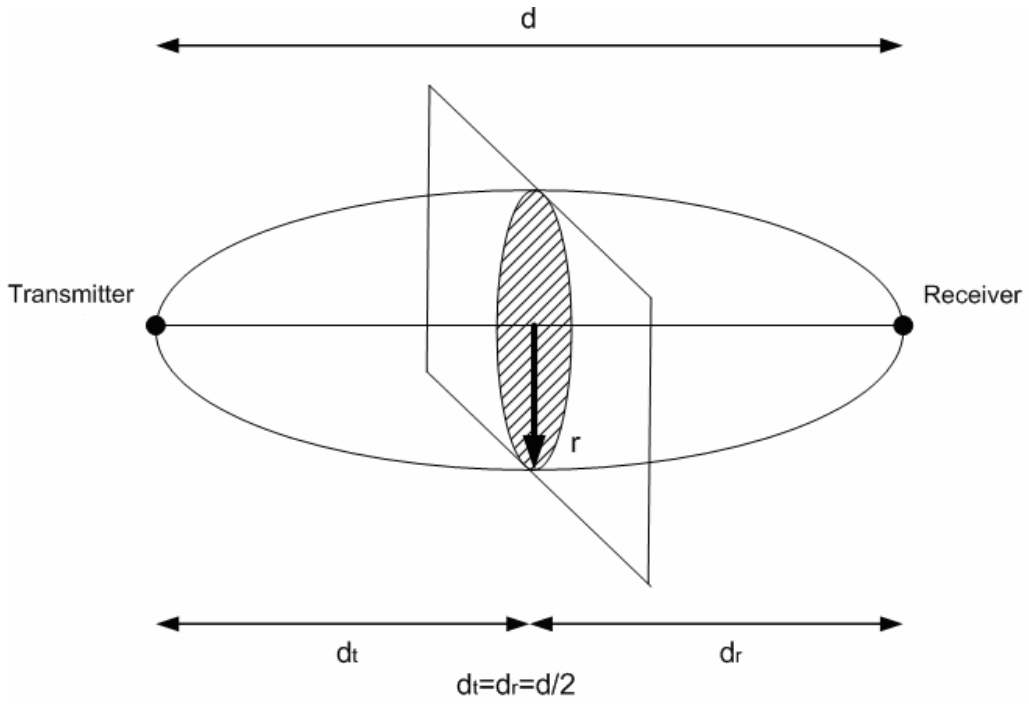

Figure 6.9: First Fresnel zone cross section at the middle point of the wireless link setup between the prototype antenna and the reader antenna.

The first Fresnel zone radius (r) was determined to be approximately 0.76 m, which is lower than the heights of the transmitter and receiver antenna. Based on this assessment, the requirement of the clearance of the first Fresnel zone was satisfied and, due to which, the free-space loss model was the most suited for determining the wireless link budget for the module [97]. The gain of the RFID logo antenna after mounting on the shoe was characterized to be 0.85 dBi. The decrease in the gain value is mainly due to the bending of the antenna structure on the conformal shoe surface.

6.4 Circuit Implementation

LINX TXE-433-KH2 Transmitter is ideally suited for the function of an active RFID tag. Housed in a compact SMD package, it combines a highly optimized RF transmitter with an on-board encoder. When the encoder is enabled, it first generates a pilot and synchronization period, and then broadcast a 10-bit ID and 8-bit data which is prefixed. The data sequence encoded by the on-board encoder that was be sent out by the RF wireless transmitter is shown in Figure 6.10. The required time for successful completion of transmission is around 50ms. The RF output power can be adjusted between -4 to 4 dBm by an external resister.

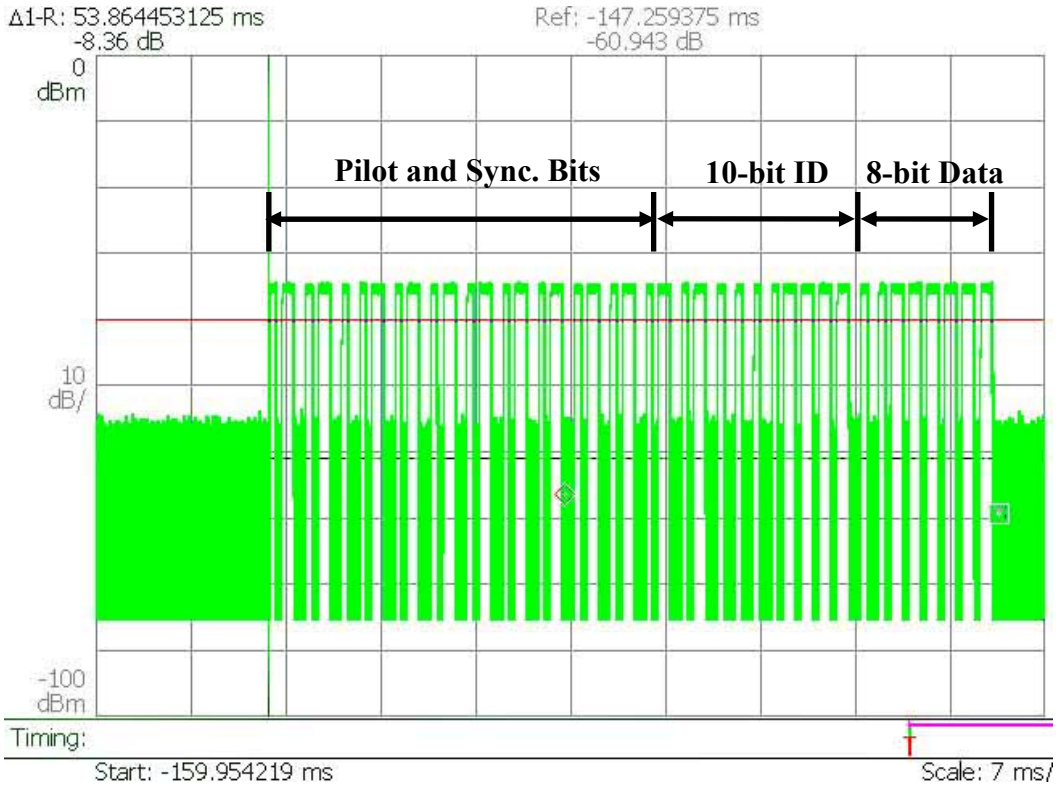

Figure 6.10: Diagram of the data sequence sent out by the active RFID tag.

Figure 6.11: Self-powered RFID shoes with mounted electronics.

Figure 6.11 shows the self-powered RFID shoes. Schematic diagram of the active RFID tag with piezoelectric energy harvesting circuit is shown in Figure 6.12. Photograph of the assembled key components of the system are shown in Figure 6.13, which includes the full-wave rectifying diode bridge, 4.7 *u*F storage capacitor, MAX666 linear voltage regulator, TXE-433-KH2 RF transmitter with on-board 20-bit encoder, and the logo antenna. During the assembly process, the antenna and the circuit trace were inkjet-printed one time together on the flexible organic substrate. Epo-Tek silver epoxy was then applied to fix the discrete components on the substrate, as shown in Figure 6.14. The epoxy had to be cured to harden its textures and improve conductivity.

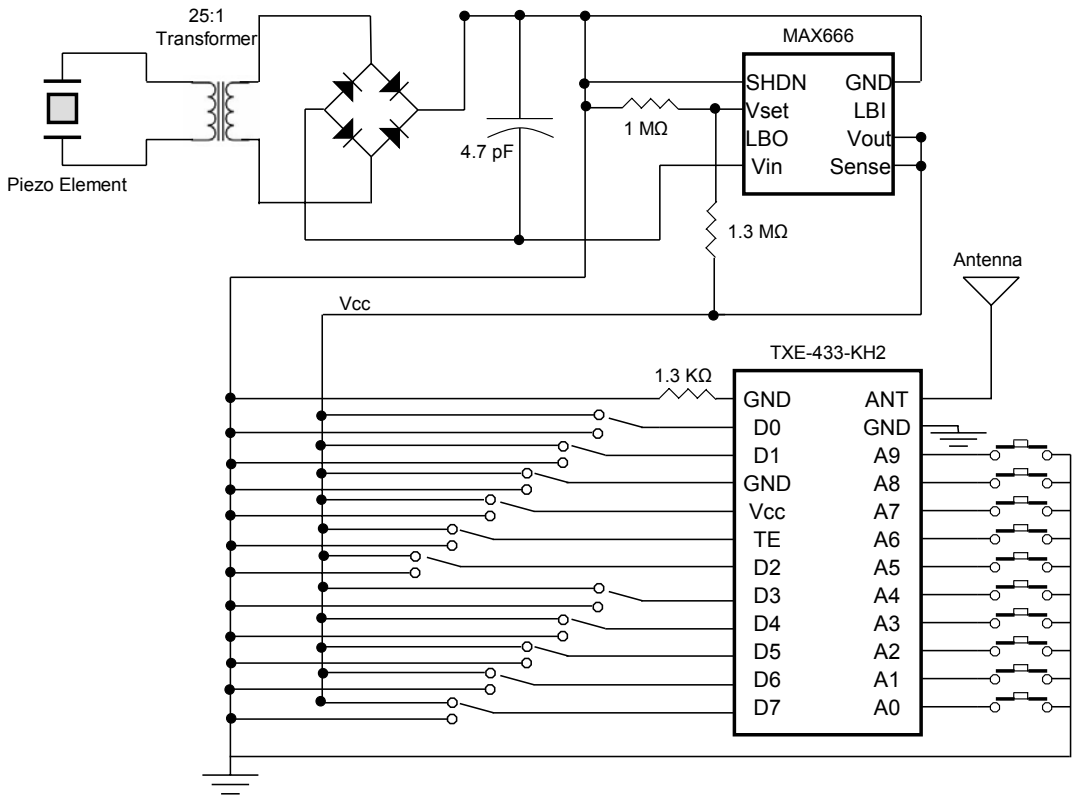

Figure 6.12: Schematic diagram of the self-powered active RFID tag.

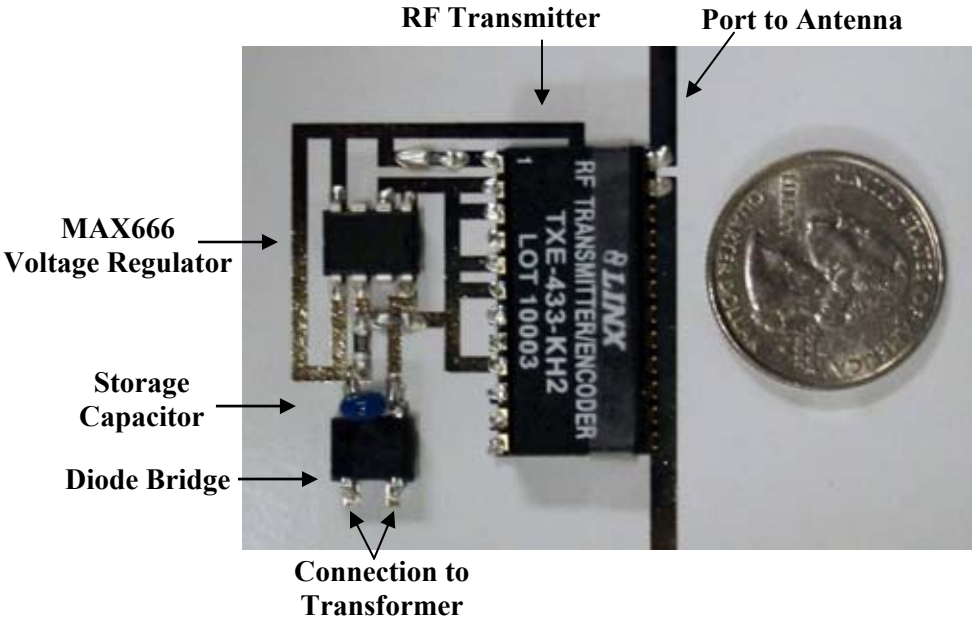

(a)

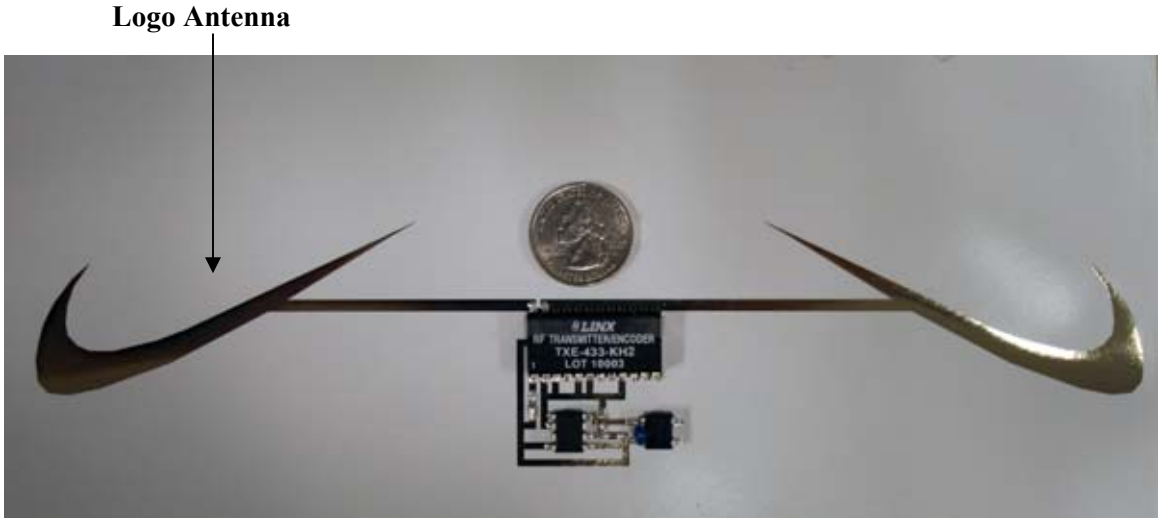

(b)

Figure 6.13: Photograph of the assembled prototype showing the key components packaged on an organic flexible substrate: (a) power regulator circuit and RF transmitter; (b) integration with the logo antenna.

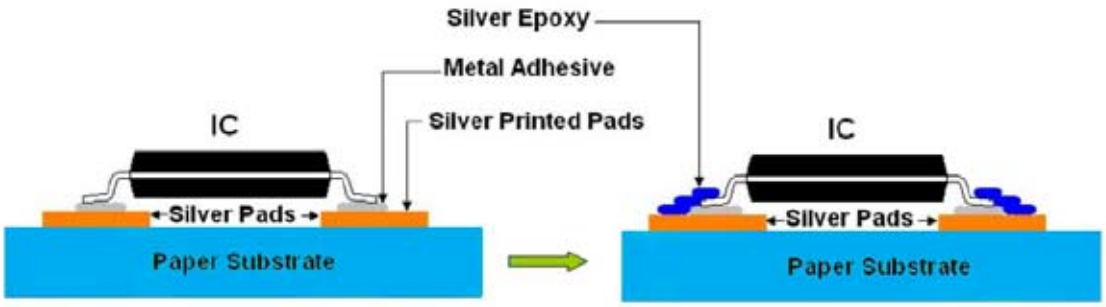

Figure 6.14: Assembly process for components on printed pads using the Epo-Tek silver epoxy.

The piezoelectric pushbutton and the step-down transformer were embedded in the bottom of the shoe. During walking, each step will trigger the pushbutton to be depressed. The energy harvesting phenomenon occurs when the spring-loaded hammer is released and delivers a dynamic mechanical force to the piezoelectric element. A pressure wave is reflected multiple times between the piezoelectric element and the hammer, in accord with the elastic and acoustical properties of the ceramic and the hammer [95]. The resonance in the piezoelectric element generates several AC voltage pulses. The transformer will step down the created high-voltage low-current wave into a low-voltage high-current wave for a better matching with the latter circuits. Since the output voltage is time dependent and takes the form of AC, the wave is fed into a full-wave diode bridge rectifier where the AC voltage is converted into DC voltage and then the energy is stored in the tank capacitor. The 4.7 *u*F capacitor integrates the charge transferred form the button strike. This, in-turn, powers a MAX666 low-dropout linear regulator, which provides a stable 3 V supply until the tank capacitor's charge is drained. The waveforms of the capacitor and the output of the linear regulator are shown in Figure 6.15, where Channel 1 is the capacitor voltage and Channel 2 is the linear regulator voltage.

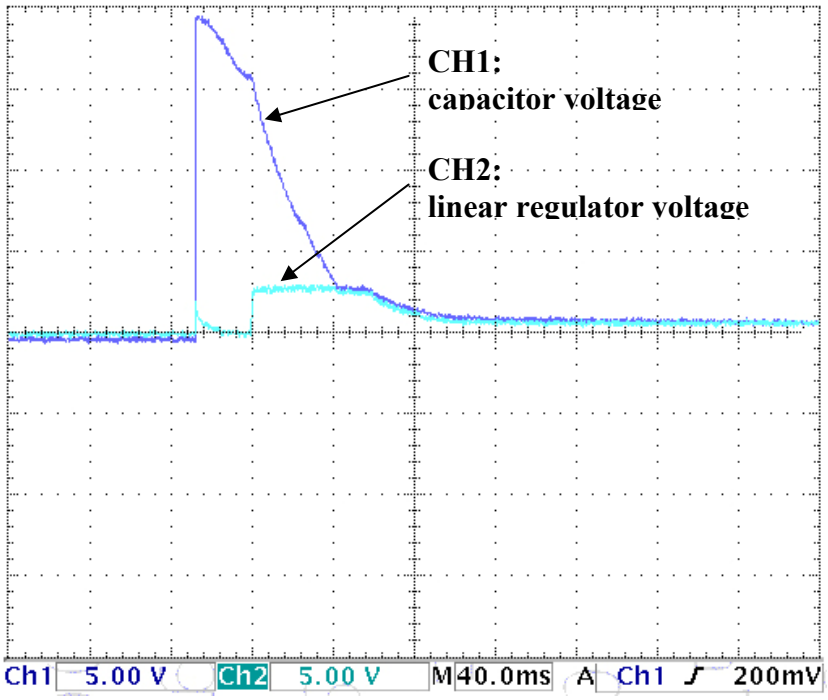

Figure 6.15: Voltage waveforms of capacitor and output of linear regulator.

The maximum voltage drop across the capacitor is 19V. The energy stored in the capacitor is measured by Equation 6.2:

$$E = \frac{1}{2} C V^2 \tag{6.2}$$

The amount of electrical energy harvested from each walking step is 848.4 uJ. As seen in Figure 6.15, at roughly 28 ms after the strike, the regulator becomes active, providing power to the active RFID circuitry. The 3V output will remain constant before it starts to drop to zero in respect with the capacitor discharge rate. When the voltage across the capacitor drops lower than 2.7 V, the active RFID tag will stop transmitting. The energy remained in the capacitor that could not be used to drive the tag is 17.1 uJ. Therefore, without considering the efficiency, there is 831.3 uJ energy can be used to power up the tag.

The maximum range of the transmitter is a function of the geographical setup with respect to the receiver, and also more importantly, to the receiver sensitivity. For active RFID, the communication range is larger than the passive ones. This would increase the maximum Fresnel zone radius in consideration of the relative low placement heights of the transmitter and receiver, especially the shoe-mounted antenna is only 7 cm above the ground. Due to this, the two-ray beam tracing model was used to compute longer range distances of the transmitter since it better accounted for received signals that had bounced off the ground [96]. For long distances with respect to the placement heights of the transmitter (h_t) and receiver (h_r), the range of the transmitter (d) was determined using Equation 6.3 as follows:

$$d = \left(\frac{Pt \cdot Gt \cdot G_r (h_t h_r)^2}{P_r}\right)^{\frac{1}{4}} \tag{6.3}$$

In Equation 6.3, P_r is the lowest power level detectable by a receiver, which is also known as the sensitivity of the receiver. A search for commercial transceivers that received ASK modulated signals, which are used for RFID, revealed sensitivities ranging from -65 to -110 dBm [98][99]. The power transmitted (P_t) and the gain of the transmit antenna (G_t) were determined to be -4 dBm and 0.85 dBi, respectively. Based on the receiver sensitivities found, for a 6 dBi gain receiver antenna (G_r), the shoe-mounted module would be expected to have a minimum range between 13.1 m to 175.3 m.

The required time for successful completion of the RFID ID broadcasting is 50 ms. The energy drain of the transmitter dominates over the remainder of the circuit. When the RF output power is set at -4 dBm level, the total circuit energy consumption is approximately 9 mW for 50 ms, totaling 450 uJ. As outlined above, the power scavenging circuit produces ample power for this application. This is verified in Figure 6.16, which is the transmitted signal captured by the RTSA. As shown in the figure, the

regulated DC voltage from the linear regulator is sufficient enough to power up the tag for over 60 ms, covering at least one complete broadcasting cycle which is 50 ms.

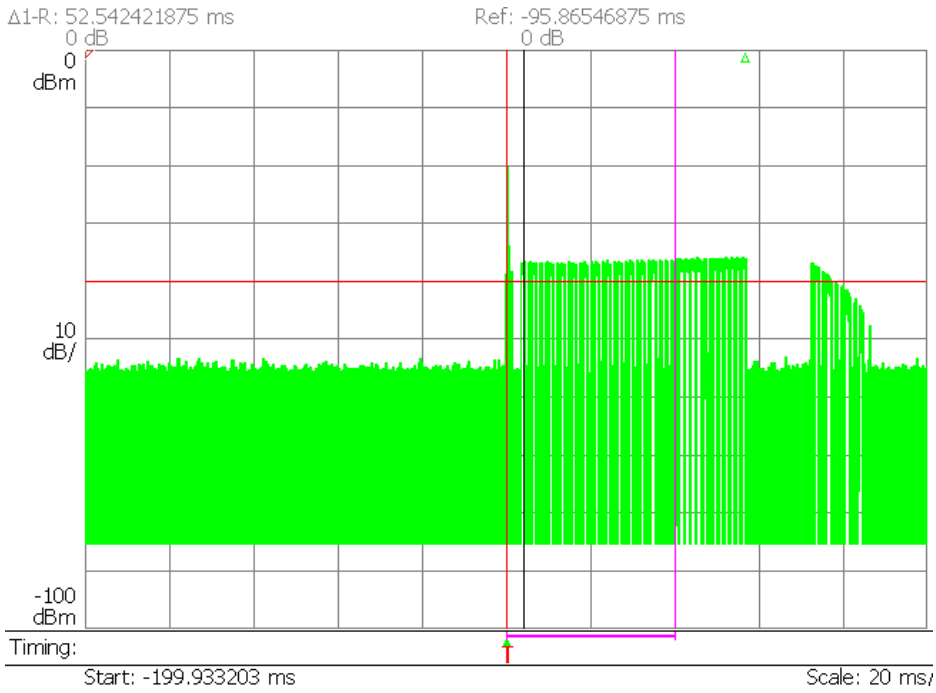

Figure 6.16: RFID data transmission captured by the RTSA reader antenna.

6.5 Chapter Summary

This chapter discusses various energy sources available in the environment that can be harvested. Although many different techniques are available to harvest energy to power wearable electronics, the amount of available raw energy and the surface area or net mass that the wearable device permits limit the power yield. In the research, a shoe-embedded piezoelectric generator was proposed, because it was an easy and effective way to harvest mechanical force energy from human beings as compared to other energy sources. An energy harvesting circuit designed for piezoelectric pushbutton is proposed and implemented efficiently for a self-powered active RFID tag. This RFID tag is capable

of transmitting an 18-bit digital word information using the mechanical force energy harvested from the heel striking. This technique can find direct applications in human positioning / tracking projects, and serve as a promising solution for other self-powered wearable electronics.

CHAPTER 7

CONTRIBUTIONS AND PUBLICATION TO DATE

This work has explored systematically design and development of a series of RFID tag structures that exhibit good performance characteristics on flexible substrates for conformal applications. There have been many contributions both to the academic and industry communities, mostly in helping better understand advantages and challenges brought by this technology. Perhaps the most substantial of these contributions are the following:

- The first paper material characterization on and above UHF band
  - Acknowledged by *IEEE International Microwave Symposium 2007* "Best Student Paper 3rd Place Award"
- The first inkjet-printed RFID tag on paper-based substrate
  - Acknowledged by *International Symposium on Antennas and Propagation 2007* "Best Poster 2nd Place Award"
- The first flexible RFID antenna on magnetic composite material
  - Acknowledged by *IEEE International Microwave Symposium 2008* "Best Student Paper Honorary Mention Award"
- Systematic investigation of passive RFID tag matching techniques
  - Acknowledged by *Asia-pacific Microwave Conference 2006* "Best Conference Paper Award"
- Several high-performance passive RFID tags on flexible substrates
- The first RFID-enabled gas sensor utilizing inkjet-printed carbon nanotubes
- The first wearable battery-free active RFID tag with piezoelectric energy scavenger on flexible substrate

This work and other related research in my PhD has led to the following publications:

Book

- L. Yang, A. Rida, and M. M. Tentzeris, "RFID and RFID-enabled Sensors on Flexible Low Cost Substrates," Morgan & Claypool Publishers, 2009. ISBN: 978-1-598-29860-4, Springer, 2008.

Book Chapters

- L. Yang, A. Rida, S. Basat, and M. M. Tentzeris, "RFID: Beyond the Basics" and "RFID: Issues of Security and Privacy ", chapters in *RFID Applied*, edited by J. Banks, D. Hanny, M. Pachano, L. Thompson, ISBN: 978-0-471-79365-6, John Wiley and Sons, 2007.
- L. Yang, A. Rida, A. Traille, and M. M. Tentzeris, "RFID", chapter in *Time Domain Methods in Electrodynamics*, edited by P. Russer, U. Siart, ISBN: 978-3-540-68766-5, Springer, 2008.

Journal Publications

- L. Yang, R. Zhang, D. Staiculescu, C. P. Wong, and M. M. Tentzeris, "A Novel Conformal RFID-enabled Module Utilizing Inkjet-printed Antennas and Carbon Nanotubes for Gas-detection Applications," *IEEE Antennas and Wireless Propagation*, vol. 8, pp. 653-656, 2009.
- L. Yang**,** L. J. Martin, D. Staiculescu, C. P. Wong, and M. M. Tentzeris, "Conformal Magnetic Composite RFID for Wearable RF and Bio-Monitoring Applications," *IEEE Transactions on Microwave Theory and Techniques*, vol. 56, no. 2, pp. 3223-3230, Dec. 2008.

- L. Yang, A. Rida, R. Vyas, M. M. Tentzeris, "RFID Tag and RF Structures on a Paper Substrate using Inkjet-Printing Technology," *IEEE Transactions on Microwave Theory and Techniques*, vol. 56, no. 2, pp. 2894-2901, Dec. 2007.
- L. Yang, A. Rida, R. Vyas, M. M. Tentzeris, "Novel 'Enhanced-Cognition' RFID Architectures on Organic/Paper Low-cost Substrates utilizing Inkjet Techonlogies," *International Journal of Antennas and Propagation*, vol. 2007, Article ID 68385, 2007.
- A. Rida, L. Yang, R. Vyas, D. Staiculescu and M. M. Tentzeris, "Novel Miniaturized Inkjet-printed Paper-Based UHF Components for RFID and Sensing Applications," *Journal of the European Microwave Association*, vol. 3, pp. 336-340, Dec. 2007.
- L. Martin, L. Yang, D. Staiculescu, H. Li, S. L. Ooi, C. P. Wong, and M. M. Tentzeris, "Investigation of the Impact of Magnetic Permeability and Loss of Magnetic Composite Materials on RFID Miniaturization for Conformal Medical Applications," accepted by *International Journal of Numerical Modelling: Electronic Networks, Devices and Fields*, Wiley, 2009.
- A. Rida, L. Yang, R. Vyas, and M. M. Tentzeris, "Conductive-Inkjet Printed Antennas on Flexible Low-Cost Paper-based Substrates for RFID and WSN Applications," accepted by *IEEE Antennas and Propagation Magazine*, 2009.
- A. Rida, L. Yang, S. Basat, A. Ferrer-Vidal, and M. M. Tentzeris, "Design, Development and Integration of Novel Antennas for Miniaturized UHF RFID Tags," accepted by *IEEE Transactions on Antennas and Propagation*, 2009.
- G. Orecchini, L. Yang, A. Rida, F. Alimenti, M. M. Tentzeris, and L. Roselli, "Green Technologies and RFID: Present and Future," accepted by *Applied Computational Electromagnetics Society Journal*, 2009.

Conference Publications

- L. Yang, D. Staiculescu, R. Zhang, C. P. Wong, and M. M. Tentzeris, "A Novel 'Green' Fully-integrated Ultrasensitive RFID-enabled Gas Sensor Utilizing Inkjet-printed Antennas and Carbon Nanotubes," *IEEE Antennas and Propagation Symposium*, pp. 1-4, June, 2009.
- L. Yang, L. Martin, D. Staiculescu, C. P. Wong, and M. M. Tentzeris, "A Novel Flexible Magnetic Composite Material for RFID, Wearable RF and Bio-monitoring Applications," *IEEE MTT-S International Microwave Symposium 2008*, pp. 963-966, June 2008. Best Student Paper Honorary Mention Award.
- L. Yang, R. Vyas, A. Rida, J. Pan, and M. M. Tentzeris, "Wearable RFID-enabled Sensor Nodes for Biomedical Applications," *Electronic Components and Technology Conference 2008*, pp. 2156-2159, May 2008.
- L. Yang, L. Martin, D. Staiculescu, C. P. Wong, and M. M. Tentzeris, "Design and Development of Compact Conformal RFID Antennas Utilizing Novel Flexible Magnetic Composite Materials for Wearable RF and Biomedical Applications," *IEEE Antenna and Propagation Society International Symposium 2008*, pp. 1-4, July 2008. Best Student Paper Honorary Mention Award.
- A. Rida, L. Yang, N. Chaisilwattana, S. Travis, S. Bhattacharya, and M. M. Tentzeris, "3D Packaging Architecture using Paper as a Dielectric Medium," *Electronic Components and Technology Conference 2008*, pp. 371-373, May 2008.
- M. M. Tentzeris, L. Yang, A. Rida, A. Traille, R. Vyas, and T. Wu, "Inkjet-printed Antennas on Paper: Are They the Ultimate Solution for UHF Ubiquitous Cognitive-intelligence RFID-enabled Applications," *2007*

International Symposium on Antennas and Propagation, Niigata, Japan, Aug. 2007. Best Poster 2nd Place Award.

- L. Yang, A. Rida, J. Li, and M. M. Tentzeris, "Antenna Advancement Techniques and Integration of RFID Electronics on Organic Substrates for UHF RFID Applications in Automotive Sensing and Vehicle Security," Proc. of *2007 IEEE 66th Vehicular Technology Conference*, Baltimore, MD, Oct. 2007.
- A. Rida, L. Yang, R. Vyas, S. Bhattacharya, and M. M. Tentzeris, "Design and Integration of Inkjet-printed Paper-Based UHF Components for RFID and Ubiquitous Sensing Applications," Proc. of *2007 European Microwave Conference*, Munich, Germany, Oct. 2007.
- L. Yang, M. M. Tentzeris, "3D Multilayer Integration and Packaging on Organic/Paper Low-cost Substrates for RF and Wireless Applications," Proc. of *2007 IEEE International Symposium on Signals, Systems and Electronics*, pp.267-270, Montreal, Canada, Aug. 2007.
- L. Yang, A. Rida, R. Vyas, and M. M. Tentzeris, "Wearable Inkjet-printed RFID on Fiber-based Materials for Real-time Diagnostics and Medical Monitoring Applications", 2007 *URSI North American Radio Science Meeting*, Ottawa, Canada, July 2007.
- L. Yang, M. M. Tentzeris, "Design and Characterization of Novel Paper-based Inkjet-Printed RFID and Microwave Structures for Telecommunication and Sensing Applications," Proc. of *2007 IEEE International Microwave Symposium*, pp.1633-1636, Honolulu, HI, Jun. 2007. Best Student Paper 3rd Place Award.
- L. Yang, A. Rida, T. Wu, S. Basat, and Manos M. Tentzeris, "Integration of Sensors and Inkjet-Printed RFID Tags on Paper-based Substrates for 'UHF

Cognitive Intelligence' Applications," Proc. of *2007 IEEE Antennas and Propagation Symposium*, Honolulu, HI, Jun. 2007.

- A. Rida, L. Yang, and M. M. Tentzeris, "Design and Characterization of Novel Paper-based Inkjet-Printed UHF Antennas for RFID and Sensing Applications," Proc. of *2007 IEEE Antennas and Propagation Symposium*, Honolulu, HI, Jun. 2007. Best Student Paper 1st Place Award.
- T. Wu, A. Traille, L Yang, B. Pan, J. Papapolymerou and M. M. Tentzeris, "Novel Substrate-independent Broadband Micromachined Antennas for mm-wave Cognitive Radio Applications," Proc. of *2007 IEEE Antennas and Propagation Symposium*, Honolulu, HI, Jun. 2007.
- A. Rida, L. Yang, R. Vyas, S. Basat, S. Bhattacharya, and M. M. Tentzeris, "Novel Manufacturing Processes for Ultra-Low-Cost Paper-Based RFID Tags With Enhanced 'Wireless Intelligence' ," Proc. of *2007 IEEE Electronic Components and Technology Conference*, pp.773-776, Reno, NV, Jun. 2007.
- R. Vyas, A. Rida, L. Yang, and M. M. Tentzeris, “Design, Integration and Characterization of a Novel Paper-based Wireless Sensor Module,” *IEEE International Microwave Symposium 2008*, pp. 1305-1308, June 2008.
- S. Bhattacharya, M. M. Tentzeris, L. Yang, S. Basat, A. Rida, "Flexible LCP and Paper-based Substrates with Embedded Actives, Passives, and RFIDs," *IEEE Polytronic 2007, 6th International IEEE Conference on Polymers and Adhesives in Microelectronics and Photonics*, pp.159 - 166, Tokyo, Japan, Jan. 2007.
- L. Yang, S. Basat, A. Rida, and M. M. Tentzeris, "Design and Development of Novel Miniaturized UHF RFID Tags on Ultra-low-cost Paper-based Substrates," Proc. of *2006 Asian-Pacific Microwave Conference*, pp.1493-1496, Yokohama, Japan, Dec. 2006. Best Conference Paper Award.

- L. Yang, S. Basat, and M. M. Tentzeris, "Design and Development of Novel Inductively Couple RFID Antennas," Proc. of *2006 IEEE Antennas and Propagation Symposium*, pp.1035-1038, Albuquerque, NM, July 2006.
- S. Basat, S. Bhattacharya, L. Yang, A. Rida, M. M. Tentzeris and J. Laskar, "Design of a Novel High-efficiency UHF RFID Antenna on Flexible LCP Substrate with High Read-Range Capability," Proc. of *2006 IEEE Antennas and Propagation Symposium*, pp.1031-1034, Albuquerque, NM, July 2006.
- S. Basat, S. Bhattacharya, A. Rida, S. Johnston, L. Yang, M. M. Tentzeris, J. Laskar, "Fabrication and Assembly of a Novel High-Efficiency UHF RFID Tag on Flexible LCP Substrate," Proc. of *2007 IEEE Electronic Components and Technology Conference*, pp.1352-1355, San Diego, CA, May 2006.

REFERENCES

[1] J. Landt, “The History of RFID,” *IEEE Potentials*, 24, 4, Oct.-Nov. 2005, pp. 8-11.

[2] A. R. Koelle, S. W. Depp, and R. W. Freyman, “Short-Range Raido-Telemetry for Electronic Identification, Using Modulated RF Backscatter,” *Proceedings of the IEEE*, 63, 8, Aug. 1975, pp. 1260-1261.

[3] A. R. Koelee, “Short Range UHF Telemetry System Using Passive Transponders for Vehicle ID and Status Information,” *IEEE Workshop on Automotive Applications of Electronics*, Oct. 1988, pp. 34-38.

[4] R. Want, “An Introduction to RFID Technology*,” IEEE Pervasive Computing*, 5, 1, Jan.-Mar. 2006, pp. 25-33.

[5] Gartner Inc. “Worldwide RFID revenue to surpass $1.2 billion in 2008,” http://www.mb.com.ph/issues/2008/03/05/TECH20080305118642.html

[6] K. Finkenzeller, RFID Handbook: Fundamentals and Applications in Contactless Smart Cards and Identification*, John Wiley and Sons Inc, New York*, 2nd edition, 2003.

[7] RFID Journal, “The History of RFID Technology,” http://www.rfidjournal.com/article/articleview/1338/1/129

[8] Harry Stockman, “Communication by Means of Reflected Power,” *Proceedings of the IRE*, pp. 1196-1204, Oct. 1948.

[9] Jeremy Landt, “Shrouds of Time The History of RFID,” *AIM Inc*., ver. 1.0. Oct. 2001.

[10] Howard Baldwin, “How to Handle RFID’s Real-world Challenges,” http://www.microsoft.com/midsizebusiness/businessvalue/rfidchallenges.mspx, *Microsoft Corporation*, 2006.

[11] V. Subramanian, J. Frechet, "Progress toward development of all-printed RFID tags: materials, processes, and devices," *Proceedings of the IEEE*, vol. 93, no. 7, pp. 1330-1338, July 2005.

[12] Mark Roberti, “Tag Cost and ROI,” www.rfidjournal.com/article/articleview/796/

[13] Gitanjali Swamy, and Sanjay Sarma, “Manufacturing Cost Simulations for Low Cost RFID Systems,” *Auto-ID Center*, Feb. 2003.

[14] Tracking RFID: What Savvy IT Managers Need to Know Today, www.sun.com/emrkt/innercircle/newsletter/0305cto.html

[15] Antonio Ferrer-Vidal, Amin Rida, Serkan Basat, Li Yang, and Manos M. Tentzeris, "Integration of Sensors and RFID’s on Ultra-low-cost Paper-based Substrates for Wireless Sensor Networks Applications", *Wireless Mesh Networks, 2006. WiMesh 2006. 2nd IEEE Workshop on*, pp.126-128, Reston, VA, 2006.

[16] S. Simula, S. Ikalainen, and K. Niskanen, "Measurement of the Dielectric Properties of Paper," *Journal of Imaging Science and Tech*. Vol. 43, No. 5, September 1999.

[17] H. Ichimura, A. Kakimoto, and B. Ichijo, "Dielectric Property Measurement of Insulating Paper by the Gap Variation Method," *IEEE Trans. Parts, Materials and Packaging*, Vol. PMP-4, No. 2, June, 1968.

[18] L. Apekis, C. Christodoulides, and P. Pissis, "Dielectric properties of paper as a function of moisture content," *Dielectric Materials, Measurements and Applications, 1988., Fifth International Conference*, pp. 97-100, 27-30 Jun 1988.
[19] P. V. Nikitin, K. V. S. Rao, "Performance Limitations of Passive UHF RFID Systems," *IEEE Antennas and Propagation Society Symp*., pp. 1011-1014, July 2006.
[20] K. V. S. Rao, Pavel V. Nikitin, S. F. Lam, "Impedance Matching Concepts in RFID Transponder Design," *Fourth IEEE Workshop on Automatic Identification Advanced Technologies*, AutoID'05, pp.39-42, 2005.
[21] David M. Pozar, Microwave Engineering, 3rd Edition, *John Wiley and Sons Inc*., 2005.
[22] K. Kurokawa, "Power Waves and the Scattering Matrix," *Microwave Theory and Techniques, IEEE Transactions on.,* vol. MTT-13, no. 3, pp. 194-202, Mar. 1965.
[23] P. V. Nikitin, K. V. S. Rao, S. F. Lam, V. Pillai, R. Martinez, and H. Heinrich, "Power Reflection Coefficient Analysis for Complex Impedances in RFID Tag Design," *IEEE Transactions on Microwave Theory and Techniques*, vol. 53, issue 9, pp. 2721-2725, 2005.
[24] S.Basat, S.Bhattacharya, L.Yang, A.Rida, M.M.Tentzeris and J.Laskar, "Design of a Novel High-efficiency UHF RFID Antenna on Flexible LCP Substrate with High Read-Range Capability", *Procs. of the 2006 IEEE-APS Symposium*, pp.1031-1034, Albuquerque, NM, July 2006.
[25] S. Roundy, "Energy Scavenging for Wireless Sensor Networks," *Kluwer Academic Publishers*, 2003.
[26] E. Braunwald, Heart Disease: A Textbook of Cardiovascular Machine, *Philadelphia, W. B. Saunders Company*, 1980.
[27] T. Starner, "Human Powered Wearable Computing," *IBM System J*., vol. 35, no. 3 and 4, pp. 618-629, 1996.
[28] V. Leonov, T. Torfs, P. Fiorini, and C. V. Hoof, "Thermoelectric Converters of Human Warmth for Self-powered Wireless Sensor Nodes," *IEEE Sensor Journal*, vol. 7, no. 5, 2007.
[29] P. D. Mitcheson, "Architectures for Vibration-Driven Micropower Generators," *J. Microelectromechanical Systems*, vol. 13, no. 3, pp. 429-440, 2004.
[30] B. Gilomen and P. Schmidli, "Mouvement a quartz dame don't I'energie est fournie par une generatrice," *Congres Europeen de Chronometrie*, Geneva, Sep. 2000.
[31] R. Want, "An introduction to RFID technology," *IEEE Pervasive Computing*, 5, 1, pp. 25-33, Jan. –Mar. 2006.
[32] G. Marrocco, "The art of UHF RFID antenna design: impedance-matching and size-reduction techniques," *IEEE Antennas and Propagation Magazine*, vol. 50, no.1, pp. 66-79, 2008.
[33] C. Balanis, "Antenna theory, analysis and design," third edition, *John Wiley & Sons, Inc., Publication*.
[34] G. Marrocco, "RFID antennas for the UHF remote monitoring of human subjects," *IEEE Transactions on Antennas and Propagation*, pp 1862-1870, Jun., 2007.

[35] C. Cho and I. Park, “Design of UHF small passive tag antennas,” *IEEE Antennas and Propagation Society International Symposium*, vol. 2, pp. 349 – 352, July 2005.
[36] H.-W Son and C.-S Pyo, “Design of RFID tag antennas using an inductively coupled feed,” *Electronics Letters*, vol. 41, pp. 994 – 996, No. 18, Sept. 2005.
[37] K. Rao, P. Nikitin, S. Lam, “Antenna design for UHF RFID tags: a review and a practical application,” *IEEE Transactions on Antennas and Propagation*, vol. 53, no. 12, Dec. 2005.
[38] J. Dacuna, R. Pous, “Low-profile patch antenna for RF identification applications,” *IEEE Transcations on Microwave Theory and Techniques*, vol. 57, No. 5, May. 2009.
[39] D. Dobkins, and S. Weigand, “Environmental effects on RFID tag antennas,” in *IEEE MTT-S International Microwave Symposium*, Long Beach, CA, pp. 4-7, June 2005.
[40] S. Aroor, and D. Deavours, “Evaluation of the state of passive UHF RFID: An experimental approach,” *IEEE Systems Journal*, vol. 1, no.2, pp. 168-176, 2007.
[41] H. Kwon, and B. Lee, “Compact slotted planar inverted-F RFID tag mountable on metallic objects,” *Electronics Letters*, vol. 41, no. 24, pp. 1308-1310, Nov. 2005.
[42] T. Mishima, K. Tanaka, N. Abe, H. Taki, "Toward construction of a mobile system with long-range RFID sensors," *Proc. of the 2004 IEEE Conference on Cybernetics and Intelligent Systems*, Vol. 2, pp. 960-965, 2004.
[43] L. Yang, and M. M. Tentzeris, “Design and Characterization of Novel Paper-based Inkjet-Printed RFID and Microwave Structures for Telecommunication and Sensing Applications”, *IEEE Intentional Microwave Symposium*, June, 2007
[44] M. Berggren, T. Kugler, T. Remonen, D. Nilsson, M. Chen, P. Norberg, "Paper electronics and electronic paper," *Proc. of the 2001 IEEE Conference on Polymers and Adhesives in Microelectronics and Photonics*, pp. 300-303, October 2001.
[45] A. Piquire, D. Chrisey, “Direct-write Technologies for rapid prototyping applications: sensors, electronics, and integrated power sources,” *Acamedic Press*, 2002.
[46] Dimatix Inc. www.dimatix.com
[47] M. Carter, J. Colvin, and J. Sears, "Characterization of conductive inks deposited with maskless mesoscale material deposition," *TMS2006*, Mar. 12-16, San. Antonio, Texas, USA
[48] Cabot Corporation, “Inkjet silver conductor AG-IJ-G-100-S1,” Data Sheet, October 2006.
[49] V. Marinov, "Electrical resistance of laser sintered direct-write deposited materials for microelectronic applications," *Journal of Microelectronics and Electronic Packaging*, 1:4, pp. 261-268, 2004.
[50] R. B. Marks, "A multiline method of network analyzer calibration," *IEEE Trans. Microwave Theory Tech*., vol. 39, pp. 1205-1215, Dec. 1991.
[51] G. Zou, H. Gronqvist, P. Starski, and J. Liu, "High frequency characteristics of liquid crystal polymer for system in a package application," *IEEE 8th Int. Advanced Packaging Materials Symp*., Mar. 2002, pp.337–341.

[52] G. Zou, H. Gronqvist, P. Starski, and J. Liu, "Characterization of liquid crystal polymer for high frequency system-in-a-package applications, *" IEEE Trans. Advanced Packaging*, vol. 25, pp. 503-508, No.4, Nov. 2002.
[53] M. H. Kutner, C. J. Nachtsheim, J. Neter, W. Li, "Applied Linear Statistical Models," 5th Edition, *the McGraw-Hill Education*.
[54] L. J. van der Pauw, "The radiation of electromagnetic power by microstrip configurations," *IEEE Trans. Microwave Theory Tech*., vol. 25, pp. 719–725, Sept. 1977.
[55] M. D. Abouzahra and L. Lewin, "Radiation from microstrip discontinuities," *IEEE Trans. Microwave Theory Tech*., vol. MTT-27, pp. 722–723, Aug. 1979.
[56] P. Guillon and Y. Garault, "Complex permittivity of MIC substrate," *AEU*, pp. 102–104, 1981.
[57] R. A. Pucel, D. J. Massé, and C. P. Hartwig, "Losses in microstrip," *IEEE Trans. Microwave Theory Tech*., vol. MTT-16, pp. 342–350, June 1968.
[58] B. C. Wadell, Transmission Line Design Handbook. *Norwood, MA: Artech House*, 1991, pp. 93–99.
[59] K. J. Coakley, J. D. Splett, M. D. Janezic, , "Estimation of Q-Factors and Resonant Frequencies," *IEEE Trans. Microwave Theory Tech*., vol. 51, No. 3, pp. 862-868, 2003.
[60] E. Vanzura, R. Geyer, and M. Janezic, "The NIST 60-Millimeter Diameter Cylindrical Cavity Resonator: Performance for Permittivity Measurements," *NIST Standard* TN-1354, 1993.
[61] D. C. Thompson, O. Tantot, H. Jallageas, G. E. Ponchak, M. M. Tentzeris, and J. Papapolymerou, " Characterization of liquid crystal polymer (LCP) material and transmission lines on LCP substrates from 30-110 GHz," IEEE Trans. Microwave Theory Tech., vol. 52, pp. 1343-1352, April 2004.
[62] C. Balanis, "Antenna theory, analysis and design," third edition, *John Wiley & Sons, Inc., Publication*.
[63] Texas Instrument, "UHF Gen2 Strap RI-UHF-STRAP-08," Data Sheet, October 2006.
[64] S.D. Kulkarni, R.M. Boisse, and S.N. Makarov, "A Linearly-Polarized Compact UHF PIFA with Foam Support," Department of Electrical Engineering, Worcester Polytechnic Institute.
[65] Intermec Inc. Product Datasheet, www.intermec.com.
[66] K. Finkenzeller, RFID Handbook, 2nd ed., Wiley, 2004.
[67] A. Cangialosi, J. E. Monaly, S. C. Yang, "Leveraging RFID in hospitals: Patient life cycle and mobility perspectives," *Communications Magazine, IEEE* Volume 45, Issue 9, September 2007 pp. 18 – 23
[68] G. Marrocco, "RFID Antennas for the UHF Remote Monitoring of Human Subjects," *Antennas and Propagation, IEEE Transactions on* Volume 55, Issue 6, Part 2, June 2007 Page(s):1862 - 1870

[69] "Magnetic Materials for RFID," TechnoForum 2005, TDK, http://www.tdk.co.jp/tf2005/pdf_e/2f0215e.pdf
[70] N. Das and A. K. Ray, "Magneto Optical Technique for Beam Steering by Ferrite Based Patch Arrays," *IEEE Transactions on Antennas and Propagation*, vol. 49, no. 8, August (2001); pp. 1239-1241.
[71] S. Morrison, C. Cahill, E. Carpenter, S. Calvin, R. Swaminathan, M. McHenry, V. Harris, "Magnetic and Structural Properties of Nickel Zinc Ferrite Nanoparticles Synthesized at Room Temperature," *Journal of Applied Physics*, vol. 95, no. 11, June (2004); pp. 6392-6395.
[72] H. Dong, F. Liu, Q. Song, Z.J. Zhang, C. P. Wong, "Magnetic Nanocomposite for High Q Embedded Inductor," *IEEE International Symposium and Exhibition on Advance Packaging Materials: Process, Properties, and Interfaces*, Atlanta, Georgia, March (2004); pp. 171-174.
[73] A. Rida, L. Yang, R. Vyas, S. Bhattacharya, M. M. Tentzeris, "Design and integration of inkjet-printed paper-based UHF components for RFID and ubiquitous sensing applications," . *European Microwave Conference*, 9-12 Oct. 2007 pp. 724 – 727.
[74] L.Yang, L. Martin, D. Staiculescu, C. P. Wong, M.M. Tentzeris, "A Novel Flexible Magnetic Composite RFID for Wearable RF and Bio-monitoring Applications", *2008 IEEE IMS Symposium*, Atlanta, GA, June 2008.
[75] P. V. Nikitin, S. Rao, S. F. Lam, V. Pillai, and H. Heinrich, "Power reflection coefficient analysis for complex impedances in RFID tag design," *IEEE Trans. Microw. Theory Tech*., vol. 53, no. 9, Sep. 2005, pp. 2721–2725.
[76] A. Hung, S. Wong, W. Ismail, "RFID Transponder Using Bow Tie Antenna for Wireless Application," *RF and Microwave Conference*, 2006. RFM 2006. International, 12-14 Sept. 2006, pp. 21 – 25.
[77] A. Galehdar, D. V. Thiel, S. G. O'Keefe, S. P. Kingsley, "Efficiency variations in electrically small, meander line RFID antennas," *Antennas and Propagation International Symposium, 2007 IEEE* 9-15 June 2007 pp. 2273 – 2276.
[78] S. O. Kasap, Principles of Electronic Materials and Devices, 2nd ed., *The McGraw-Hill Companies*, New York, 2002; p.516.
[79] L. L. Hench and J. K. West, Principles of Electronic Ceramics, *John Wiley & Sons*, New York, 1990; p.296.
[80] J. Neter et al, "Applied Linear Statistical Models", 4th Ed., *The McGraw-Hill Companies*, Chicago, 1996.
[81] D. Staiculescu, C. You, L. Martin, W. Hwang, M. M. Tentzeris, "Hybrid Electrical/Mechanical Optimization Technique Using Time-Domain Modeling, Finite Element Method and Statistical Tools for Composite Smart Structures", *Proc. of the 2006 IEEE IMS Symposium*, June 2006, pp. 288-291.
[82] M. Philipose, J. Smith, B. Jiang, A. Mamishev, K. Sundara-Rajan, "Battery-free wireless identification and sensing," *IEEE Pervasive Computing*, Volume 4, Issue 1, pp. 37 – 45, 2005.

[83] S. Johan, Z. Xuezhi, T. Unander, A. Koptyug, H. Nilsson, "Remote Moisture Sensing utilizing Ordinary RFID Tags," *IEEE Sensors 2007*, pp. 308 - 311, 2007
[84] S. Iijima, Nature, 1991, 354, 56.
[85] T. Zhang, S. Mubeen, N, Myung, and M. Deshusses, "Recent progress in carbon nanotube-based gas sensors," *Nanotechnology,* vol. 19, July, 2008
[86] D. R. Kauffman, and Alexander Star, "Carbon Nanotube Gas and Vapor Sensors," *Nanotechnology*, pp. 6550-6570, 2008.
[87] J. Song, J. Kim, Y. Yoon, B. Choi, and C. Han, "Inkjet printing of singe-walled carbon nanotubes and electrical characterization of the line pattern," *Nanotechnology*, vol. 19, 2008.
[88] M. Dragoman, E. Flahaut, D. Dragoman, M. Ahmad, R. Plana, "Writing electronic devices on paper with carbon nanotube ink," ArXiv-0901.0362, Jan. 2009.
[89] Carbon Solutions, Inc., http://www.carbonsolution.com/products/products.html
[90] P. V. Nikitin, K. V. S. Rao, "Performance limitations of passive UHF RFID systems," *IEEE Symposium on Antennas and Propagation 2006*, pp. 1011-1014, July 2006.
[91] J. Penders, B. Gyselinckx, R. Vullers, etc., "Human++: from technology to emerging health monitoring concepts," *5th International Summer School and Symposium on Medical Devices and Biosensors*, pp. 94-98, June, 2008.
[92] J. Paradiso, T. Starner, "Energy scavenging for mobile and wireless electronics," *IEEE Pervasive Computing*, vol. 4, pp. 18-27, 2005.
[93] N. Shenck, J. Paradiso, "Energy scavenging with shoe-mounted piezoelectrics," *IEEE Micro*, vol. 21, pp. 30-42, 2001.
[94] K. Y. Hoe, "An investigation of self powered RF wireless sensors," National University of Singapore, 2006.
[95] Y. Tan, K. Hoe, S. Panda, "Energy harvesting using piezoelectric igniter for self-powered radio frequency wireless sensors," *IEEE International Conference on Industrial Technology*, pp. 1711-1716, 2006.
[96] J. Seybold, Introduction to RF Propagation. Hoboken, NJ: Wiley, 2005, pp. 111–133, 163–179.
[97] T. Kvaksrud, "Range measurements in an open field environment," Texas Instrum. Incorporated, Dallas, TX, Design Note DN018, 2008.
[98] "UHF ASK/FSK transceiver: ATA5429," Atmel, San Jose, CA, Data sheet, Oct. 2007.
[99] "KH2 series receiver / decoder data guide," Linx Technologies, Data sheet, Jan. 2006.